OPTIMIZATION AND APPLICATION OF MEV TIME-OF-FLIGHT SECONDARY ION MASS SPECTROMETRY IN THE STANDARD AND LOW PRIMARY ION BEAM ENERGY MODE

Marko Barac

Doctoral Dissertation
Jožef Stefan International Postgraduate School
Ljubljana, Slovenia

Supervisor: Dr. Sc. Zdravko Siketić, Department of Experimental Physics, Ruđer Bošković Institute, Zagreb, Croatia
Co-Supervisor: Prof. Dr. Janez Kovač, Department of Surface Engineering, Jožef Stefan Institute, and Jožef Stefan International Postgraduate School, Ljubljana, Slovenia

Evaluation Board:
Prof. Dr. Primož Pelicon, Chair, Jožef Stefan International Postgraduate School and Jožef Stefan Institute, Ljubljana, Slovenia
Asst. Prof. Klemen Bučar, Member, Jožef Stefan International Postgraduate School and Jožef Stefan Institute, Ljubljana, Slovenia
Dr. Max Doebeli, Member, ETH Zurich, Switzerland

MEDNARODNA PODIPLOMSKA ŠOLA JOŽEFA STEFANA
JOŽEF STEFAN INTERNATIONAL POSTGRADUATE SCHOOL

Marko Barac

OPTIMIZATION AND APPLICATION OF MEV TIME-OF-FLIGHT SECONDARY ION MASS SPECTROMETRY IN THE STANDARD AND LOW PRIMARY ION BEAM ENERGY MODE

Doctoral Dissertation

OPTIMIZACIJA IN UPORABA MASNE SPEKTROMETRIJE SEKUNDARNIH IONOV Z MERJENJEM ČASA PRELETA V STANDARDNEM IN NIZKEM ENERGIJSKEM NAČINU MEV PRIMARNEGA IONSKEGA ŽARKA

Doktorska disertacija

Supervisor: Dr. Sc. Zdravko Siketić

Co-Supervisor: Prof. Dr. Janez Kovač

Ljubljana, Slovenia, August 2022

In honor of my parents and my wife.
In loving memory of Nono.

Acknowledgments

I could not have imagined better mentors than Dr. Sc. Zdravko Siketić and Prof. Dr. Janez Kovač. Their patience, rationality, kindness, and enthusiasm for the work they do could not have made being their PhD student more enjoyable. I sincerely thank them for passing on their vast knowledge and for always being at my disposal.

For the past few years, a small MeV SIMS team has formed in our lab, of which Dr. Sc. Ivančica Bogdanović Radović and Marko Brajković are indispensable members. Therefore, I thank them for the collaboration on numerous research ideas, brainstorming on all of the challenges we have faced, and celebrating achievements together.

I thank Andrea Ledić and Andrijana Filko from the Forensic Science Centre "Ivan Vučetić" for a wonderful, exciting and fruitful collaboration in their field of forensics of intersecting lines.

Running an accelerator is a difficult task, but technicians Damir Španja and Željko Periša make it look easy. Thank you for doing an enormous job of running both machines, revealing all the tips and tricks to keep them happy and for always being there to fix them when they decide to take a break. I would like to thank Donny Cosic as well, for doing the same and equally important thing with the data acquisition system.

I am thankful to Dr. Sc. Iva Božićević Mihalić together with whom I embarked on the multivariate analysis world and with whom I have been learning, finding new analysis techniques and ways to preprocess the data.

Finally, I would like to express my gratitude to all the rest of my colleagues from the lab, both the permanently residing ones and the passing ones, for the ceaselessly good atmosphere and for always being approachable and ready to help.

I acknowledge the support of the European Union through projects Horizon 2020 (RADIATE grant agreement No. 824096) and COST (Action 16101: Multiforesee), as well as the Center of Excellence for Advanced Materials and Sensing Devices (CEMS), all of which made this work possible.

Finally, I treasure my parents' love and support throughout these years of research, and I am deeply grateful to my wife for the love, patience, and unconditional support she provides every day. Coming home to her and to happiness is what has truly driven and inspired me.

Abstract

Time-of-flight secondary ion mass spectrometry using MeV ions (MeV ToF SIMS) has been around for a few decades as a reliable, surface-sensitive method for the detection of molecular ions having masses up to 1000 Da. It provides excellent lateral resolution of a few μm for imaging of organic samples, making it a superb mass spectrometry technique in fields such as biology, forensics, cultural heritage, etc. In conventional keV SIMS, nuclear stopping predominates and causes a collision cascade that primarily results in the dissociation of larger molecules but is very effective at desorbing atomic ions and small molecules. In contrast, MeV atomic-ion bombardment causes energy loss in the material that is primarily caused by electronic stopping, which is reflected in the "soft" desorption of larger organic molecules. The secondary ion yield is enhanced at higher masses (100-1000 Da) compared to the typical ToF SIMS, and fragmentation of molecules is decreased, although the underlying desorption mechanisms are still not fully understood or explainable by a general theory.

This work investigates the idea of a low energy range (100 keV – 5 MeV) primary ion beam mode in MeV SIMS and its potential for exploiting the capabilities of both conventional keV SIMS and MeV SIMS simultaneously – the analysis of inorganic species, while still being able to sputter and analyze larger organic molecules. This energy mode was named LE (Low Energy) MeV SIMS. Secondary ion yield dependence on the primary ion energy of leucine and various inorganic targets was studied. Next, imaging of a hybrid organic/inorganic target made of Cr and leucine was performed, showing that the contrast between the organic and inorganic area is almost completely diminished when lowering the primary ion beam energy. LE MeV SIMS depth profiling of a dual-layer Cr-ITO sample in a dual-beam mode was also explored, and the obtained depth profile was compared against well-established keV SIMS. Depth profiles demonstrated solid chemical sensitivity to inorganic secondary ions and satisfactory depth resolution, given that a simple sputter source was used for etching. Systematic investigation of MeV ToF SIMS in the low energy regime opens up new possibilities in both the fundamental understanding of the impact of the primary ion stopping power on the detection of secondary ions of organic and inorganic species, and expanding the application of MeV SIMS to analysis, imaging, and depth profiling of inorganic species with increased efficiency.

Furthermore, the increasingly complex, multivariate nature of MeV ToF SIMS datasets often makes the analysis and comparison very hard, possibly leaving crucial information overlooked. This can be tackled by implementing multivariate analysis algorithms standardly used in various other analytical techniques, including the most similar keV SIMS, in order to extract critical, often latent information, and reveal underlying patterns in the data. This proved to be especially beneficial in the MeV SIMS application in the forensics of questioned documents, specifically the imaging of ink intersections.

A novel application of MeV SIMS coupled with particle induced X-ray emission (PIXE) is presented to determine the deposition order of intersecting lines made by various types of writing tools. Principal component analysis (PCA) employed in image processing of the

data from both MeV SIMS and PIXE yielded excellent image contrast that is needed to identify the inks and to determine their deposition order. Only the cases that could not be solved with MeV SIMS were further analyzed by PIXE, which detects elemental information from greater depths. In challenging cases involving liquid-based inks, the combination of approaches proved to be crucial in disclosing the deposition mechanisms and assisted in the resolution of some of them. Next, intersections of several optically identical ballpoint pen inks were studied using non-destructive optical techniques (microscopic and infrared luminescence) that are standardly applied for questioned documents' examination at the Forensic Science Centre "Ivan Vučetić", and MeV SIMS, which is applied at the Ruđer Bošković Institute. The obtained results were compared and discussed. An emphasis is placed on the success of MeV SIMS assisted by t-stochastic neighbor embedding (t-SNE) in differentiating two very similar ballpoint pen inks and determining their deposition order. In general, MeV SIMS also provides chemical information about the studied writing tools, which is an added value. The traces from all the intersections studied so far during this work proved to be distinguishable.

Povzetek

Masna spektrometrija sekundarnih ionov z merjenjem časa preleta z uporabo MeV ionov (MeV ToF SIMS) je že nekaj desetletij uveljavljena površinsko občutljiva metoda za detekcijo molekulskih ionov z masami do 1000 Da. Metoda omogoča odlično lateralno ločljivost nekaj μm za slikanje organskih vzorcev, zato se je pokazala kot zelo uporabna izvedba masne spektrometrije na področjih, kot so biologija, sodna medicina, kulturna dediščina itd. Podobna metoda je keV SIMS, kjer prevladuje interakcija na osnovi zaustavljanja primarnih ionov v polju jeder, kar povzroči kaskado trkov in se kaže v disociaciji večjih molekul s površine ter je učinkovita pri desorpciji majhnih ionov in molekul. V nasprotju z metodo keV SIMS povzroči bombardiranje z ioni energije MeV pri metodi MeV SIMS izgubo energije v materialu ob zaustavljanju primarnih ionov zaradi interakcije z elektroni, kar se odraža v "mehki" desorpciji večjih organskih molekul. Izkoristek detekcije sekundarnih ionov se pri metodi MeV SIMS v primerjavi z metodo keV SIMS poveča pri večjih masah (100-1000 Da), fragmentacija molekul pa se zmanjša, vendar osnovni mehanizmi desorpcije še vedno niso popolnoma razumljeni ali teoretično razloženi.

To delo obravnava uporabo primarnega ionskega snopa v nizkem energijskem območju (100 keV – 5 MeV) pri metodi MeV SIMS in možnost, da bi hkrati izkoristili prednosti metod keV SIMS in MeV SIMS za analizo anorganskih materialov, pri čemer bi še vedno lahko učinkovito analizirali tudi večje organske molekule. Ta nizko-energijski način je bil poimenovan LE (ang. Low Energy) MeV SIMS. Raziskali smo odvisnost izkoristka detekcije sekundarnih ionov od energije primarnega ionskega žarka za levcin in različne anorganske materiale. Nato smo izvedli slikanje heterogene organsko-anorganske tarče iz Cr in levcina, ki je pokazalo, da kontrast med organskim in anorganskim območjem skoraj popolnoma izgine, ko se zniža energija primarnega ionskega žarka. Izvedli smo tudi globinsko analizo z metodo LE MeV SIMS dvoplastne strukture Cr-ITO z dvema ionskima žarkoma. Dobljeni globinski profil je bil primerjan z globinskim profilom, dobljenim s konvencionalno metodo keV SIMS. Globinski profili so pokazali visoko kemijsko občutljivost za anorganske sekundarne ione in zadovoljivo globinsko ločljivost glede na to, da je bil za ionsko jedkanje uporabljen preprost izvor ionov. Sistematična raziskava uporabnosti metode MeV ToF SIMS v nizkoenergijskem režimu odpira nove možnosti tako pri temeljnem razumevanju vpliva zaustavljanja primarnih ionov na zaznavanje sekundarnih ionov iz organskih in anorganskih materialov kot za uporabe MeV SIMS za analizo, slikanje in globinsko analizo anorganskih materialov z večjo učinkovitostjo.

Poleg tega je zaradi vse bolj kompleksne in večplastne narave podatkov, dobljenih z metodo MeV ToF SIMS, te pogosto težko analizirati in jih primerjati, zaradi česar so lahko spregledane ključne informacije. To je mogoče izboljšati z implementacijo algoritmov multivariatne analize, ki se standardno uporabljajo v različnih drugih analitičnih tehnikah, vključno z najbolj podobno metodo keV SIMS, da bi izluščili kritične, pogosto skrite informacije in razkrili osnovne povezave v podatkih. To se je izkazalo za posebej koristno pri uporabi metode MeV SIMS v forenziki spornih dokumentov, zlasti pri slikanju presečišč črt iz črnila.

Predstavljena je nova uporaba metode MeV SIMS v povezavi s spektroskopijo ionsko vzbujenih rentgenskih žarkov (PIXE) za ugotavljanje vrstnega reda nanašanja križajočih se črt iz različnih pisal. Analiza glavnih komponent (PCA), uporabljena pri obdelavi slik, dobljenih z metodama MeV SIMS in PIXE, je dala odličen kontrast slik, ki je potreben za prepoznavanje črnil in določitev vrstnega reda njihovega nanašanja. Le primere, ki jih ni bilo mogoče razumeti z metodo MeV SIMS, smo nadalje analizirali z metodo PIXE, ki zazna elementarne informacije iz večjih globin. V zahtevnih primerih, ki so vključevali tekoča črnila, se je kombinacija pristopov izkazala za ključno pri razumevanju načina nanašanja. Nadalje smo raziskali več primerov prekrivanj črt iz različnih črnil z uporabo ne-destruktivnih optičnih metod (mikroskopija in infrardeča luminiscenca), ki se standardno uporabljajo za pregled sumljivih dokumentov v forenzičnem centru "Ivan Vučetić", in z uporabo metode MeV SIMS na Inštitutu Ruđer Bošković. Primerjali smo dobljene rezultate obeh metod. Uspešna je bila uporaba metode MeV SIMS v kombinaciji z metodo t-porazdeljena stohastična vdelava soseda (t-SNE) pri razlikovanju dveh zelo podobnih črnil za pisala in ugotavljanju vrstnega reda njunega nanašanja. Metoda MeV SIMS daje tudi dodatno informacijo o kemični sestavi črnila iz pisalnih orodjih. V okviru tega dela smo uspeli razložiti vse prekrivajoče se sledi črnila.

Contents

List of Figures **xv**

Abbreviations **xvii**

1 Introduction **1**
1.1 Thesis Structure . . . 1
1.2 Secondary Ion Mass Spectrometry (SIMS) . . . 2
1.3 MeV SIMS . . . 2
1.4 Interaction of Ion Beam with Solid Matter . . . 3
1.4.1 Electronic and nuclear stopping . . . 3
1.4.2 Sputtering theory . . . 6
1.4.2.1 Collision cascade desorption . . . 7
1.4.2.2 Hit theory . . . 9
1.4.2.3 Thermal models . . . 10
1.4.2.4 Pressure pulse model . . . 11
1.5 MeV ToF SIMS Setup at RBI . . . 13
1.6 Multivariate Analysis Methods . . . 16
1.6.1 Principal component analysis . . . 17
1.6.2 T-distributed stochastic neighbor embedding . . . 21
1.6.3 MVA in the SIMS community . . . 22
1.7 Motivation and Thesis Objectives . . . 23

2 Optimization of MeV ToF SIMS Technique in the Low Primary Ion Beam Energy Mode for the Analysis of Inorganic Materials **25**
2.1 MeV ToF SIMS Analysis of Hybrid Organic/Inorganic Compounds in the Low Energy Region . . . 26
2.2 Depth Profiling of Cr-ITO Dual-Layer Sample with MeV SIMS Using Ions in the Low Energy Region . . . 34

3 Application of MeV ToF SIMS in the Standard Primary Ion Beam Energy Mode in Forensics of Questioned Documents, Supported by MVA Image Analysis **41**
3.1 Determination of Deposition Order of Toners, Inkjet Inks, and Blue Ballpoint Pens Combining MeV SIMS and PIXE . . . 42
3.2 Comparison of Optical Techniques and MeV SIMS in Determining Deposition Order Between Optically Distinguishable and Indistinguishable Inks from Different Ballpoint Pens . . . 52

4 Conclusions **75**

Appendix A LE MeV SIMS Spectra of Selected Inorganic Targets **77**

References **79**

Bibliography **87**

Biography **89**

List of Figures

Figure 1.1: Total stopping power for Cu in Cr. 5
Figure 1.2: Collision cascade sputtering of atoms and molecules. 8
Figure 1.3: Thermal models of desorption. 10
Figure 1.4: Pressure-volume curve for a liquid-gas phase transition. 11
Figure 1.5: Pressure pulse model. 12
Figure 1.6: Layout of experimental beamlines at the RBI accelerator facility. 13
Figure 1.7: MeV ToF SIMS setup at the RBI accelerator facility 14
Figure 1.8: ToF SIMS spectrometer mounted on the RBI microbeam station. . . . 16
Figure 1.9: Measured data represented in a matrix. 17
Figure 1.10: A schematic of PCA transformation on a two-variable system. 18
Figure 1.11: A schematic description of Eq. 1.29 (PCA). 19
Figure 1.12: Explanation of eigenvectors and eigenvalues. 19
Figure 1.13: Principal components outcome of two classes of bacteria. 20
Figure 1.14: Comparison of PCA and t-SNE. 22

Figure A.1: Inorganic samples selected for LE MeV SIMS measurement. 77
Figure A.2: LE MeV SIMS spectra of selected inorganic samples. 78

Abbreviations

1D	...	One-dimensional
2D	...	Two-dimensional
3D	...	Three-dimensional
AFM	...	Atomic Force Microscopy
ERDA	...	Elastic Recoil Detection Analysis
eV	...	Electron Volt
GPU	...	Graphics Processing Unit
HV	...	High Voltage
IPS	...	International Postgraduate School
ITO	...	Indium Tin Oxide (In_2O_5Sn)
JSI	...	Jožef Stefan Institute
MALDI	...	Matrix-Assisted Laser Desorption/Ionization
MCP	...	Microchannel Plate Detector
MCR	...	Multivariate Curve Resolution
MOSFET	...	Metal-Oxide Semiconductor Field-Effect Transistor
MVA	...	Multivariate Analysis
NMF	...	Non-negative Matrix Factorization
OLED	...	Organic Light-Emitting Diode
PCA	...	Principal Component Analysis
PIXE	...	Particle Induced X-ray Emission
RBI	...	Ruđer Bošković Institute
RBS	...	Rutherford Backscattering Spectrometry
SIMS	...	Secondary Ion Mass Spectrometry
SRIM	...	Stopping and Range of Ions in Matter
STIM	...	Scanning Transmission Ion Microscopy
TOF	...	Time-Of-Flight
t-SNE	...	t-distributed Stochastic Neighbor Embedding
XPS	...	X-ray Photoelectron Spectroscopy

Chapter 1

Introduction

1.1 Thesis Structure

This thesis is conceptualized as a series of four author's articles published in the international peer reviewed journals during his doctoral research within the scope of megaelectron volt secondary ion mass spectrometry. It is organized in three main chapters, with Chapter 1 being an Introduction, and Chapters 2 and 3 composed of published articles. Chapter 1 covers the necessary context of the presented research: theoretical background on the physical processes that occur upon interaction of an ion beam with a solid, a description of MeV ToF SIMS experimental setup at Ruđer Bošković Institute where the research was conducted, and a mathematical description of multivariate analysis methods most commonly used in the SIMS community. Finally, the last subchapter in Chapter 1 is dedicated to the description of motivation and main thesis objectives, which are then addressed in the following Chapters. Chapter 2 deals with the fundamental research conducted on MeV SIMS that involves optimization of the technique in the non-standard, low primary ion beam energy mode with the objective to analyze inorganic and/or hybrid organic/inorganic materials. Two articles are presented in this Chapter, one demonstrating a systematic feasibility study of various targets (organic, inorganic) and imaging of a hybrid sample, and the other article covering an attempt in MeV SIMS depth profiling of an inorganic dual-layer sample. Chapter 3, on the other hand, deals with exploring MeV SIMS potential in application to forensics of questioned documents, specifically determination of deposition order of intersecting ink lines from different writing tools, supported by multivariate analysis of imaging data. Here, the standard MeV primary ion beam energy is used, which is optimal for the detection of organic species. This is covered within two published articles, one demonstrating a feasibility study involving MeV SIMS analysis of inks from various different types of writing tools and combining MeV SIMS and PIXE in problematic cases, and the other paper covering a comparison of MeV SIMS and standard optical techniques used in forensics of questioned documents on two sample categories: optically distinguishable and indistinguishable. Chapter 4 elaborates and concludes the results presented in the thesis and offers insight on future prospects and potential in further development and impact of both the fundamental research of the low energy MeV SIMS, as well as MeV SIMS application in forensics.

1.2 Secondary Ion Mass Spectrometry (SIMS)

When a beam of ions strikes a surface of solid material, the energy transferred by incident particles causes a collision cascade that sets several atomic layers in motion and is accompanied by complex processes of energy transfer (elastic or non-elastic collisions) in the surface zone of the solid. It results in the emission of electrons, photons, atoms and molecules (neutral and charged). All the emitted ion species can be extracted into a mass spectrometer where they can be differentiated and detected by a mass analyzer. The emitted ions are called secondary ions and the method is therefore called secondary ion mass spectrometry (SIMS) [1].

A focused keV ion beam is used for sputtering of secondary particles in most of the available commercial SIMS instruments. The mechanism of interaction of keV ion beam with the sample structure is mainly based on nuclear stopping, which can be described as elastic collisions between the impinging ion and the target nuclei inducing atomic displacements and phonons. Conventional (keV) SIMS instruments are commercially available as bench-top systems and are used in a wide variety of scientific research fields. Applications range from dopant profiling in semiconductor research [2], [3] to trace element analysis in geology, cultural heritage [3] or biomedicine [4]–[6]. Spatial resolutions of 50 nm are possible for imaging [7], [8], which is superior over other molecular imaging techniques such as Matrix Assisted Laser Desorption/Ionization (MALDI) [4], [6]. Typical secondary ion mass range is up to 1000 Da [9], [10]. Isotopes can be separated with a high mass resolution $M/\Delta M$ of up to 10^4 [11].

1.3 MeV SIMS

MeV SIMS is a variation of conventional SIMS using a primary ion beam produced in an MV particle accelerator instead of keV ions. In the last couple of years several setups were designed at the accelerator facilities worldwide utilizing focused MeV heavy ions for the target excitation [12]–[16]. With MeV ions, it is possible to significantly increase the ion yields from intact molecules [17]–[19]. MeV SIMS uses primary ion beams with energies of a few to tens of MeV. Therefore, electronic stopping is much more prevalent and energy is transferred fast, which leads to rapid heating [20]. This way higher molecular secondary ion yields can be reached in comparison to conventional keV SIMS [21]. Mass range can extend up to 20000 Da [22]–[24].

Recently dedicated MeV SIMS experiments have been developed with imaging capability [21], [25], [26]. The instruments are relatively big (of the order of tens of meters) and quite expensive and complex in design and usage, thus MeV SIMS is developed only in the laboratories already equipped with MV accelerators commonly used for the Ion Beam Analysis (IBA). Regardless, they have higher flexibility in beam types, with the benefit of higher molecular yields. Yield increases of several orders of magnitude have been reported for heavy secondary ions, e.g. an increase of a factor of 1000 for a peptide at mass 1154 Da in comparison to keV SIMS [12]. A mass range of up to 1200 Da has so far been demonstrated for MeV SIMS imaging [12] and spatial resolutions of below 1 micrometer [27] have been reported. Applications of MeV SIMS can be found in several fields, among them biomedical research [26], [28], surface chemistry [29], forensics [30] and cultural heritage studies [31]. Most studies focus on as high a mass range as possible because heavy secondary ions can significantly improve the understanding of the surface chemistry as they simplify data interpretation. Knowledge of heavier species present in the spectra makes it easier to identify lighter fragments and chemical bonding states on the surface of the sample. MeV SIMS is particularly interesting for molecular imaging

in biomedical research. Typical cell sizes of mammalian cells are of the order of 10 µm [32], which cannot be resolved by other high mass range techniques. MeV SIMS has the potential for even smaller beam diameters and is, therefore, able to extend the secondary ion mass range for cell imaging [33].

1.4 Interaction of Ion Beam with Solid Matter

When an energetic ion impinges on a surface, it starts a collision cascade: the projectile dissipates its energy by collisions with the target atoms, and if these are energetic enough, they collide with other atoms. These collisions can be described as elastic in a sense that energy loss to electrons during the collision can be neglected, which is the case in keV SIMS. A fraction of the projectile energy will be dissipated to the electronic cloud of the target nuclei. Electronic energy loss due to such inelastic collisions is the prevalent process in MeV SIMS. The resulting stopping of the ion determines the range distribution of the projectile ion. The collision cascade is important for determining the number of recoils set in motion in the target by the projectile. This determines the amount of damage and its distribution in the target, and also the atomic relocation and hence mixing in non-elemental targets, as well as surface-topographical changes. The latter range from atomic roughness (adatoms, surface vacancies) to the information about the formation of craters and of even large-scale surface structures, such as ripples. Finally, the number of energetic recoils generated close to the surface determines the sputtering of the target in keV SIMS, while in MeV SIMS, several theories are used to explain the ejection of species as a consequence of high electronic energy density deposition within the first few monolayers of the material. While the sputtering process is of fundamental interest to SIMS since it forms its basis, all processes mentioned above are important and contribute to changing the target under irradiation. [34]

The understanding of ion stopping and ion-induced processes in materials started with analytical calculations of stopping, range theory and cascade theory in the 1960s. After this pioneering work, cascade theory has been refined both to widen its scope by including low energy projectile ions, the study of non-elemental targets, the prediction of the angular distribution of sputtered particles, etc., and also by refining the quality of its predictions. A more careful calculation of interatomic interaction potentials proved important. Besides analytical approaches, numerical and simulation schemes were applied to the study of cascades. While in the late 1970s and 1980s Monte Carlo and Binary Collision Approximation codes such as TRIM [35] or MARLOWE [36], [37] were frequently applied, in the last few decades molecular-dynamics simulations have found a more and more widespread application. [34]

1.4.1 Electronic and nuclear stopping

The stopping power of a material for a particle is a measure of the average energy loss per unit path length of the particle due to interactions in the material. It is consequently defined as:

$$S = -\frac{1}{N}\frac{\mathrm{d}E}{\mathrm{d}x} \tag{1.1}$$

where N is the number density of absorber atoms per unit area, E is the kinetic energy of the particle and x is the distance along the particle trajectory in the material. By the definition in Eq 1.1, S is strictly speaking a force (not a power). The term stopping force has indeed been proposed, but the term stopping power is deep-rooted in the field and broadly accepted. The theoretical framework for a general treatment of energy loss to the

nuclei as well as to the electrons, i.e., the electronic system, was comprehensively treated by N. Bohr [38] and J. Lindhard [39] in a number of important papers.

To the first order, the stopping power of a target for an ion depends on the ion energy E and atomic number Z_1, as well as on the density and the atomic number Z_2 of the target elements. The bombardment of a solid target with an ion beam will initiate collisions with the nuclei and the electrons. The former events will cause a large-angle scattering, whereas for the latter any significant deflection of the primary particle will be excluded. The interaction mechanisms by which the ion can lose energy, dependent on the ion's velocity, are:

- excitation or ionization of the electrons in the target (electronic energy loss),
- elastic collisions with the nuclei of target atoms (nuclear energy loss),
- radiative emission of energy.

Thus, the total stopping power can be divided into three independent parts:

$$S_{\text{tot}} = S_{\text{nuclear}} + S_{\text{electronic}} + S_{\text{radiative}} \tag{1.2}$$

At projectile energies and masses involved in keV and MeV SIMS, the term $S_{radiative}$ can be neglected. It becomes significant only for very light projectiles such as electrons, or at very high projectile energies, due to the emission of bremsstrahlung in the electric field of the particles in the material traversed.

Elastic collisions with the target nuclei dominate at ion velocities v significantly lower than the Bohr velocity v_B (2.188 x 10^8 cm/s). As the ion velocity increases, the nuclear energy loss diminishes as $1/E$. In the velocity range $v \sim 0.1 v_B$ to $Z_1^{2/3} v_B$ (known as the Thomas-Fermi velocity), the electronic energy loss (i.e. collisions with electrons in the target) starts becoming the main interaction mechanism and is roughly proportional to velocity ($E^{1/2}$). At velocities $v \geq Z_1^{2/3} v_B$, the ion starts to get stripped of electrons and the charge state of ion increases. At this point, the projectile can be regarded as a positive point charge Z_1, and the (electronic) stopping power starts to decrease as the projectile spends less time in the vicinity of the target electron. An example of the total stopping power in a Cr target for a Cu beam is shown in Figure 1.1.

Both the nuclear and the electronic energy loss for ion velocities below the Thomas-Fermi velocity can be estimated with the Lindhard-Scharff theory based on quasi-elastic collisions. An important scaling parameter is Lindhard's reduced energy ε [39]:

$$\varepsilon = \frac{a_L M_2}{Z_1 Z_2 e^2 (M_1 + M_2)}\, E, \tag{1.3}$$

where $e^2 = 1.44$ eV nm and a_L is the Lindhard screening length, given by:

$$a_L = \frac{0.8853\, a_B}{\left(Z_1^{2/3} + Z_2^{2/3}\right)^{1/2}}, \tag{1.4}$$

with $a_B = 0.053$ nm being the Bohr radius. The nuclear stopping power expressed in reduced units can be formulated by a universal scattering function $f(t^{1/2})$:

$$s_{\text{nuclear}}(\varepsilon) = \frac{d\varepsilon}{d\rho} = \frac{1}{\varepsilon} \int_0^{\varepsilon} f(t^{1/2}) dt^{1/2}, \tag{1.5}$$

where $t = \varepsilon^2 (T/T_m)$, with T being the recoil energy and $T_m = (4 M_1 M_2/(M_1 + M_2)^2) E$ the maximum possible energy transferred to the electron and lost by the ion in the collision,

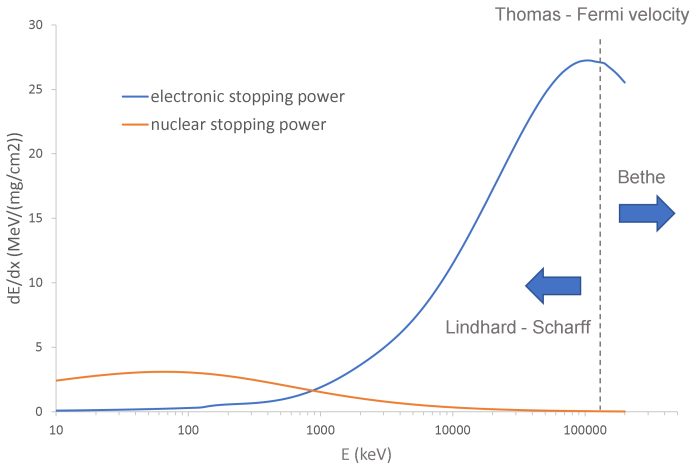

Figure 1.1: Total stopping power for a copper primary beam in a Cr target. Two regimes for electronic stopping power are described based on Lindhard-Scharff and Bethe theory, with regard to the Thomas-Fermi velocity as a maximum of the electronic stopping curve. Simulation was done in SRIM-2013.

ε is Lindhard's reduced energy, and ρ is the reduced length based on a cross section πa_L^2 and an energy ratio T_m/E:

$$\rho = LN4\pi a_L^2 \frac{M_1 M_2}{(M_1 + M_2)^2}, \tag{1.6}$$

where L is a measure of length in the laboratory frame. The nuclear stopping power in practical units can then be expressed as:

$$S_{\text{nuclear}}(E) = \frac{\pi a_L^2 T_m}{\varepsilon} s_{\text{nuclear}}(\varepsilon) \tag{1.7}$$

The absolute magnitude is determined partly by the ε in the denominator of the conversion factor, which means that for heavy atoms on a heavy target ε becomes small and, in turn, leads to a large nuclear stopping. The maximum of the nuclear stopping, which for the classical Thomas–Fermi model occurred at $\varepsilon \cong 0.3$, is therefore shifted to higher energies for heavy projectiles. [40]

The electronic stopping, on the other hand, has different forms at high and low velocities, with the limit being the Thomas-Fermi velocity, $v_B Z_1^{2/3}$. At lower velocities $v < v_B Z_1^{2/3}$, the Lindhard-Scharff model is still applicable, but at high velocities $v > v_B Z_1^{2/3}$, Bethe's or Bohr's theory becomes appropriate. The two regions are highlighted in Figure 1.1 for the case of Cu beam in Cr target.
According to the Lindhard-Scharff theory, the electronic stopping power can be expressed in reduced units as [41]:

$$s_{\text{electronic}}(\varepsilon) = k_L \varepsilon^{1/2} \tag{1.8}$$

where the constant of proportionality k_L depends on the atomic number and the mass of the beam ion and the target atom. The electronic stopping is thus proportional to the velocity ($\varepsilon^{1/2}$) and can be converted to real units with the same factor as the reduced nuclear stopping cross-section in Eq. 1.7.

According to the Bethe's equation for high velocities ($v > v_B Z_1^{2/3}$), based on a first-order perturbation treatment, the electronic stopping can be expressed as [42]:

$$S_{\text{electronic}}(E) = \frac{4\pi Z_1^2 Z_2 e^4}{m_e v^2} \ln \frac{2 m_e v^2}{I}, \tag{1.9}$$

where I is the average excitation energy in electron volts, which for most elements is roughly $I \cong 10 Z_2$. In case of projectiles with high atomic number, the quantum treatment proposed by Bethe is replaced by Bohr's expression derived for a harmonic oscillator:

$$S_{\text{electronic}}(E) = \frac{4\pi Z_1^2 Z_2 e^4}{m_e v^2} \sum_{\nu=1}^{Z_2} \ln \frac{C m_e v^2}{Z_1 e^2 \omega_\nu}, \tag{1.10}$$

where ω_ν is a characteristic frequency of each electron level of the target atom. Here, Z_1 appears in the logarithm as an influence on the position of the stopping maximum.

The expressions 1.9 and 1.10 for the electronic stopping power are derived under the assumption that the incoming ion is fully stripped due to all electrons having velocities less than the ion velocity. The effective charge state (i.e. ion charge fraction) of the incoming heavy ion according to Bohr's estimate is [38]:

$$\frac{Z^\star}{Z} = \left(\frac{v}{v_0 Z_1^{2/3}} \right), \tag{1.11}$$

where Z is the total number of electrons in the ground state ion, and $Z^\star$ is the positive charge on the ion. The difference $Z - Z^\star$ is the number of electrons remaining on the ion. Evidently, the average ion charge state increases with the ion velocity. However, regardless of the initial ion charge state, which may be very far from the equilibrium charge state, an ion beam will approach charge state equilibrium after having penetrated a few layers from the surface. Expression in Eq. 1.11 in fact explains the two different regions of electronic stopping due to the two extreme states of an energetic ion.

1.4.2 Sputtering theory

When an energetic ion impinges on a target surface, the deposited energy density close to the projectile path through the solid becomes extremely high and causes extensive fragmentation of target molecules. But over time, locally deposited energy diffuses outwards from the initially excited region. Eventually, several different kinds of species are desorbed from the target, including neutral and charged, fragments and intact molecules. Therefore, sputtering is the erosion of material surfaces by particle impact. The variety of materials for which sputtering has been or can be observed is virtually unlimited. The standard source of bombarding particles in the laboratory is a collimated ion beam with a well-defined energy, but both electrons and photons as well as neutrons and other particles may give rise to sputter phenomena. Sputtering is a phenomenon on the atomic scale: one can identify an individual sputter event, i.e. the emission of a number of atoms or molecules from a material surface initiated by a single bombarding particle. A sputter event is a priori statistical in nature. However, after bombardment with a great number of particles, macroscopic effects such as a change in weight can be observed, and a crater may be visible on the target area facing the beam. Such macroscopic phenomena are quasi-deterministic and allow the operational definition of terms such as erosion rate and sputter yield. A desorption event in response to an energetic projectile impact is the result of a large number of processes, all of which are amenable to theoretical treatment. In the case of keV atomic and cluster projectile impact, target particle motion is directly excited,

but in the case of MeV atomic projectiles, as in MeV SIMS, target particles are set in motion indirectly through relaxation of electronically deposited energy. This conversion occurs via relaxation of repulsive electronic states (as in the case of a Coulomb explosion, for example), molecular expansion after vibrational excitation, or chemical energy release. Several desorption processes can occur: 'direct' desorption processes in which a particular molecule is ejected due to its own repulsive interactions with neighbouring molecules, or 'indirect' desorption processes which reflect the spatial evolution of energy to regions quite far beyond that in which energy is initially deposited. Finally, further evolution in energized species during and after desorption may modulate the charge state and degree of clustering or fragmentation, determining critically what species is eventually detected far away from the sample. [43]

The collision cascade theory is a well-established and generally accepted theory in describing sputtering induced by keV ions. Here however, due to nuclear interactions and high energy density deposited, the fragmentation of ejected molecules is pronounced. This results in limited analytical mass range of secondary ions. On the other hand, when the electronic excitations are the prevailing reason for species ejection, there is no generally accepted theory. Several of theoretical models coexist, and they need to be carefully treated to describe the physical conditions in question. The hit theory, thermal models of desorption and the pressure pulse model each tend to refer only to the part of the process that starts with ion impact and ends with the formation of secondary particles, neutral and ionized. Because currently available experimental evidence suggests that larger ejected molecules come from relatively far away from the region that is initially energized, ejection mechanisms characterized by "indirectness" or "collective motion imparted at a distance" seem to currently be the most satisfactory. [43]

Key points of mentioned desorption models are summarized from P. Sigmund's chapter on sputtering theories [43] in the following sections.

1.4.2.1 Collision cascade desorption

In general, the collision cascade model is best suited for situations in which the primary ions impacting the materials have keV energies. As mentioned in the previous section, the ion velocity in this velocity region is less than the Bohr velocity, and the predominant process involves interaction with the target via screened elastic nuclear collisions. As long as the energy density is not too high, which is the case when most atoms in the energized region are in motion, or when moving atoms collide with other moving atoms rather than with atoms at rest, the total ensemble of energized atoms is referred to as a collision cascade. A schematic depiction of sputtering via collision cascade for atoms and molecules is described in Figure 1.2. Sigmund's [44]–[46] collision cascade theory for atomic solids is well-established and thoroughly described. For low incident particle kinetic energies and high desorbed atom kinetic energies, the theory describes the desorbed atom kinetic energy spectrum scaling as E^{-2}. The sputtering yield is proportional to the nuclear stopping power $(dE/dx)_n$. The model accurately describes the sputtering of metal targets by keV atomic ions, however, generalizing the collision cascade theory to a molecular solid is a difficult task. The atomic collision cascade model, according to Hoogerbrugge and Kistemaker [47], is able to describe the initial energetic portion of the collision cascade, but "in a later, low energy, stage of the cascade, the presence of relatively strong bonds forces the complete molecules to participate in the collisions and the atomic picture loses its value." Schematic diagrams at these extremes are depicted in Figure 1.2.b and c. A statistical model is one of the theoretical approaches to collision cascade sputtering of molecules that focuses somewhere in-between the atomic and molecular picture: a surface molecule is assumed to be impacted from below by several atoms with a kinetic energy

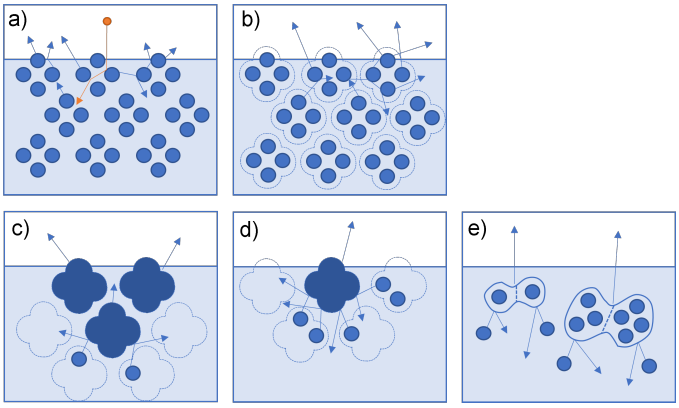

Figure 1.2: Schematic diagrams of collision cascade sputtering of atoms and molecules. a) Collision cascade in an atomic solid. Five atoms are sputtered. b-d) Collision cascades in an organic solid. b) At early times, the cascade has an atomic character. c) At late times, the cascade has a molecular character. d) One molecule being ejected by several atoms impacting from below. e) Statistical models. Left: Haring's model, right: model of Hoogerbrugge and Kistemaker. Acquired from [43].

distribution $N(E) \propto E^{-2}$ (Figure 1.2.d). Haring et al. [48] used a statistical model to calculate the kinetic energy and angular distributions of desorbed diatomic molecules, and they extended their findings to larger polyatomic molecules. Each target atom in the desorbed polyatomic molecule is assumed to have been impacted by a moving atom from the substrate below, gaining kinetic energy as if in a collision cascade (isotropic velocity distribution and $N(E) \propto E^{-2}$). The target atoms' momenta are assumed to be uncorrelated. The final desorbed molecule parameters are calculated in the same way that they are in standard collision cascade theory. The desorbed molecule kinetic energy spectrum scales as $E^{0.5-2.5m}$ in case of large kinetic energies for a polyatomic molecule of m atoms, each impacted by one recoil from the substrate. The steep energy distribution indicates fragmentation of the polyatomic molecule in cases of too high internal energy. Hoogerbrugge and Kistemaker [47] have extended Haring's model in the sense that a polyatomic molecule containing $m > 2$ atoms is considered to be impacted by exactly two atoms in a collision cascade. Each atom from below the surface is assumed to collide with a portion, or "sub-unit", of the molecule to be desorbed (Figure 1.2.e). In this case, the desorbed molecule kinetic energy distribution scales as $E^{-4.5}$ for high kinetic energies.

On the other hand, Garrison [49] has employed a classical dynamics simulation to demonstrate that collision cascade sputtering of organic molecules is indeed feasible, which showed that a cascade is capable of ejecting large intact organic admolecules from the surface, but they had to be struck simultaneously by two or three atoms from the solid. This led to a conclusion that in order to induce desorption of intact molecular species with sufficiently low internal energy (and avoid fragmentation), a "collective" desorption process needs to occur in a form of a "push" in the same general direction by several atoms colliding in the underlying solid.

As for the case of bio-organic molecule desorption, collision cascade theory has mostly been applied in sputtering experiments of glycerol molecular ions. Generally, asymptotic power laws were observed [50]. Even though collision cascade desorption was evidently present in glycerol liquid matrices, the model could not explain the dominant fraction of the yield. Yen et al. [51] have later found the glycerol ion sputtering yield scaling as $[(dE/dx)_n - C]^2$, where $(dE/dx)_n$ is the nuclear stopping power and C is a threshold pa-

rameter, whereas the collision cascade model predicted linear scaling with $(dE/dx)_n$. The low energy desorbed molecular ions are suspected to be produced by a thermal bulk desorption mechanism, or a pressure pulse, whereas the high energy sputtered ions probably originate as a result of a collision cascade early on.

1.4.2.2 Hit theory

The hit theory is one of the approaches to treating organic molecule desorption in cases of MeV atomic ion impact, where energy transfer is governed mainly by electronic stopping. According to the ion track model by Hedin et al. [52], a primary ion is slowed down in the target along a cylindrical infratrack of radius of about 5 Å. Here, about 50 % of energy is deposited, and the rest is transferred to the ultratrack of a much larger radius via energetic secondary electrons (delta rays) originating from the infratrack which create electronic excitations and ionize the surrounding bulk. The hit theory has been used to explain the observed behavior of the ion desorption yield with respect to the electronic stopping power $(dE/dx)_e$. Katz [53] first introduced the idea of hit theory, whereas the application to desorption was added by Hedin et al. [52]. The concept relies on a condition that a surface molecule will be desorbed as an ion only if it receives at least i_{min} "hits" from delta rays. A molecule is assumed to be exposed to a flux of delta rays as a result of an MeV atomic ion passage through the bulk, and if it is to be desorbed intact, all internal bonds should remain intact, and some external bonds should break. The hit theory deals with modifications of these bonds in a statistical manner, describing the number of hits experienced by a molecule by a Poisson distribution. The desorption yield of molecular ions is then calculated as an integral over the surface with the ion track at the center:

$$Y = P_{ion} Z_{avg} n_m \int_{r_d^2}^{\infty} \pi d(r^2) e^{-\eta_F(r)} \sum_{i=i_{min}}^{\infty} \frac{\eta_D^i(r)}{i!} e^{-\eta_D(r)} \tag{1.12}$$

where two proportionality constants appear: the probability of desorption of a molecule as an ion P_{ion}, and the average depth from which ion desorption originates Z_{avg}. Two key quantities,

$$\eta_F(r) = \frac{\varepsilon(r)}{n_m W_F} \ , \ \text{ and } \ \eta_F(r) = \frac{\varepsilon(r)}{n_m W_F} \ , \tag{1.13}$$

denote the average number of internal and external broken bonds, respectively, in a molecule at perpendicular distance r from the ion track, with n_m being the molecular number density, W_F a bond breaking energy, and $\varepsilon(r) \propto \frac{(dE/dx)_e}{r^2}$ the energy density deposited by delta rays at a distance r. Complete fragmentation is taken into account with the lower integration limit r_d, which is roughly the radius of the target molecule, when the incident ion directly collides with the molecule. The predicted ion yield scaling follows $Y \propto (dE/dx)_e$ for large $(dE/dx)_e$, and a steeper $Y \propto (dE/dx)_e^n$ for smaller $(dE/dx)_e$, with $n > 1$.

The model appears to be very useful in the description of a small amount of ionization given the dominant desorption of neutral molecules. However, it takes the ionization probability into account only through a proportionality constant, failing to explain some experimental observations, such as $Y \propto (dE/dx)_e^3$ behavior of small neutral biomolecules [54]. Furthermore, the model is unclear in accounting for observed similarities [55] between SIMS spectra generated upon keV and MeV atomic-ion impact, given that a lot less delta rays are generated in the former case.

1.4.2.3 Thermal models

Thermal models of desorption assume that the energy deposited upon ion impact is localized within a small volume which is called a thermal (or elastic) spike if the target particles receive a significant amount of kinetic energy. This region can be characterized by a temperature $T(\mathbf{r}, t)$ as a function of perpendicular distance from the track and time passed from ion impact, since the energized region eventually dilutes and cools down completely due to heat conduction. Additionally, the track temperature is also dependent on the thermal diffusivity. Two approaches to thermal theory of desorption exist: activated desorption, which describes the evaporation from the energized region molecule by molecule, and bulk desorption, in which a bulk of the material spontaneously vaporizes as a whole. Both variants are shown in Figure 1.3.

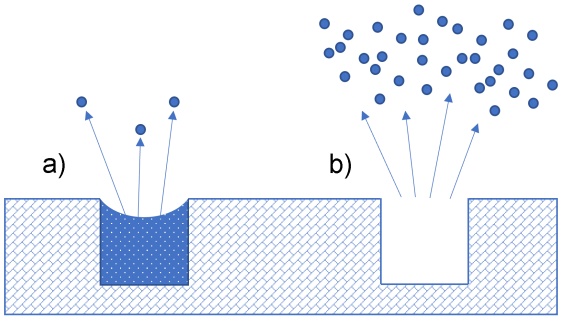

Figure 1.3: Schematic diagrams of thermal desorption mechanisms. a) Activated desorption (evaporation). b) Bulk desorption after an irreversible transition into the gas phase. Acquired from [43].

An expression for the evaporative desorption yield due to thermal spike can be described as an integral over the surface:

$$Y = \int_0^\infty dt \int_0^\infty 2\pi r dr \Phi[T(\mathbf{r}, t)] \tag{1.14}$$

where Φ is the thermally activated particle flux evaporating from the surface, for which a simple Arrhenius form for an ideal gas can be employed $\Phi \propto exp(U/kT)$, where U is the surface binding energy, n_m is molecular number density, M is the molecular mass, k is the Boltzmann constant. For a very narrow initial (cylindrical) thermal spike, the yield scales as $Y \propto (dE/dx)_e^2$, whereas if the spike has larger initial width, the yield scales abruptly as $Y \propto (dE/dx)_e^2$ for smaller $(dE/dx)_e$ values, but follows $Y \propto (dE/dx)_e$ for larger $(dE/dx)_e$ values.

When a molecule gains enough thermal energy to evaporate, it should also get enough internal energy to dissociate. Attempts to address this problem were made in several studies because of the vagueness of the evaporative thermal spike model in this regard. Lee and Lucchese [56] suggested that thermal desorption with "cool" internal modes is possible. They have calculated stochastic classical trajectories of a model system in response to a temperature pulse and found that the internal energy of the adsorbed molecule remained low and increased rather slowly up to the total thermal spike dissipation. They also monitored the center-of-mass motion of the adsorbed molecule with respect to the substrate represented by several atoms. The substrate suffered large fluctuations during thermal excitation, consequently pushing the molecule, which led to desorption. The authors concluded that the desorption of a molecule in the context of the evaporative thermal

spike model is possible without significant fragmentation only if the equilibrium between translational and internal modes is not reached prior to desorption.

The idea of bulk desorption process has been modeled by a number of approaches ranging from thermodynamics [57], molecular dynamics simulations [58], [59], even adiabatic expansion [60]. The mechanism of bulk desorption is alternatively referred to as gas-flow or phase-explosion desorption. The simplest thermodynamical approach starts with a pressure-volume (p-V) diagram for a material that undergoes a liquid-gas phase transition (Figure 1.4).

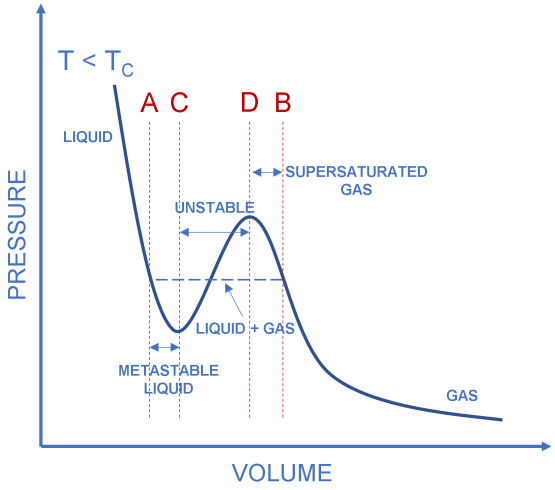

Figure 1.4: Pressure-volume curve for a material undergoing a liquid-gas phase transition. Segment A-C represents a metastable liquid; segment D-B represents a supersaturated gas; and segment C-D represents an absolutely unstable state of the liquid, characterized by an irreversible transition to the vapor phase. Acquired from [43].

The pressure decreases by increasing the volume, but for temperatures below the critical temperature T_C, a constant pressure region exists for a range of volumes, where the liquid evaporates due to the presence of impurities in the liquid (heterogeneous nucleation). The pressure starts to decrease with increasing volume only after total evaporation of the liquid. During gas compression, a reverse behavior occurs. If heterogeneous nucleation does not take place, the liquid fails to evaporate during overexpansion, resulting in a metastable liquid. Similarly, overcompression fails to induce condensation, giving a supersaturated gas. A curve that associates the metastable liquid with the supersaturated gas can be described by:

$$(\frac{\partial p}{\partial V})_T \geq 0 \tag{1.15}$$

which indicates the mechanical instability of the liquid and an irreversible phase transition to the spinoidal form (vapor and clusters), as shown in the C-D region in Figure 1.4.

1.4.2.4 Pressure pulse model

Johnson et al. [61] dealt with the pressure pulse model for desorption of organic molecules. The concept relies on the incident ion depositing kinetic energy ΔE_i in a small spherical volume of radius r_0, as a result of collisions or electronic interaction with partial conversion of the electronically deposited energy into kinetic energy. The schematic of a localized region of kinetic energy excitation is shown in (Figure 1.5).

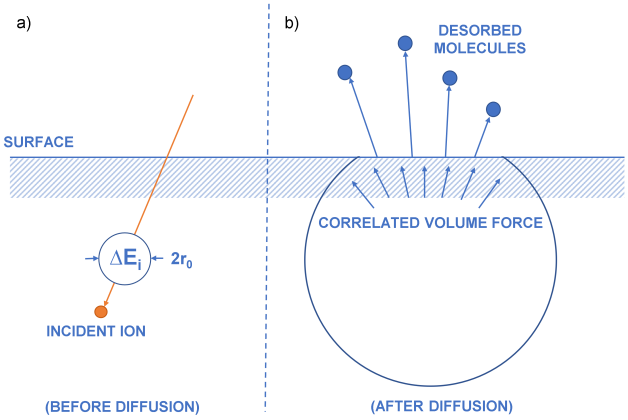

Figure 1.5: a) An incident ion creates a localized region of kinetic energy excitation, b) the motional energy diffuses collisionally. As energy reaches the surface, desorption may occur either by evaporation or in response to the correlated volume force, $\nabla\varepsilon(\mathbf{r},t)$. Acquired from [43].

The propagation of energy can be explained by a simple diffusion:

$$\nabla\cdot[\kappa\nabla\varepsilon(\mathbf{r},t)]=\frac{\partial\varepsilon(\mathbf{r},t)}{\partial t} \tag{1.16}$$

where κ is the diffusivity, and $\varepsilon(\mathbf{r},t)$ is the volume energy density. The solution is:

$$\varepsilon(\mathbf{r},t)=\frac{\Delta E_i}{\pi^{3/2}(r_0^2+4\kappa t)^{3/2}}\exp\left(-\frac{r^2}{r_0^2+4\kappa t}\right) \tag{1.17}$$

The result for a spherical geometry is the thermal spike formalism given the local temperature $T(\mathbf{r},t)$ defined as $\varepsilon(\mathbf{r},t)/kn_m$, and the desorption yield can thus be determined from Eq. 1.14.

A volume force can be introduced as -$\nabla\varepsilon(\mathbf{r},t)$, described as a net force per unit volume within the region having energy density $\varepsilon(\mathbf{r},t)$. The volume force can be seen as a pressure pulse which transfers momentum to the molecules experiencing it:

$$\mathbf{p}(\mathbf{r})=\frac{\beta}{n_m}\int_0^\infty dt[-\nabla\varepsilon(\mathbf{r},t)] \tag{1.18}$$

The proportionality constant β incorporates the translational kinetic energy fraction of the total energy in the solid (without the internal energy of molecules). In order to induce desorption, a condition on the normal molecular momentum needs to be satisfied:

$$p_\perp\geq p_c=\sqrt{2MU} \tag{1.19}$$

If one applies the pressure pulse model to cylindrical ion tracks, regarded as mini-pulses with average spacing of λ, then the surface for which the condition in Eq. 1.19 is fulfilled is a half-sphere of radius r_c. If stopping power dE/dx is associated with the quantity $\Delta E_i/\lambda$, the following scaling of half-sphere radius r_c and sputtering yield Y can be formulated:

$$r_c\propto\frac{1}{n_m^{2/3}U}\frac{dE}{dx}\;;\;\; Y\propto\left(\frac{1}{U}\frac{dE}{dx}\right)^3 \tag{1.20}$$

The angles of emission are determined by the incidence angle of impacting ion, i.e. the orientation of the cylindrical ion track with respect to the surface: ejection is estimated

at 45° when the ion impact is oriented normal to the surface, closer to the surface normal when the incidence angle is off from the normal, and around the grazing incidence, the ejection tends to happen along the surface normal.

When it comes to estimating the stopping power scaling in case of MeV atomic ions and organic targets, the pressure pulse model performs surprisingly well with its prediction $Y \propto (dE/dx)_e^3$. Additionally, it accounts for the dominant fraction of the ejected neutrals, which is consistent with measurements performed by Hedin et al. [54] for the leucine molecule. Model's predictions of ejection angular and radial velocity distributions were also corroborated by Ens et al. [55] employing molecular dynamics simulations for insulin.

Even though the pressure pulse model seems to be the most impressive in explaining the desorption of large molecules under MeV ion impact, and may even be considered the most general model proposed so far, there are still limits to the validity. For example, it is still questionable if the scaling $Y \propto (dE/dx)_e^3$ holds in general, which requires further experimental validation. Furthermore, like other models, pressure pulse model does not take into account the complex issue of ionization and neutralization, as well as possible differences in scaling laws for positive vs. negative ion yields.

1.5 MeV ToF SIMS Setup at RBI

In order to produce an ion beam for probing a sample, an ion source is required. In MeV ToF SIMS, MeV ions are used, thus one needs to accelerate the initial beam generated with an ion source to reach energies in the MeV range. In the Laboratory for Ion Beam Interactions at Ruđer Bošković Institute, several ion sources are available, as well as two electrostatic accelerators: 1.0 MV HVEE Tandetron, and 6.0 MV EN Tandem Van de Graaff (Fig. 1.6). The ion source used for generating the primary ion beam in MeV ToF

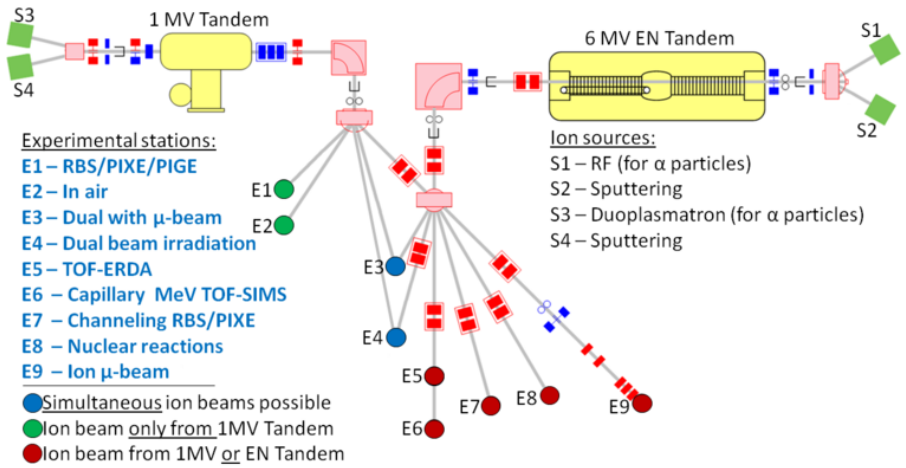

Figure 1.6: Layout of experimental beamlines at the RBI accelerator facility. Acquired from [62].

SIMS is a sputtering source called SNICS. The SNICS (Source of Negative Ions by Cesium Sputtering) can generate beams from a variety of solid materials, which are introduced into the source in the form of solid pellets and serve as cathodes. First, cesium vapor is injected from cesium oven into the system, where heated surfaces ionize the cesium vapor. Cs^+ ions are then attracted to the cooled cathode held at a small negative potential, resulting in sputtering of negative ions upon impact, which are then repelled out of the source by the cathode and pre-accelerated by a positive potential via extractor towards

the accelerator.

Both accelerators at the RBI accelerator facility are tandems, meaning they have two-step acceleration process involving one high-voltage terminal. Tandems are a variation of single-ended accelerators. The working principle of the Van de Graaff accelerator is based on accumulating electric charge on the hollow metallic terminal by means of a constantly moving insulator belt that runs between two pulleys with metallic combs (one resides inside the hollow terminal). The outer pulley is earthed and its comb is maintained at a potential difference of a few kV. A high electric field causes electrical discharge, removing electrons from the belt and making it positively charged. The belt carries the positive charge up to the inner pulley, which is inside a large ball-shaped metal terminal. The comb in the inner pulley collects positive charge from the belt and conducts it to the terminal, where it distributes evenly on the terminal surface. This way, the terminal acquires an increasing positive charge with correspondingly high voltage that rises until an equilibrium is established where the rate of loss of negative charge balances the positive charge current carried by the moving belt. The Van de Graaf accelerator can reach very high electric potentials of a few MV. The other accelerator at the RBI facility has an acceleration process very similar to the Van de Graaff accelerator. Tandetron is a type of tandem electrostatic linear accelerator that accelerates ions in a uniform electrostatic field with a maximum electric potential of +1MV supplied by a Cockroft-Walton high-voltage multiplier that consists of a combination of diodes and capacitors, instead of the belt.

The ion source in single-ended machines is usually located inside the high-voltage terminal. Tandems, on the other hand, can produce energy at least twice as high by generating the initial negative ion beam outside of the accelerator, which is then attracted toward the accelerator by the positive terminal, where a stripper gas is used to strip the negative ions of electrons, thus making it positively charged and subsequently accelerated by repulsive forces away from the terminal. This configuration offers additional advantage of much simpler ion source instrumentation accessibility outside of the accelerator.

MeV ToF SIMS setup [13] (shown in Fig. 1.7) is installed at the nuclear microprobe station (E9 in Fig. 1.6), which uses a system of quadrupole lenses (doublet or triplet) to focus an ion beam to the micrometer scale. It is convenient for sample imaging via ion beam scanning. However, the setup is limited to focusing ions with rigidity $ME/q^2 < 14$ (equivalent to 8 MeV Si^{4+}), therefore not allowing the use of heavier and more energetic ions. Other techniques are installed on the microprobe station as well, such as Particle Induced X-ray Emission (PIXE), Rutherford Backscattering Spectrometry (RBS), and Scanning Transmission Ion Microscopy (STIM).

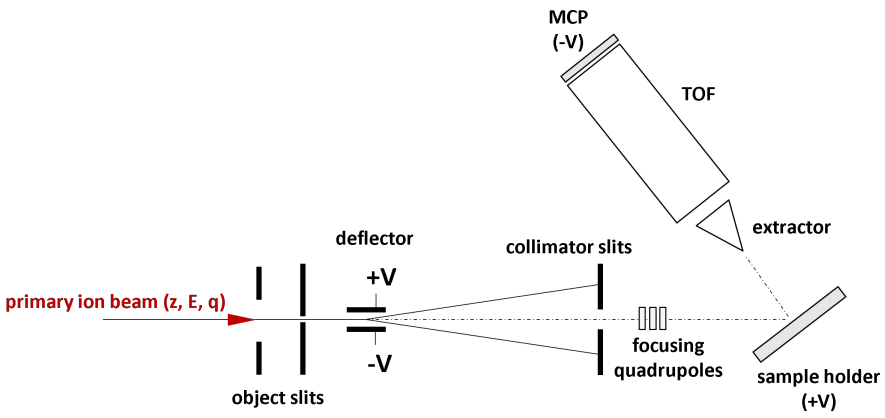

Figure 1.7: A schematic of MeV ToF SIMS setup at the RBI accelerator facility.

Ion beam current optimizing is performed using apertures such as object and collimator slits before the microprobe station. When operating MeV ToF SIMS in pulsed mode, a fast electrostatic deflector placed immediately after the object slits is used to provide ion pulses. It consists of two pairs of metal plates, each pair responsible for either horizontal or vertical deflection of the beam over the collimator slit opening. Voltage of a few hundred volts applied to the plates is enough to sufficiently deflect the type of primary ion beam used for MeV ToF SIMS. The deflector uses a fast high-voltage MOSFET push-pull switch with rise time of a few ns.

When the primary ion beam impinges on the sample surface and causes desorption of molecules, a positive or negative potential of ± 5 kV set on the sample holder repels the ejected positive or negative secondary ions toward the grounded extractor, respectively. Thus, MeV ToF SIMS can detect both positive and negative secondary ions. The extractor tip is positioned perpendicular to the sample surface, which is tilted at 45° to the incoming pulsed ion beam. In the sample surface – extraction region, secondary ions reach the same final kinetic energy [63]:

$$\frac{mv^2}{2} = eV \tag{1.21}$$

and cross the field-free drift region in the ToF tube with velocities:

$$v = (\frac{2eV}{m})^{1/2} \tag{1.22}$$

and flight times:

$$t = (\frac{m}{2eV})^{1/2} D \tag{1.23}$$

which depend upon the square root of their masses (D is the ToF tube length). This means that heavier secondary ions will reach the microchannel plate (MCP) detector at the end of the ToF tube at later times than the lighter ones, thus appearing later (at higher channels) in the mass spectrum. This is called the time-of-flight (ToF) principle. In a pulsed beam mode, beam pulsing is used as a START signal for the ToF measurement, while STOP is defined by the secondary ions reaching the MCP detector at the end of the ToF tube. In a continuous beam mode, a STIM detector can be placed behind the target to mark the START signal for the ToF measurement, but this requires a target that is transparent to the primary ion beam. The ToF spectrometer installed on the microprobe station is shown in Fig. 1.8. The recorded MeV ToF SIMS spectrum channels are proportional to time-of-flight, thus a calibration of the x-axis is necessary to represent mass usually by means of selecting well-defined peaks with known masses, using a quadratic dependence of mass on time-of-flight.

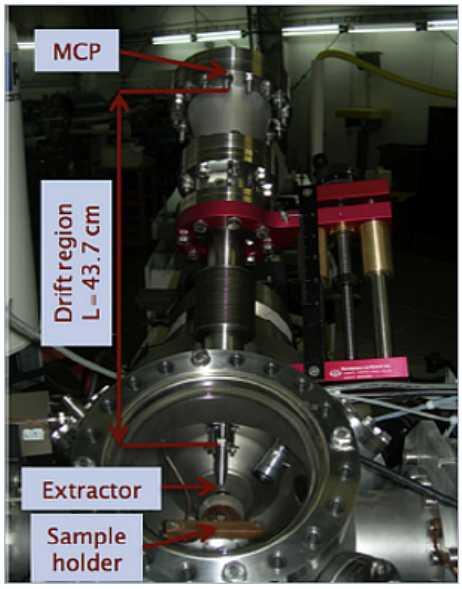

Figure 1.8: ToF SIMS spectrometer mounted on the RBI microbeam station. Acquired from [13].

1.6 Multivariate Analysis Methods

MeV ToF SIMS is a relatively new technique; thus the mass spectral databases are yet to be built. Obtained mass spectra are quite complex and high-dimensional, demanding good data interpretation and analysis tools in order to fully exploit MeV ToF SIMS capabilities. Dimensionality reduction methods such as Principal Component Analysis (PCA), commonly used for the analysis of the keV ToF SIMS mass spectra and images, can also be applied in the MeV ToF SIMS.

A single MeV SIMS mass spectrum consists of hundreds of different mass peaks and the information about sample composition, molecular orientation, surface order, chemical bonding, and sample purity is contained within this complexity. Comparing relative intensities of even a hundred peaks across a moderate group of samples significantly complicates analysis. Not only single peaks can vary across the sample set, but two or more peaks can vary with respect to each other across the samples. Considering the analysis of MeV SIMS 2D images, variations in hundreds of peak intensities across thousands of image pixels must be traced. Additionally, MeV SIMS images in general have rather small counts per pixel, and if the variations across pixels are subtle, this makes the analysis more complicated. On top of that, noisy variations due to surface topography or uneven extraction field make manual analysis even more unavailing.

Multivariate analysis (MVA) is increasingly popular among SIMS scientists for handling mentioned problems. PCA is the most often used MVA algorithm in the ToF SIMS community. To realize the full power of MVA, it is necessary to better understand what data to use to answer a given question, how to optimally process the data before applying MVA and how to correctly interpret the outcomes from the analysis. Also, good experimental design is essential to maximize the amount of quality information that MVA can leverage out of a dataset.

Prior to PCA and other multivariate analyses, the data is most often preprocessed by autoscaling or by log transformation, which can enhance the value of low intensity peaks and minimize noise contribution in the analysis. Measured data can be considered as a

set of M spectra (observations) with N measured molecular ion peaks (or a stack of N ion images having M pixels), as shown in Fig. 1.9.

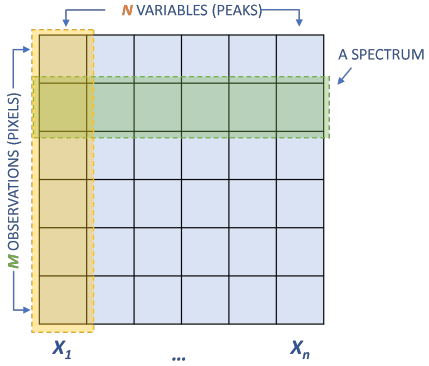

Figure 1.9: Measured data represented as a matrix X of N variables and M observations.

In SIMS, the data is collected as discreet quantised events. Such measurements follow a Poisson distribution whose variance is equal to its mean, meaning that in a distribution of intensities of a particular peak across the dataset, its mean will change depending on the intensity of that peak, and a more intense peak will have a higher mean, therefore a higher variance than weaker peaks. Hence, variables (peaks) have different amounts of noise and error, making them difficult to compare. The standard deviation of a Poisson variable is usually estimated by the square root of that variable, and the standard procedure of scaling, called *square root scaling*, is dividing each value of the original data matrix X by its square root. This happens to be inappropriate for SIMS images due to very low counts per pixel and large relative uncertainties. For this reason, Keenan and Kotula [64] proposed scaling that takes into account the relationship among all variables by dividing each column of the data matrix X (peaks) by the square root of the mean variable intensity, and then dividing each row of the matrix X (observations) by the square root of the mean spectrum:

$$X_S = G^{-1/2} X H^{-1/2} \tag{1.24}$$

where X_S is the scaled data matrix, G is a diagonal matrix with the mean variable intensity along its diagonal (the mean of each column), X is the data matrix and H is a diagonal matrix with the mean spectrum (mean of each row) along its diagonal [65].

The following two subsections are aimed to briefly cover the basic concept of PCA, a linear unsupervised dimensionality reduction technique which has been extensively used in MeV SIMS image analysis throughout the work presented in this thesis, as well as t-distributed stochastic neighbor embedding, a new and emerging non-linear dimensionality reduction technique that has proved to be particularly well suited for visualisation of high-dimensional MeV SIMS images containing subtle differences.

1.6.1 Principal component analysis

Principal component analysis (PCA) is a multivariate statistical method which is the parent of most types of factor analysis. It has been found to be particularly useful within analytical chemistry and has been successfully applied to the interpretation of many types of analytical spectra, including SIMS spectra and images. Applying PCA to a dataset as represented in Fig 1.9 produces a set of T (where $T = N$) linear combinations of the original ion peaks called principal components (PC). The first principal component (Y_1)

is given by the linear combination of the variables $X_1, X_2, \ldots, X_N$ [66]:

$$Y_1 = a_{11}X_1 + a_{12}X_2 + ...a_{1N}X_N \tag{1.25}$$

or, in matrix notation:

$$Y_1 = a_1^T X \tag{1.26}$$

The first principal component is calculated such that it accounts for the greatest possible variance in the data set. Of course, one could make the variance of Y_1 as large as possible by choosing large values for the weights $a_{11}, a_{12}, ..., a_{1N}$. To prevent this, weights are calculated with the constraint on their sum:

$$a_{11}^2 + a_{12}^2 + ... + a_{1N}^2 = 1 \tag{1.27}$$

The second principal component is calculated in the same way, with the condition that it is uncorrelated with (i.e., perpendicular to) the first principal component and that it accounts for the next highest variance:

$$Y_2 = a_{21}X_1 + a_{22}X_2 + ...a_{2N}X_N \tag{1.28}$$

A schematic of an orthogonal transformation on a system of two variables (peaks) is shown in Fig. 1.10.

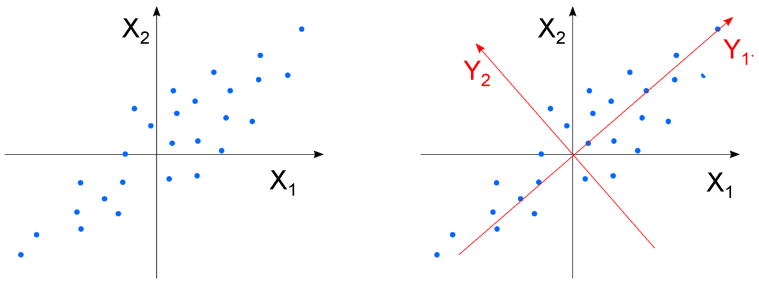

Figure 1.10: A schematic of PCA transformation on a two-variable system. The blue dots can denote pixels from SIMS image, or different samples in PCA spectra analysis.

This continues until a total of T principal components have been calculated, equal to the original number of variables N. At this point, the sum of the variances of all of the principal components will equal the sum of the variances of all of the variables, that is, all of the original information has been explained or accounted for. Collectively, all of these linear (orthogonal) transformations of the original variables to the principal components are:

$$Y = XA \tag{1.29}$$

A schematic description of Eq. 1.29 is given in Fig 1.11. The rows of matrix A are called the eigenvectors of a diagonal matrix S_X, which is the variance-covariance matrix of the original data X. The elements of an eigenvector are the weights a_{ij}, and are also known as loadings, viewed as a measure of the importance of the original axes (variables) to the new direction (principal component), shown in Fig 1.12. From matrix A and matrix S_X, the variance-covariance matrix of the principal components can be calculated:

$$S_Y = AS_XA^T \tag{1.30}$$

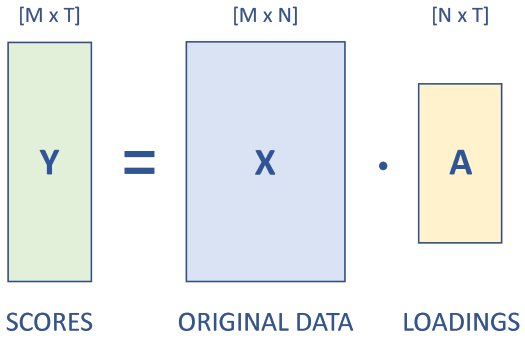

Figure 1.11: A schematic description of Eq. 1.29 depicting two key matrices, scores and loadings, generated with PCA, and their relationship with the original data. M is the number of observations (spectra), N is the number of variables (peaks), and T is the number of generated principal components.

The elements in the diagonal of matrix S_Y are known as the eigenvalues. The eigenvalues are the variance explained by each principal component and are constrained to decrease monotonically from the first to the last principal component. These eigenvalues are commonly plotted on a scree plot to show the decreasing rate at which variance is explained by additional principal components. The eigenvalues associated with the eigenvectors describe the magnitude of the eigenvector, or the spread of the observations along the new axis (Fig 1.12). The positions of each observation (or pixel) in this new coordinate system

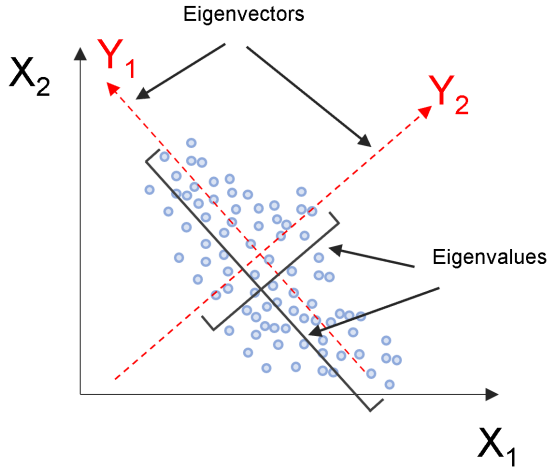

Figure 1.12: The eigenvectors define the directions of the new axes (principal components), while the eigenvalues associated with the eigenvectors describe the magnitude of the eigenvector.

of principal components are called scores (the score matrix Y in Fig 1.11) and are calculated as linear combinations of the original variables and the weights a_{ij}. For example, the score for the r^{th} sample on the k^{th} principal component is calculated as [66]:

$$Y_{rk} = a_{1k}x_{r1} + a_{2k}x_{r2} + ...a_{Nk}x_{rN} \tag{1.31}$$

In interpreting the principal components, it is often useful to know the correlations of the original variables with the principal components. The correlation of variable X_i and principal component Y_j is:

$$r_{ij} = \sqrt{a_{ij}^2 Var(Y_j)/s_{ii}} \tag{1.32}$$

In simpler words, the initial data space can be represented by orthogonal axes of variables (peaks), and by new principal components space that has orthogonal axes as well (Fig. 1.10). One is a rotation, or mapping, of the other and this means one can transform spectra back and forth between original and PC space as required.

To summarize: a loading of high magnitude for a particular peak implies that the peak is significant in defining the new direction of maximum difference in the data. A loading of smaller magnitude implies lesser importance in defining the direction. The sign of the loading does not bear importance, only the magnitude. Furthermore, if the spectral data points are projected on the new axis in PC space, then the distance along that direction is the *score* of that spectrum for that principal component. [65]

An example is given in Figure 1.13, on a dataset from *Enterococcus* spp. (*En*) and *Proteus mirabilis* (*Pm*) bacterial species, acquired from [65]. On the left, the loading plot of the first principal component is shown, together with the scores plot of PC2 against PC1. Here, it is evident that *En* samples are exhibiting similar chemistry characterized by the negatively loaded mass channels in PC1 (*m/z* 88, 132, 181), while *Pn* samples are exhibiting similar chemistry characterized by the positively loaded mass channels in PC1 (*m/z* 70, 84, 291). Mass channels exhibiting a zero or close to zero loading are considered non-discriminatory. The larger the magnitude of the loading, the more that variable contributes to the PC in question, assuming the data is properly scaled.

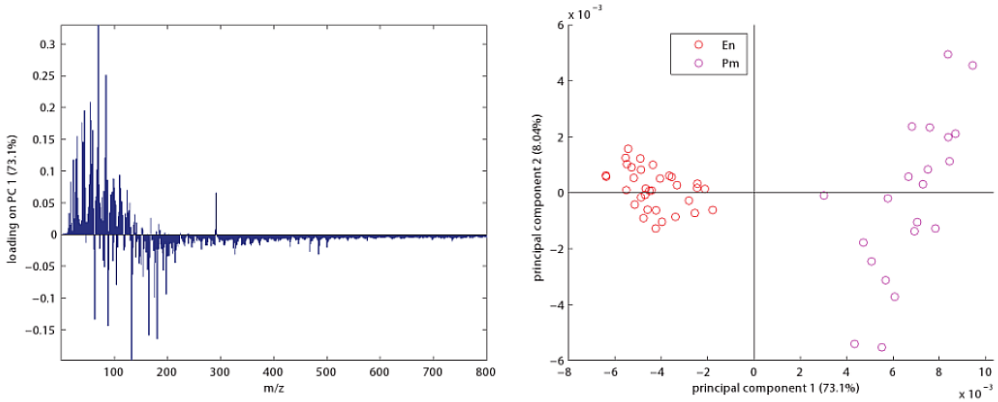

Figure 1.13: Principal components outcome of two classes of bacteria. Loading on PC1 (left) and scores of PC2 against PC1 (right) colored according to classes: *Enterococcus* spp. (*En*) red circles and *Proteus mirabilis* (*Pm*) magenta circles. Acquired from [65].

In PCA image analysis, inspection of the loadings for each PC can reveal peaks which are either strongly correlated or anti-correlated in the image and can aid in chemical interpretation of the PC images. When ion peaks load together in a principal component, this is often an indication that the peaks arise from the same chemical or physical effect. For example, if the loadings show that all of the peaks within a PC are positively correlated, that PC may capture some effect such as topography that influences the emission of all ions. A smaller number of peaks that all have large positive loadings in a PC may all be emitted from one compound that occupies the bright areas in that PC image. Peaks with large negative loadings may all be emitted from one compound that occupies the dark

areas in that PC image. Careful interpretation of the PC images and the PC loadings can assist in the image contrast enhancement, differentiation between topographic and chemical effects, and identification of series of peaks that arise from fragmentation of a molecule. [34]

Since dimensionality reduction implicits focusing on a few principal components versus many variables, several criteria have been proposed for determining how many PCs should be investigated and how many should be ignored. One common criteria is to ignore principal components at the point at which the next PC offers little increase in the total variance explained. A second criteria is to include all those PCs up to a predetermined total percent variance explained, such as 90%. A third standard is to ignore the last PCs whose variance explained is all roughly equal. [66] In spectral SIMS analysis, where noise is typically very low and the number of spectra is generally small compared to the number of pixels in an image, the magnitude of the eigenvalues is a reliable estimate of the value of the PC. Unfortunately, this is not the case for PCA analysis of ToF SIMS images with high noise content. A PC that contains a large fraction of the variance in the image may only describe noise within one of the larger image regions. A PC that describes less than 1% of total image variance may nonetheless describe a significant difference between a small region and the remaining image. [34]

1.6.2 T-distributed stochastic neighbor embedding

T-SNE is a new dimensionality reduction technique developed by van der Maaten and Hinton [67] for the visualization of similarity data that is capable of retaining local structure of the data while also somewhat preserving the important global structure. Instead simply rotating vectors as in PCA, t-SNE converts similarities between data points to joint probabilities. Local relationships between points in high dimensions are used to create a low-dimensional mapping represented by t-SNE coordinates (usually two or three). Distances between data points (observations) in a high dimensional space of variables (peaks) are used to calculate conditional probabilities with Gaussian distribution representing the similarity between data points. A similar approach is used to construct the probability distribution in a low-dimensional space using Student's t-distribution reflecting the similarities in the low-dimensional space. This results in observations that are dissimilar in a high-dimensional space being far apart in the low-dimensional t-SNE space, while similar objects in a high-dimensional space being densely packed in the t-SNE space. The algorithm tends to preserve distances (local structure of the data) by minimizing the Kullback-Leibler divergence, and it does so by using hyperparameters such as perplexity, learning rate and number of steps.

T-SNE is hence more appropriate for visualizing datasets which require numerous principal components for explaining important variations, as it is represented by only two or three t-SNE axes. It is also reported to be more sensitive to subtle variations which otherwise cannot be caught by any principal component. Additionally, due to its non-linearity, it overperforms with non-linear data compared to PCA, which assumes linearity of the dataset.

Capabilities of t-SNE in comparison to PCA are demonstrated on the MNIST images of handwritten digits, a dataset commonly used for training and testing in machine learning [68]. Data points in the space of the first two generated principal components (left) and in 2D t-SNE space (right) are shown in Figure 1.14. It is evident that PCA does not effectively separate different groups of digits by the first two principal components as much as t-SNE, which forms clusters of data points based on their relative similarities, resulting in clustering more closely to the true labels. These results also indicate that this is an example of a more non-linear than linear dataset.

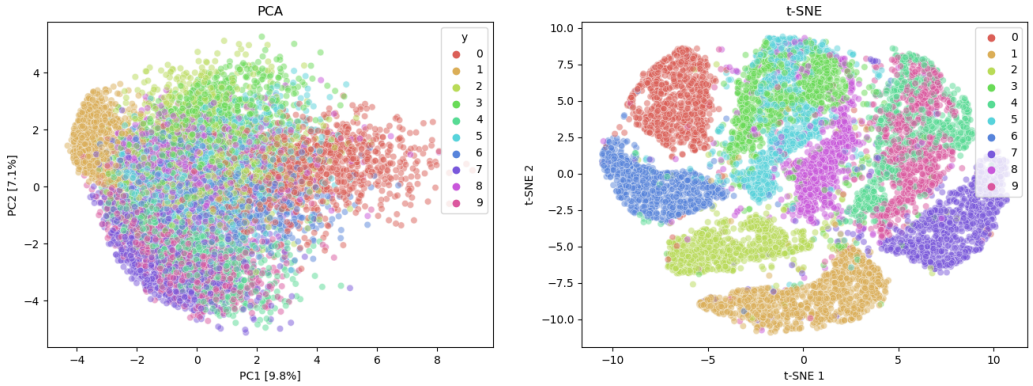

Figure 1.14: Comparison of PCA (left) and t-SNE (right) performance on the MNIST training dataset of handwritten digits.

1.6.3 MVA in the SIMS community

The first paper that dealt with PCA and SIMS in 1997 [69] proposed a method for quantification of SIMS spectra of polystyrene, with the aim to take all the information recorded in each spectra into account. In the following years, several groups demonstrated the real power of MVA in the SIMS community [70], [71] on complex biological samples such as proteins and cells. Several years later, an important breakthrough happened with the first MVA on SIMS imaging datasets of polymers [72]. The analysis of images dealt with an increased complexity, giving rise to the need for a more advanced mathematical treatment, and widened the possibilities of other methods such as multivariate curve resolution (MCR), already established in the chemometrics studies, in the application in SIMS [73], [74].

A growing number of research groups started to use MVA methods [75], [76], however the lack of standardized terminology and data pre-processing steps prior to MVA started to raise concern in the community. In order to tackle the raising problem, Lee et al. [77]–[82] and Gilmore et al. [83]–[85] published numerous comprehensive works on dealing with SIMS data specifically. Another big advancement came along with the improvement of the SIMS technique itself, becoming capable of producing very large 3D datasets (imaging with depth profiling). Around this time, subsampling of a SIMS 3D dataset with a random vectors-based algorithm was performed [86], [87], enabling the calculation of principal components using GPU. This opened up the possibility to use another MVA method called non-negative matrix factorization (NMF). The contributions continue to rise along with the size and complexity of the SIMS datasets, which are becoming inevitable in working with the most recently developed commercial SIMS instruments. Apart from the popular MVA methods within the SIMS community, the rapid growth of the machine learning research field has been inspiring SIMS researchers to apply novel and less computationally demanding analysis methods such as the application of Fourier transform analysis [88] and deep learning neural networks [89] to SIMS datasets.

1.7 Motivation and Thesis Objectives

Time-of-flight Secondary Ion Mass Spectrometry using MeV ions (MeV ToF SIMS) is a fairly new Ion Beam Analysis surface-sensitive technique being increasingly used for the analysis and imaging of organic materials in various fields, such as forensics (fingerprints and inks), cultural heritage (paints), biology (plants and tissues) etc. Conventional SIMS, on the other hand, is a well-established technique used mainly in the analysis of inorganic materials, with the most popular application in semiconductor industry. The fundamental difference between the two methods lies in the interaction mechanism of the primary ions with the material. While keV SIMS operates with energies of a few tens of keV through direct energy transfer to the secondary ions via nuclear stopping, MeV ToF SIMS uses heavy energetic ions of few tens of MeV which cause soft desorption through electronic stopping and interaction with the electronic system. This manifests in lower fragmentation of secondary ions, and higher sensitivity to large, intact molecules in MeV SIMS versus keV SIMS.

In this thesis, an idea is introduced to investigate the low energy range (a few 100 keV to a few MeV) primary ion mode in MeV SIMS and its potential benefits in exploiting the capabilities of both conventional (keV) SIMS and MeV SIMS simultaneously – the analysis of samples standardly analyzed by keV SIMS (mostly inorganic species), while still being able to sputter and analyze larger biomolecules. Systematic investigation of low energy MeV SIMS (named LE MeV SIMS in this thesis) may open up new possibilities in both the fundamental understanding of impact of the primary ion stopping power on the detection of secondary ions of organic and inorganic species, as well as in expanding the application of MeV ToF SIMS to analysis, imaging and depth profiling of inorganic species with increased efficiency. This also presents a possibility to analyze hybrid organic/inorganic compounds, increasingly popular in photovoltaics, OLED screens, solar cells etc. Furthermore, other types of instruments, such as ion implanters, could benefit in expanding their range of applications to performing mass spectrometry on organic, inorganic, or hybrid compounds within their technical limits.

In summary, the aim of this thesis is to demonstrate that MeV ToF SIMS can in fact be used to analyze inorganic, as well as hybrid organic/inorganic samples by lowering the primary ion beam energy from standardly used few MeV to a few hundred keV, and that it is capable of depth profiling of inorganic samples of several tens to hundreds nm using a relatively low-cost sputter ion source, without significant degradation of the depth profile. This is done by performing extensive systematic investigation and optimization of the MeV ToF SIMS technique in the low energy region, employing primary ion beams of different parameters and studying secondary ions yields of various inorganic and hybrid targets. These objectives are addressed in Chapter 2.

Considering MeV ToF SIMS is a relatively new technique, apart from the fundamental research in the non-standard energy region, there is still a wide range of unexplored or only touched upon applications to which the technique can contribute operating in the standard energy mode (optimized for detection of organic species). One of the most perspective fields is forensics, specifically questioned documents. MeV ToF SIMS is a surface-sensitive and chemically non-destructive technique that provides high lateral resolution information, which makes it a perspective candidate for determining the deposition order of inks from different writing tools. However, due to the complex, multivariate nature of MeV SIMS datasets, the need for multivariate analysis techniques for the detection of underlying patterns and extraction of latent information is justified in MeV SIMS imaging examples from forensics of ink intersections. In the Laboratory for Ion Beam Interactions at RBI, among numerous fields of applications of MeV SIMS the author had the chance to be involved in, the forensics of questioned documents proved to be a niche in which MeV

SIMS demonstrated the most substantial success, resulting in a formal collaboration with the accredited institution for forensic examination of the Croatian Ministry of Internal Affairs: Forensic Science Centre Ivan Vučetić. This work can bring MeV SIMS closer to qualifying as an alternative method of choice in more complex forensic cases where all standard techniques fail to either determine the deposition order or even differentiate the inks used in a system. Additionally, to the best of author's knowledge, up until now, multivariate analysis of MeV SIMS images in general has never been done before, although it has been used with other similar techniques such as cluster and keV SIMS.

To summarize, in addition to the fundamental research of the low energy region, this thesis is also aimed to demonstrate that pattern detection and extraction of crucial information from complex MeV SIMS datasets of ink intersections can be significantly enhanced with the implementation of multivariate analysis techniques as pivotal tools in determining the deposition order, especially in datasets with subtle differences and low-count peaks of interest, in which MeV SIMS outperforms optical methods. It is also aimed to signify the advantage of MeV SIMS over optical methods standardly used in questioned documents in offering rich molecular information stored in each pixel of an image with higher sensitivity to heavier molecules (mainly dyes and pigments) as opposed to keV SIMS. These objectives are addressed in Chapter 3.

Chapter 2

Optimization of MeV ToF SIMS Technique in the Low Primary Ion Beam Energy Mode for the Analysis of Inorganic Materials

In this chapter, a hypothesis is addressed that the low energy range (a few 100 keV to a few MeV) primary ion mode in MeV secondary ion mass spectrometry (LE MeV SIMS) could have potential in exploiting the capabilities of conventional (keV) SIMS and MeV SIMS simultaneously. The fundamental difference between the two methods lies in the interaction mechanism of the primary ions with the material. While keV SIMS operates with energies of a few tens of keV through direct energy transfer to the secondary ions via nuclear stopping, thus being efficient for detection of inorganic ions, MeV ToF SIMS uses heavy energetic ions of few tens of MeV which cause soft desorption through electronic stopping and interaction with the electronic system, which is more convenient for detecting ions from larger organic molecules. The low energy primary ion beam MeV SIMS mode of operation is investigated with the aim to see if in this energy range both types of materials (inorganic and organic) can be simultaneously analyzed. This study is described in Subchapter 2.1 through systematic investigation of secondary ion yields from one organic and several inorganic targets under different primary ion beam conditions, within the scope of equal influence of electronic and nuclear stopping. Furthermore, a feasibility of depth profiling of inorganic materials with LE MeV SIMS is explored in Subchapter 2.2 using a sputter-cleaning Ar ion source for etching. A comparison is made with keV SIMS depth profile acquired on the same target in order to assess possible LE MeV SIMS advantages and unique features.

Additionally, spectra of several selected inorganic samples were recorded in order to further investigate the range of targets with sufficient secondary ion yield using LE MeV SIMS. The generated set of spectra serves as a preliminary internal database and is aimed to be further continuously expanded. The data is presented in Appendix A.

2.1 MeV ToF SIMS Analysis of Hybrid Organic/Inorganic Compounds in the Low Energy Region

A systematic feasibility study was conducted, first by analyzing the dependence of secondary ion yields in indium tin oxide (ITO, In_2O_5Sn) and leucine ($C_6H_{13}NO_2$) on various primary ion energies and charge states of a Cu beam, within the scope of equal influence of electronic and nuclear stopping. The observed trend in the secondary ion yield of leucine has shown expected dominance of electronic stopping, and reduced fragmentation of leucine with higher primary ion velocities was confirmed. Secondary ions from ITO and several other selected inorganic species were successfully detected at all three chosen primary ion beam energies, exhibiting expected behavior of secondary ion yield with respect to the primary ion velocity: yields decreasing with increasing velocity, i.e., decreasing nuclear stopping in the inorganic material, which is a driving force in collisional sputtering. Furthermore, MeV SIMS images of samples containing separate regions of Cr and leucine were analyzed using both keV and MeV primary ions, in an attempt to simulate imaging of hybrid samples and compare ion image contrasts. Based on the results, it was concluded that there is potential for the imaging of hybrid organic/inorganic samples with ions in the energy range where electronic and nuclear stopping power contribute almost equally, but this largely depends on the sample characteristics, as the secondary ion yield trends are drastically different between species and there seems to be no single parameter to describe them. This complicates the choice of a unique, most optimal primary ion beam for the analysis of a hybrid target composed of multiple species.

Author's contribution: Prepared the samples and performed partial leucine evaporation on a chromium target, performed the experiments and analyses, and jointly wrote the paper with the co-authors.

ACS Partner Journal

Journal of the American Society for Mass Spectrometry

pubs.acs.org/jasms Research Article

MeV TOF SIMS Analysis of Hybrid Organic/Inorganic Compounds in the Low Energy Region

Marko Barac, Marko Brajković, Iva Bogdanović Radović, Janez Kovač, and Zdravko Siketić*

Cite This: *J. Am. Soc. Mass Spectrom.* 2021, 32, 825−831 Read Online

ACCESS | Metrics & More | Article Recommendations

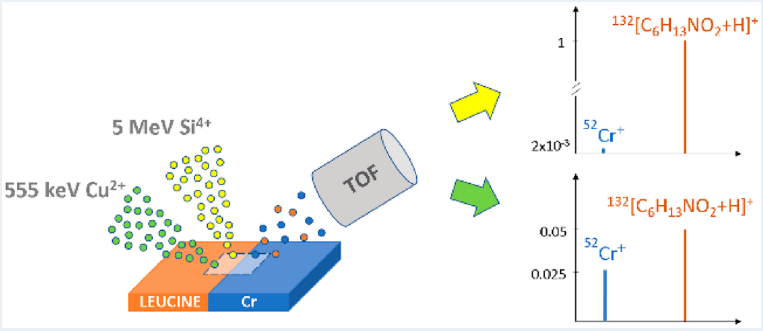

ABSTRACT: The low energy range (a few 100 keV to a few megaelectronvolts) primary ion mode in MeV secondary ion mass spectrometry (MeV SIMS) and its potential in exploiting the capabilities of conventional (keV) SIMS and MeV SIMS simultaneously were investigated. The aim is to see if in this energy range of both types of materials, inorganic and organic, can be simultaneously analyzed. A feasibility study was conducted, first by analyzing the dependence of secondary ion yields in indium tin oxide (ITO, In_2O_5Sn) and leucine ($C_6H_{13}NO_2$) on various primary ion energies and charge states of a Cu beam, within the scope of equal influence of electronic and nuclear stopping. Expected behavior was observed for both targets (mainly nuclear sputtering for ITO and electronic sputtering for leucine). MeV SIMS images of samples containing separate regions of Cr and leucine were obtained using both keV and MeV primary ions. On the basis of the image contrast and measured data, the benefit of a low energy beam is demonstrated by Cr^+ intensity leveling with leucine $[M + H]^+$ intensity, as opposed to a significant contrast at a higher energy. It is estimated that, by lowering the energy, the leucine $[M + H]^+$ yield efficiency lowers roughly 20 times as a price for gaining about 10 times larger efficiency of Cr^+ yield, while the leucine $[M + H]^+$ yield still remains sufficiently pronounced.

KEYWORDS: *low energy MeV SIMS, organic/inorganic compounds, stopping power*

INTRODUCTION

Time-of-flight secondary ion mass spectrometry (TOF SIMS) using primary beam in the megaelectronvolt energy range has emerged as a promising technique similar to cluster SIMS[1] and has been developed in the recent years in several accelerator facilities around the world. In contrast to conventional keV SIMS, higher primary ion energies generate significantly higher yields of heavy molecular ions[2] while causing softer desorption resulting in reduced fragmentation.[3]

Studies of irradiation effects focus on either displacement damage due to nuclear stopping or the effects of intense electronic excitations and ionization due to a swift heavy ion bombardment of the material. Indeed, in most situations, electronic and nuclear stopping overshadow one another. Studies that focus specifically on the stopping region where the synergy of electronic and nuclear loss is possibly the most visible are scarce. Recent research[4] on some clean metallic targets has found that, at a significant electronic loss due to swift heavy ion (SHI) bombardment, the majority of the sputtered material is emitted in the neutral state, with only a negligible fraction of ionized particles, which, however, appeared to be larger than under kiloelectronvolt bombardment. A significant electronic sputtering effect is observed in some metals but not in others. Another study[5] speculated that this could be influenced by strong electron−phonon coupling and/or a low melting point. The measured yields were not as large as for insulators but were above the predictions for solely

Received: January 11, 2021
Revised: February 4, 2021
Accepted: February 16, 2021
Published: February 22, 2021

https://dx.doi.org/10.1021/jasms.1c00006
J. Am. Soc. Mass Spectrom. 2021, 32, 825−831

Journal of the American Society for Mass Spectrometry pubs.acs.org/jasms Research Article

nuclear sputtering. Here, the synergy of nuclear and electronic loss was assumed and evaluated using an extended thermal spike model for simulating electronic sputtering by an evaporation process of particles. Experiments on the sputtering of indium atoms under the impact of slow highly charged ions indicated a fundamentally different sputtering mechanism as compared to nuclear sputtering observed under a conventional kiloelectronvolt primary ion beam.[6] In our most recent study concerning the detection of large organic molecules,[7] an expected increase of the secondary ion yield of phthalocyanine with increasing energy, charge state, electronic stopping, and velocity was found for several different types of primary ions. Although the general trend is valid, there seemed to be no single parameter able to describe the results for all primary ions at once.

In the present study, an idea is introduced to investigate the low energy range (a few 100 keV to a few megaelectronvolts) primary ion mode in MeV SIMS and its potential benefits in exploiting the capabilities of both conventional (keV) SIMS and MeV SIMS simultaneously—the analysis of samples standardly analyzed by keV SIMS (mostly inorganic species), while still being able to sputter and analyze larger biomolecules. Low energy MeV SIMS may open up a possibility for this fairly new accelerator technique, as well as for other types of instruments, such as ion implanters, to perform mass spectrometry on hybrid organic/inorganic compounds within their technical limits.

METHODS

All measurements were performed using an 1 MV HVE Tandetron accelerator on the heavy-ion microprobe line at Ruđer Bošković Institute, where the TOF SIMS system was installed.[8] This kind of system is flexible to some degree in terms of primary ion species, energy, and charge state, which is a key advantage in performing these studies. Specifically, the system is limited to a maximal magnetic rigidity equivalent to an 8 MeV Si^{4+} beam. Measurements were carried out under a vacuum (10^{-6}–10^{-7} hPa). The time-of-flight start signal was defined by a pulsed primary ion beam, achieved with the beam deflector located about 6 m in front of the sample, and the stop signal was defined by a secondary ion reaching the microchannel plate (MCP) detector positioned at the end of the linear TOF spectrometer. The voltage applied to the sample holder in order to push the secondary ions into the TOF system was +5 kV, and the MCP detector voltage was set to −2 kV; therefore, the instrument was operated in the positive ion mode. The primary ion beam was focused using magnetic quadrupole lenses. All the measured secondary ion yields were normalized to the total current that impacted the sample during the measurement. This was done in a way that, before and after each measurement, first, the direct current was measured in a Faraday cup. Second, the time for which the beam was present on a sample was calculated from the beam deflector geometry, the high voltage switch rise time (10 ns), and the voltage applied to deflect the beam (from 100 to 500 V), in order to calculate the duty cycle and thus the effective current that affected the sample. To minimize the effects of sample surface conditions and geometry on the measured secondary molecular yields, spectra were collected from the same sample area. For each measurement, the target angle with respect to the extractor was optimized to maximize the total secondary ion yield. Currents measured on a Faraday cup ranged from 0.9–900 pA depending on the primary ion species and energy. The beam fluence during all the measurements was kept below the static limit for SIMS[9] (which is around 10^{12} ions/cm^2), so the variation in secondary ion yields due to surface damage can be neglected. Normalized secondary ion yield uncertainties include Faraday cup measured current uncertainties of about 10% and uncertainties of peak areas (defined by the square root of counts from the linearly fitted background and the square root of counts from net peak area). It should be noted that, because of the variations in mass resolution and in the background trends for each energy point, as well as a lack of statistics in certain cases, the uncertainty was sometimes considerable.

In the first part of the study, indium tin oxide (ITO, In_2O_5Sn) and leucine ($C_6H_{13}NO_2$) were analyzed using Cu primary ions of seven different energies and charge states, keeping the magnetic rigidity $(m{\cdot}E)/q^2$ constant for technical simplicity, except for the lowest two energies. The indium ion yield from a 120 nm thick conductive layer of ITO coated on a glass plate and leucine molecular yields from leucine evaporated on a silicon plate were analyzed.

In the second part, various inorganic species were selected and analyzed using three different primary ion beam energies after Ar^+ sputter-cleaning of their surfaces.

In the last part of the study, a two-component sample was made in a way that leucine was evaporated partly on Cr, and then, imaging was performed at the region where both leucine and the inorganic part of the sample were present. Measurements were done by employing 555 keV Cu^{2+} and 5 MeV Si^{4+} primary ions, with currents ranging from 12–20 and 200–500 pA, respectively. The scan size was around 400 × 400 μm^2, with a beam diameter of roughly 50 μm. Furthermore, average spectra of the organic and inorganic regions were generated. For each primary ion beam, the average pixel spectra were obtained from two clusters generated by k-means clustering algorithm applied on selected principal components after principal component analysis (PCA).

RESULTS AND DISCUSSION

Secondary Ion Yield Dependence of In^+ in ITO and Main Molecular Ion in Leucine on Various Primary Ion Velocities in the Low Energy MeV SIMS Region. In order to investigate the possibility to detect organic molecular ions at low energies and inorganic ions at high energies, as well as to observe general trends in secondary ion yields with respect to the stopping power, ITO and leucine were analyzed using Cu primary ions having seven different energies and charge states. Te primary ion beams used were 150 keV Cu^{2+}, 300 keV Cu^{2+}, 555 keV Cu^{2+}, 1.25 MeV Cu^{3+}, 2.22 MeV Cu^{4+}, 3.47 MeV Cu^{5+}, and 5 MeV Cu^{6+}. Leucine was additionally analyzed using 5 MeV Si^{4+}. The energy/charge state region covered with these beams encompasses the stopping power region in which an equal occurrence of nuclear and electronic stopping interactions is expected in each sample. The electronic stopping power was calculated with CasP program[10] (using the UCA model and DHFS screening potential) since it provides nonequilibrium energy loss and considers the charge state of the incident ion. This is crucial in the context of SIMS in which the sputtering occurs from the first few monolayers at the sample surface, where the ion charge state equilibrium is not yet established. The nuclear stopping power was calculated using SRIM.[11]

https://dx.doi.org/10.1021/jasms.1c00006
J. Am. Soc. Mass Spectrom. 2021, 32, 825−831

Journal of the American Society for Mass Spectrometry pubs.acs.org/jasms Research Article

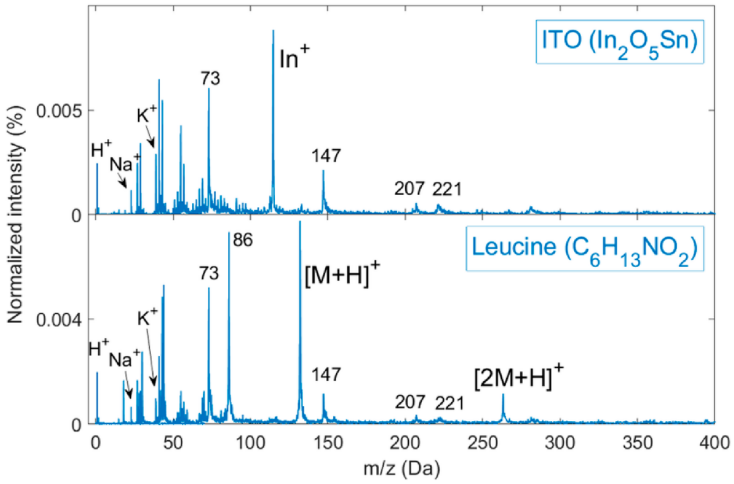

Figure 1. MeV SIMS spectra of ITO and leucine obtained with 1.25 MeV Cu^{3+} primary ions.

Typical MeV SIMS spectra of ITO and leucine obtained with 1.25 MeV Cu^{3+} primary ions are presented in Figure 1. Spectra were normalized to the total number of counts.

Both spectra contain H^+, Na^+, and K^+ ions, as well as polydimethylsiloxane (PDMS), which is a usually present contaminant at the sample surface. PDMS characteristic positive ions can be seen at m/z = 73, 147, 207 and 221 Da, and are often used to calibrate the mass spectra. ITO yields an In^+ ion at m/z = 114.8 Da, which appears to be prominent at this energy. Leucine yields its protonated main molecular ion peaks $[M + H]^+$ with m/z = 132 Da and $[2M + H]^+$ with m/z = 263 Da.

Figure 2 shows In^+ secondary ion yield dependence on the primary ion velocity, with respect to the ratio of nuclear and

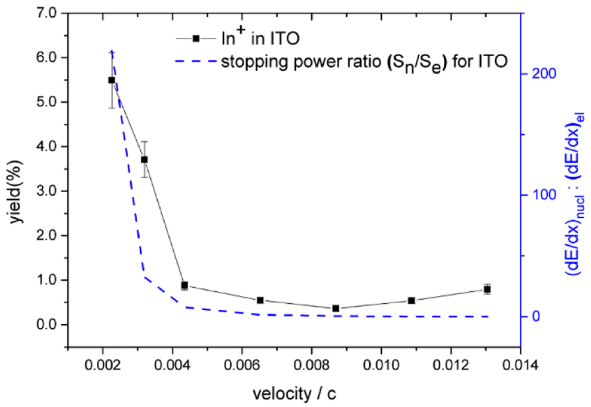

Figure 2. In^+ secondary ion yield dependence on primary ion velocity with respect to the ratio of nuclear and electronic stopping in ITO.

electronic stopping in ITO. The lines in the figure are intended to guide the eye. Clearly, In^+ ions mainly sputter as a consequence of nuclear loss of primary ion energy in the material, since the yield rapidly decreases according to the decrease of the nuclear to electronic stopping ratio in ITO. However, the yield starts to slightly increase after around v/c = 0.009 (2.22 MeV Cu^{4+}), which indicates the influence of electronic loss on the sputtering of In^+, as well.

Figure 3 shows a leucine protonated main molecular ion yield $[M + H]^+$ with m/z = 132 Da and a leucine m/z = 86 Da fragment molecular ion yield dependence on primary ion velocity with respect to the ratio of electronic and nuclear stopping in leucine. As an organic compound, leucine is expected to sputter more efficiently on higher energies and charge states. It is clear that the yields of the main molecule and fragment increase in accordance with the electronic loss in leucine. Also, the yield of fragment m/z = 86 Da increases more slowly than the main molecular ion yield $[M + H]^+$, which is also expected since it is known that the fragmentation of organic compounds is reduced with increasing electronic loss in the material. This effect is more obvious in Figure 4, where the yield ratio $Y_{86}/Y_{[M+H]^+}$ can be seen decreasing with increasing velocity of the primary ions.

Secondary Ion Yield Dependence of Selected Inorganic Species on Primary Ion Velocity. Samples including V, Co, Cr, In, ITO, and Sn were all sputter-cleaned before the analysis with 200 keV Cu^{2+}, 440 keV Cu^{2+}, and 5 MeV Si^{4+} primary ions. Sputter-cleaning was performed for 15 min with a PREVAC Ion Source IS 40C1 operating under E = 3 keV and I = 10 mA, with an Ar pressure of about 6×10^{-6} mbar and a current density around 15 $\mu A/cm^2$, which corresponds to an Ar^+ ion fluence of about 8×10^{16} ions/cm^2. Secondary ion yields were measured at all three energies and plotted for each sample with respect to the primary ion velocity (Figure 5).

Clearly, all secondary ions exhibit sputtering behavior influenced mainly by nuclear stopping (which is more pronounced at lower velocities). This is expected for metals because of the considerable dissipation of electronic excitation before any significant energy transfer to the lattice occurs.

Imaging of Cr with Partially Evaporated Leucine with 555 keV Cu^{2+} and 5 MeV Si^{4+}. In order to investigate the possibility of performing MeV SIMS imaging on a sample consisting of laterally distributed partly organic and partly inorganic regions and efficiently detect all relevant constituents simultaneously, a target was produced by evaporating leucine powder on a part of Cr foil. Then, imaging was performed at the region where both leucine and the Cr area of the sample is present, with 555 keV Cu^+ and 5 MeV Si^{4+} primary ions. It should be noted that the measured area is not precisely the

https://dx.doi.org/10.1021/jasms.1c00006
J. Am. Soc. Mass Spectrom. 2021, 32, 825−831

Journal of the American Society for Mass Spectrometry pubs.acs.org/jasms Research Article

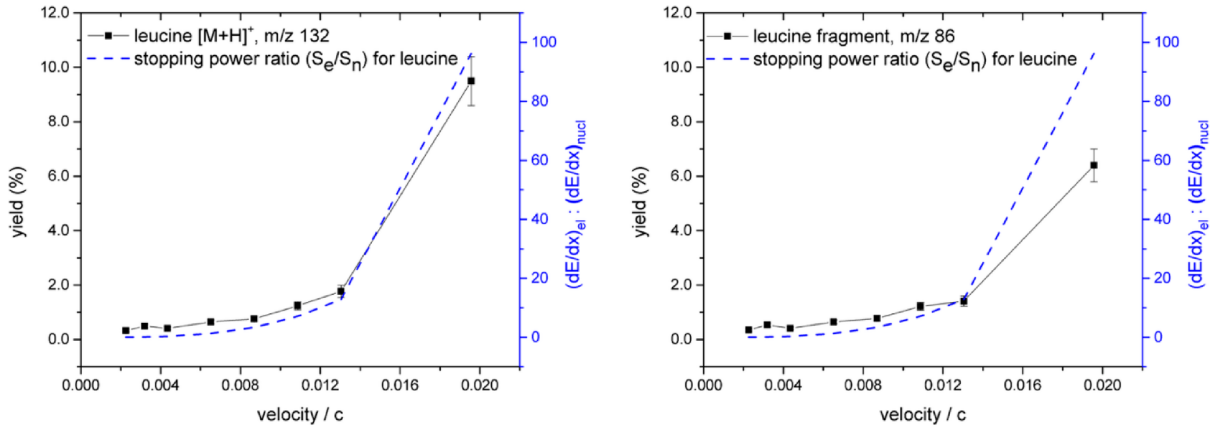

Figure 3. Leucine m/z = 132 Da (left) and leucine fragment m/z = 86 Da (right) molecular ion yields dependence on primary ion velocity with respect to the ratio of electronic and nuclear stopping in leucine.

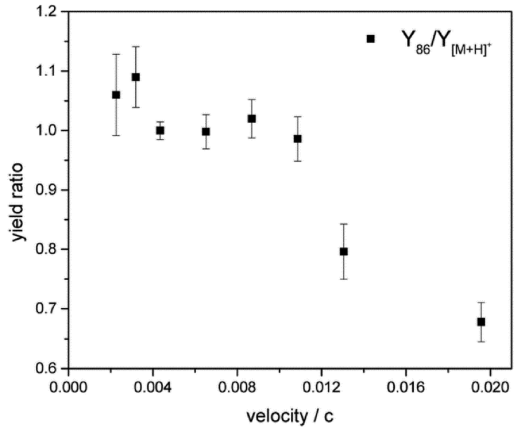

Figure 4. Dependence of yield ratio of leucine fragment m/z = 86 Da and main molecular ion m/z = 132 Da on primary ion velocity.

same for 555 keV and 5 MeV primary ions because of the need for beam optimization using a Faraday cup after the beam was changed. The images were generated by selecting peaks corresponding to Cr^+ and leucine $[M + H]^+$ from the total mass spectrum. Binning by a factor of 2 was applied, resulting in 64 × 64 pixels, and smoothing with a Gaussian filter (standard deviation of 0.6) in order to flatten random intensity variations across the species-specific region. For each primary ion beam energy, the Cr^+ color intensity was normalized to the total leucine $[M + H]^+$ yield for comparison. The intensity comparison should be made only between images of different species obtained with the same primary beam energy, since the data was not normalized to the effective current but only to the total number of counts.

On the basis of the earlier obtained graphs, one can expect a roughly 20 times higher secondary ion yield of leucine $[M + H]^+$ with 5 MeV Si^{4+} compared to that of the 555 keV Cu^{2+} primary beam. In contrast, Cr^+ is expected to be roughly 10

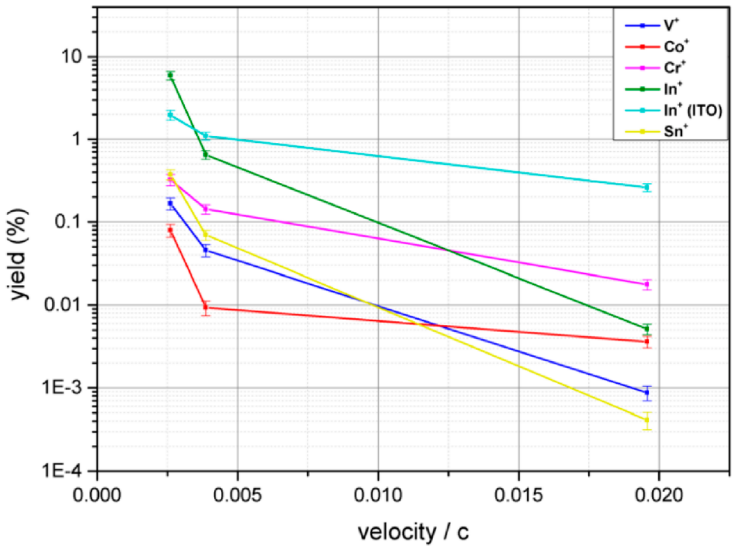

Figure 5. Secondary ion yield dependence of various inorganic ions on primary ion velocity corresponding to 200 keV Cu^{2+}, 440 keV Cu^{2+}, and 5 MeV Si^{4+}, respectively.

https://dx.doi.org/10.1021/jasms.1c00006
J. Am. Soc. Mass Spectrom. 2021, 32, 825−831

Journal of the American Society for Mass Spectrometry pubs.acs.org/jasms Research Article

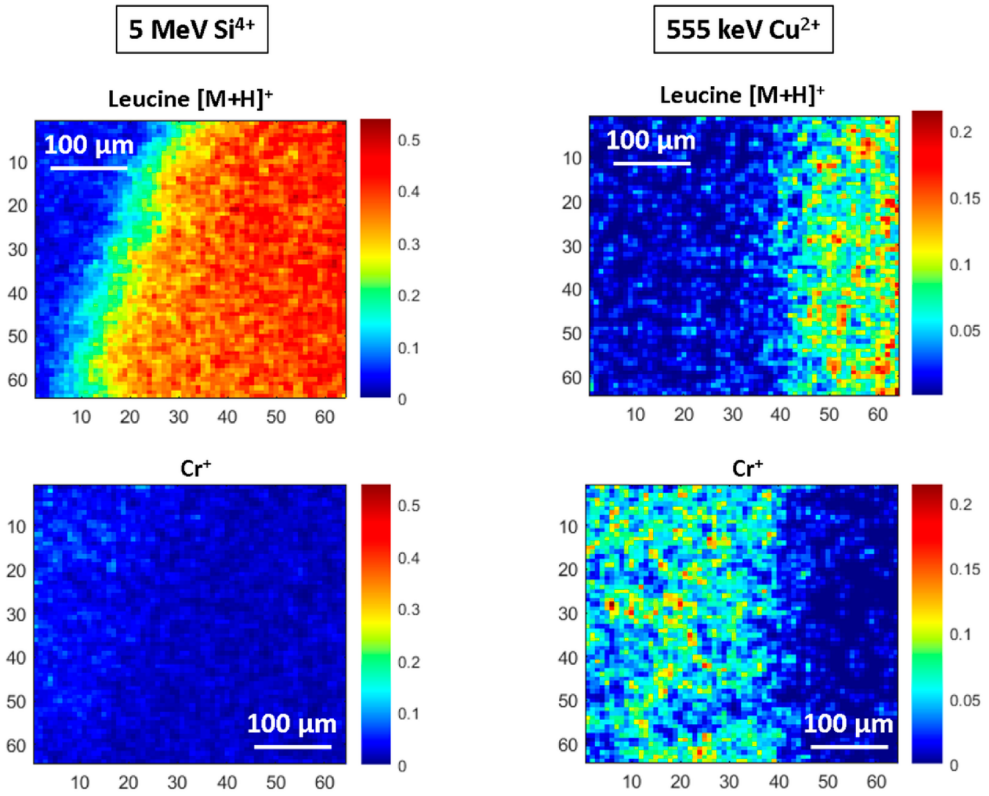

Figure 6. (left) 5 MeV Si^{4+} images of leucine and Cr regions. (right) 555 keV Cu^{2+} images of leucine and Cr regions. In each case, the Cr^+ color intensity was normalized to the total leucine $[M + H]^+$ yield.

times higher with 555 keV Cu^{2+} versus 5 MeV Si^{4+}. On the contrary, the leucine $[M + H]^+$ yield is expected to be around 500 times higher than the Cr^+ yield on 5 MeV Si^{4+} and only about twice as high as Cr^+ on 555 keV Cu^{2+}, which is demonstrated in Figure 6. The contrast between leucine $[M + H]^+$ and Cr^+ becomes almost completely diminished by lowering the energy to 555 keV Cu^{2+}. In other words, the leucine $[M + H]^+$ yield efficiency lowered as a price for gaining a larger efficiency of Cr^+ yield, although still remained pronounced at 555 keV Cu^+.

The effect can also be observed by comparing the spectra of species-particular regions averaged over pixels (Figure 7). Prior to k-means, PCA was applied to the preprocessed data as described in the beginning of this subsection, but the cluster spectra were generated from binned and normalized original image, without smoothing. The Cr^+ peak can be observed from the Cr region at 5 MeV Si^{4+} in Figure 7a, which is higher than estimated with respect to the leucine $[M + H]^+$ peak from the leucine region, but this could be due to the not well-defined interface between the two regions as a result of the beam spot dimension. In Figure 7b, for 555 keV Cu^{2+}, the yields of Cr^+ and leucine $[M + H]^+$ become more comparable, with the Cr^+ peak showing up.

CONCLUSIONS

In the present study, the expected behavior of the secondary ion yield of In^+ in ITO and the main molecular ion $[M + H]^+$ from leucine was observed with regard to the nuclear and electronic energy loss in the material, respectively. It was found that, in the stopping region covered with the used primary ion beams, a synergy of electronic and nuclear loss could occur, but this depends mainly on the sample characteristics. Nevertheless, the observed trends in the secondary ion yields mostly show the dominance of either nuclear (ITO) or electronic (leucine) stopping yet with indications of electronic stopping influence on the In^+ yield in ITO at higher velocities. Also, the molecular ion yield of the leucine fragment at m/z = 86 Da expressed the anticipated behavior—the yield increases with the electronic stopping, while the ratio of the fragment ion and the main molecular ion yield decreases, indicating that the fragmentation is reduced for higher primary ion velocities.

Selected inorganic species were successfully detected at all three primary ion beam energies, exhibiting expected behavior of secondary ion yield with respect to the primary ion velocity—yields decreasing with increasing velocity, i.e., decreasing nuclear stopping in the inorganic material, which is a driving force in collisional sputtering.

MeV SIMS images were obtained using 555 keV Cu^{2+} and 5 MeV Si^{4+} primary ions on a hybrid sample consisting of regions containing Cr and leucine, laterally separated. It is anticipated that, by lowering the energy to 555 keV Cu^{2+}, the leucine $[M + H]^+$ yield efficiency is reduced roughly 20 times as a price for gaining about 10 times higher efficiency of Cr^+ yield while still remaining prominent at a low energy. On the basis of the results from this study, it can be concluded that there is a potential for the imaging of hybrid organic/inorganic samples with ions in the energy range where electronic and nuclear stopping power contribute almost equally.

https://dx.doi.org/10.1021/jasms.1c00006
J. Am. Soc. Mass Spectrom. 2021, 32, 825−831

Journal of the American Society for Mass Spectrometry pubs.acs.org/jasms Research Article

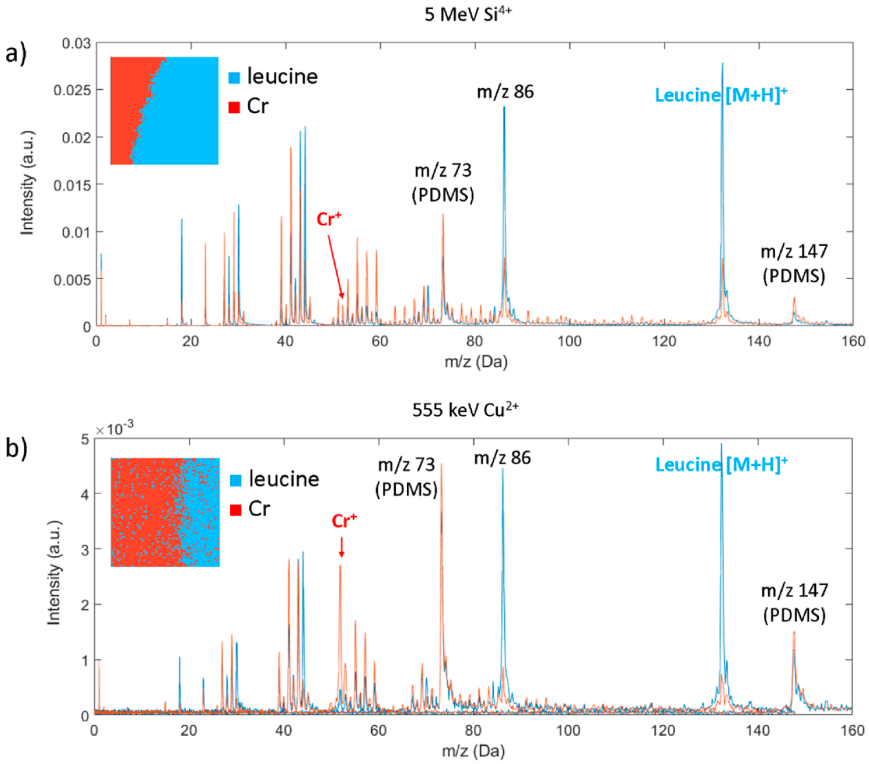

Figure 7. Average cluster spectra of the leucine area (blue) and Cr area (red) from the MeV SIMS image obtained with (a) 5 MeV Si^{4+} and (b) 555 keV Cu^{2+}.

AUTHOR INFORMATION

Corresponding Author

Zdravko Siketić – *Ruđer Bošković Institute, HR-10000 Zagreb, Croatia;* orcid.org/0000-0002-7358-8090; Phone: +38514571227; Email: zsiketic@irb.hr

Authors

Marko Barac – *Ruđer Bošković Institute, HR-10000 Zagreb, Croatia; Jožef Stefan International Postgraduate School, SLO-1000 Ljubljana, Slovenia*

Marko Brajković – *Ruđer Bošković Institute, HR-10000 Zagreb, Croatia*

Iva Bogdanović Radović – *Ruđer Bošković Institute, HR-10000 Zagreb, Croatia;* orcid.org/0000-0002-4100-736X

Janez Kovač – *Jožef Stefan Institute, SLO-1000 Ljubljana, Slovenia*

Complete contact information is available at: https://pubs.acs.org/10.1021/jasms.1c00006

Notes

The authors declare no competing financial interest.

ACKNOWLEDGMENTS

Authors acknowledge support by the RADIATE project under the Grant Agreement 824096 from the EU Research and Innovation program HORIZON 2020 and by the European Regional Development Fund for the 'Center of Excellence for Advanced Materials and Sensing Devices' (Grant No. KK.01.1.1.01.0001). M. Brajković acknowledges support by the Croatian Science Foundation (CSF) project "Young Researchers' Career Development Project - Training of Doctoral Students" co-financed by the European Union, Operational Program "Efficient Human Resources 2014-2020" and the ESF.

REFERENCES

(1) Jones, B. N.; Matsuo, J.; Nakata, Y.; Yamada, H.; Watts, J.; Hinder, S.; Palitsin, V.; Webb, R. Comparison of MeV monomer ion and keV cluster ToF-SIMS. *Surf. Interface Anal.* **2011**, *43* (1–2), 249–252.

(2) Nakata, Y.; Honda, Y.; Ninomiya, S.; Seki, T.; Aoki, T.; Matsuo, J. Yield enhancement of molecular ions with MeV ion-induced electronic excitation. *Appl. Surf. Sci.* **2008**, *255* (4), 1591–1594.

(3) Kamensky, I.; Håkansson, P.; Sundqvist, B.; McNeal, C. J.; Macfarlane, R. Comparison of biomolecule desorption yields for low and high energy primary ions. *Nucl. Instrum. Methods Phys. Res.* **1982**, *198* (1), 65–68.

(4) Breuer, L.; Ernst, P.; Herder, M.; Meinerzhagen, F.; Bender, M.; Severin, D.; Wucher, A. Mass spectrometric investigation of material sputtered under swift heavy ion bombardment. *Nucl. Instrum. Methods Phys. Res., Sect. B* **2018**, *435*, 101–110.

(5) Mieskes, H. D.; Assmann, W.; Grüner, F.; Kucal, H.; Wang, Z. G.; Toulemonde, M. Electronic and nuclear thermal spike effects in sputtering of metals with energetic heavy ions. *Phys. Rev. B* **2003**, *67* (15), 155414.

(6) Herder, M.; Ernst, P.; Skopinski, L.; Weidtmann, B.; Schleberger, M.; Wucher, A. Ionization probability of sputtered indium atoms under impact of slow highly charged ions. *J. Vac. Sci. Technol., B: Nanotechnol. Microelectron.: Mater., Process., Meas., Phenom.* **2020**, *38* (4), 044003.

(7) Brajković, M.; Barac, M.; Bogdanović Radović, I.; Siketić, Z. Dependence of Megaelectron Volt Time-of-Flight Secondary Ion

Journal of the American Society for Mass Spectrometry pubs.acs.org/jasms Research Article

Mass Spectrometry Secondary Molecular Ion Yield from Phthalocyanine Blue on Primary Ion Stopping Power. *J. Am. Soc. Mass Spectrom.* **2020**, *31* (7), 1518−1524.
(8) Tadić, T.; Bogdanović Radović, I.; Siketić, Z.; Cosic, D. D.; Skukan, N.; Jakšić, M.; Matsuo, J. Development of a TOF SIMS setup at the Zagreb heavy ion microbeam facility. *Nucl. Instrum. Methods Phys. Res., Sect. B* **2014**, *332*, 234−237.
(9) Amstalden van Hove, E. R.; Smith, D. F.; Heeren, R. M. A. A concise review of mass spectrometry imaging. *Journal of Chromatography A* **2010**, *1217* (25), 3946−3954.
(10) Grande, P. L.; Schiwietz, G. The unitary convolution approximation for heavy ions. *Nucl. Instrum. Methods Phys. Res., Sect. B* **2002**, *195* (1−2), 55−63.
(11) Ziegler, J. F.; Ziegler, M. D.; Biersack, J. P. SRIM - The stopping and range of ions in matter (2010). *Nucl. Instrum. Methods Phys. Res., Sect. B* **2010**, *268* (11−12), 1818−1823.

https://dx.doi.org/10.1021/jasms.1c00006
J. Am. Soc. Mass Spectrom. 2021, 32, 825−831

2.2 Depth Profiling of Cr-ITO Dual-Layer Sample with MeV SIMS Using Ions in the Low Energy Region

In this subchapter, a possibility of depth profiling of inorganic materials with LE MeV SIMS is explored using 555 keV Cu^{2+} primary ion beam, while etching the surface with 1 keV Ar^{+} ions. This is demonstrated on a dual-layer sample consisting of 50 nm Cr layer deposited on 150 nm ITO glass. These materials proved to have sufficient secondary ion yield on this particular primary ion beam energy in the previous study. LE MeV SIMS and keV SIMS depth profiles of Cr-ITO dual-layer are compared and corroborated by AFM and ToF-ERDA analysis. The profile demonstrated solid chemical sensitivity to inorganic secondary ions, as expected, as well as satisfactory depth resolution comparable to keV SIMS using the same type of etching beam. The observed limitations in the profile seemed to be a consequence of the sputtering rather then the analysis conditions. Perhaps the most interesting revelation was a significantly reduced matrix effect on Cr^{+} secondary ion at the partially oxidized locations in Cr layer, compared to keV SIMS. This work demonstrates that depth profiling of inorganic materials with MeV SIMS using lower energy primary ion beams is feasible using a relatively low-cost sputtering source for etching.

Author's contribution: Optimized the experimental setup for depth profiling, performed LE MeV SIMS measurements and analysis, and jointly wrote the paper with the co-authors.

www.nature.com/scientificreports

scientific reports

Check for updates

OPEN

Depth profiling of Cr-ITO dual-layer sample with secondary ion mass spectrometry using MeV ions in the low energy region

Marko Barac[1,2]✉, Marko Brajković[1], Zdravko Siketić[1], Jernej Ekar[2,3], Iva Bogdanović Radović[1], Iva Šrut Rakić[4] & Janez Kovač[3]

This work explores the possibility of depth profiling of inorganic materials with Megaelectron Volt Secondary Ion Mass Spectrometry using low energy primary ions (LE MeV SIMS), specifically 555 keV Cu^{2+}, while etching the surface with 1 keV Ar^{+} ions. This is demonstrated on a dual-layer sample consisting of 50 nm Cr layer deposited on 150 nm In_2O_5Sn (ITO) glass. These materials proved to have sufficient secondary ion yield in previous studies using copper ions with energies of several hundred keV. LE MeV SIMS and keV SIMS depth profiles of Cr-ITO dual-layer are compared and corroborated by atomic force microscopy (AFM) and time-of-flight elastic recoil detection analysis (TOF-ERDA). The results show the potential of LE MeV SIMS depth profiling of inorganic multilayer systems in accelerator facilities equipped with MeV SIMS setup and a fairly simple sputtering source.

Secondary Ion Mass Spectrometry using MeV ions (MeV SIMS)[1] is a fairly new Ion Beam Analysis (IBA) technique that is being increasingly used for the analysis and imaging of organic materials in various fields, such as forensics (fingerprints[2] and inks[3–5]), cultural heritage (paints[6]), biology (plants[7] and tissues[8]), etc. Conventional keV SIMS, on the other hand, is a well-established technique used mainly in the analysis and depth profiling of inorganic materials, with the most popular application in the semiconductor industry, i.e. studies of dopant profiles[9,10], diffusion, corrosion[11], contamination[12], etc. It is also convenient for analyzing biomolecules, but with decreased ionization efficiency compared to MeV SIMS[1] and keV cluster SIMS[13,14]. Techniques developed in order to enhance the ionization efficiency involve the use of high energy gas cluster ion beams (GCIBs) such as C_{60}^{+} and Ar_x ($x = 500–5000$)[13,14] and recently water cluster ions $(H_2O)_n^{+}$ ($n = 1–10\,000$)[15,16], which have proven superior over former.

KeV SIMS is a surface-sensitive technique (ions are detected from a few uppermost monolayers) and can be extended to depth profile analysis by introducing ion sputtering. A variety of applications in SIMS depth profiling arise from high sensitivity to inorganic species and excellent depth resolution[17,18]. Recently, depth profiling of organic films has proven promising by employing either cluster ion beams or low energy Cs^{+} ions for sputtering, due to reduced surface degradation[19]. Depth resolution, a quantitative measure of the depth range, is by convention the sputtered depth measured between 84 and 16% of the maximum yield at an ideally sharp interface between two media[20]. Several different parameters contribute to the profile broadening that originate from instrumental factors, ion beam-sample interactions, and sample characteristics. These include surface roughening caused by sputtering[21], atomic mixing in the collision cascade[22], information depth of the technique[23], non-uniform etching ion beam density in the analyzed area[24], differential sputtering due to crystalline/amorphous regions[25], etc. For thicker metallic layers, sputtering-induced roughness is generally the dominating contribution to depth resolution[26]. The best resolution in SIMS (below 5 nm) is achieved with low sputtering ion beam energy[27] (below 1 keV) and high incidence angle, in combination with sample rotation in order to minimize sputtering-induced roughness[28]. At this point, atomic mixing and information depth are of increasing importance for depth resolution[26].

On the other hand, modification of the original element distribution due to matrix effects poses a significant limitation in quantitative SIMS depth profiling. This phenomenon arises from the secondary ion yield dependence on the surrounding chemical state (of the matrix). The matrix effect depends largely on experimental

[1]Ruđer Bošković Institute, Bijenička c. 54, 10000 Zagreb, Croatia. [2]Jožef Stefan International Postgraduate School, Jamova c. 39, SLO-1000 Ljubljana, Slovenia. [3]Jožef Stefan Institute, Jamova c. 39, SLO-1000 Ljubljana, Slovenia. [4]Institute of Physics, Bijenička c. 46, 10000 Zagreb, Croatia. ✉email: mbarac@irb.hr

conditions, namely the nature of the primary ion, the incident angle, the detected species, and the energy of secondary ions[29]. In data analysis, this is usually tackled with the use of reference materials containing similar matrix[10,30,31]. Many studies have investigated the parameters involved in matrix effects and possible methods for reducing them[32,33].

MeV SIMS is also surface-sensitive and can in theory be extended to depth profiling. The fundamental difference between keV and MeV SIMS lies in the interaction mechanism of the primary ions with the material. While keV SIMS operates with energies of a few tens of keV through direct energy transfer to the secondary ions via nuclear stopping, MeV SIMS uses heavy energetic ions of a few tens of MeV that interact through electronic stopping with the target's electronic system. It was shown in our previous work[34] that lowering the primary ion beam energy from a standardly used few MeV to a few hundred keV enhances the efficiency of secondary ion detection for some inorganic species. Their detection was successful at all three primary ion beam energies used (200 keV Cu^{2+}, 440 keV Cu^{2+}, and standardly used 5 MeV Si^{4+}), exhibiting the expected behavior of secondary ion yield with respect to the primary ion velocity: their yields decreasing with increasing velocity, i.e., decreasing nuclear stopping in the inorganic material, which is a driving force in collisional sputtering. This energy mode was named LE (Low Energy) MeV SIMS. In the present work, LE MeV SIMS depth profiling was explored based on previously confirmed good sensitivity to several inorganic species, in order to compare the achieved depth resolution against keV SIMS, as well as to observe the magnitude of eventual matrix effects, given that specific primary ion beam conditions are introduced in LE MeV SIMS. Up until now, the authors have found no record of an attempt of a dual-beam MeV SIMS depth profiling of inorganic matter in the literature.

This first demonstration of MeV SIMS depth profiling of an inorganic target at low primary ion beam energy opens up possibilities in both fundamental understanding of the impact of the primary ion characteristics on secondary ion yield of inorganic species, as well as expanding the application of MeV SIMS and other types of instruments, such as ion implanters, to perform mass spectrometry of inorganic species within their technical limits. This also presents a novelty for Ion Beam Analysis (IBA) laboratories in terms of the possibility to expand (and possibly improve) the set of existing techniques capable of depth profiling.

Experimental and methods

A dual-layer Cr-ITO sample was prepared by magnetron sputtering of roughly 50 nm Cr on top of 150 nm ITO (In_2O_5Sn), deposited on a soda-lime glass substrate. The sample was first characterized by Time-of-Flight Elastic Recoil Detection Analysis (TOF-ERDA) to determine layers' atomic content and layer thicknesses. TOF-ERDA measurement was performed by 23 MeV $^{127}I^{7+}$ ions with 20° incidence angle toward the sample surface. TOF-ERDA spectrometer was positioned at an angle of 37.5° toward the beam direction. More details about the used TOF-ERDA spectrometer can be found in the Ref.[35,36].

The sample was also examined by atomic force microscopy (AFM) in tapping mode at several different places over areas of 2×2 μm^2 to 10×10 μm^2 before and after sputtering, in order to obtain RMS roughness.

KeV TOF SIMS depth profiling was performed on the dual-layer Cr-ITO sample on a TOF.SIMS 5 instrument produced by ION TOF, Germany, at Jožef Stefan Institute in Ljubljana, Slovenia, in a dual-beam mode using 30 keV Bi^+ analysis ion beam with ion current of 2 pA and 1 keV Ar^+ etching ion beam with ion current of 127 nA. The analysis was performed over an area of 100×100 μm^2, while etching was done over 400×400 μm^2. The base pressure in the chamber was $5{\cdot}10^{-9}$ mbar. Hydrogen was introduced in the analysis chamber at pressure $7{\cdot}10^{-7}$ mbar to reduce matrix effects[32]. Mass spectra were obtained in the positive secondary ion mode.

LE MeV SIMS depth profiling was performed on the dual-layer Cr-ITO sample on an in-house MeV TOF SIMS setup described elsewhere[37]. The chosen analysis beam was 555 keV Cu^{2+}, having currents in the range of 1–5 fA in pulsed primary ion mode. The analysis covered an area of 300×300 μm^2, under vacuum pressure of 10^{-6}–10^{-7} mbar. Sputtering was carried out using PREVAC Ion Source IS 40C1, operating with 1 keV Ar^+ ion beam and emission current of 10 mA. The ion source was mounted at an angle of 45° with respect to the surface normal. The sputtering beam spot size was approximately 1×1 cm^2, as provided by the manufacturer. During ion sputtering, the sample holder was scanned in two directions in an attempt to homogenize sputtering, thus creating a sputtering area in the shape of a parallelogram with an unspecified area. Ar pressure was ranging from $6{\cdot}10^{-5}$ to $3{\cdot}10^{-4}$ mbar and the unsuppressed ion current measured on the target was ranging from 6 to 12 μA (changed between cycles). Depth profiling was conducted in a dual-beam mode, in cycles consisting of SIMS analysis of the sample surface by 555 keV Cu^{2+} and sputtering by 1 keV Ar^+ for 10–20 min. Mass spectra were obtained in a positive secondary ion mode. While generating depth profiles, peak areas of selected secondary ions were normalized to the primary ion current and measurement time.

Results and discussion

Dual-layer Cr-ITO sample was first evaluated with TOF-ERDA depth profiling. The resulting depth profile of the main species constituting the sample is shown in Fig. 1. Analysis of TOF-ERDA spectra was performed by software Potku[38]. Despite the fact that depth resolution in ERDA deteriorates with depth due to multiple scattering, one can obtain the thickness of each layer by integrating the depth profile, or directly by measuring the distance between half of the maximum of the elemental curve at the layer surface (which marks the beginning of the layer) and at the interface (which marks the end of the layer). Cr and ITO layer thickness is calculated to be 44 ± 3 nm and 154 ± 9 nm, respectively (atomic density of Cr and ITO was considered in conversion from atoms/cm^2 to nm). It should be noted that because of deteriorating depth resolution (which is roughly 22 nm at the Cr-ITO interface), ERDA has limited capability to resolve eventual structure in the depth profile at the layers' interface. Since ERDA is a quantitative technique, elemental concentrations are provided in atomic percentages.

KeV SIMS profiles of selected species with respect to the sputter ion dose density (ions/cm^2) are shown in Fig. 2. Cr-ITO interface is clearly resolved, and layers' compositions are mostly uniform. Another ToF SIMS

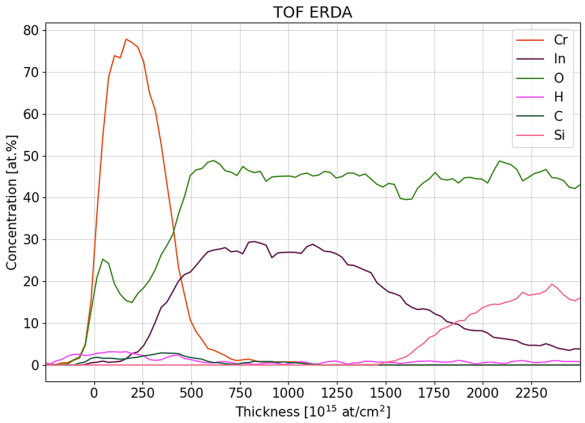

Figure 1. TOF ERDA depth profile of dual-layer Cr-ITO sample on soda-lime glass.

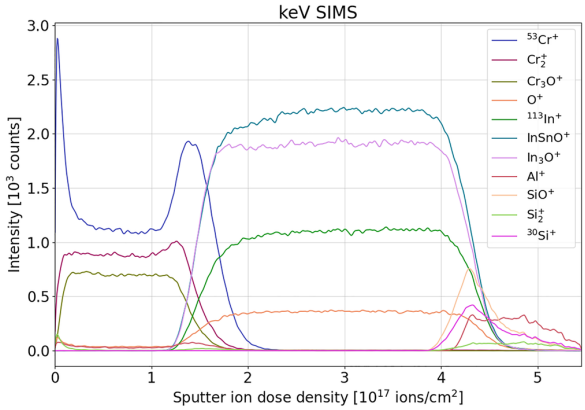

Figure 2. keV SIMS depth profile of selected species from dual-layer Cr-ITO sample on soda-lime glass.

measurement (not shown here) using a 2 keV Cs^+ etching beam observed the presence of increased CrO^- at the surface of the Cr layer and interface with ITO. As a result, partial oxidation of Cr at the Cr-ITO interface causes a matrix effect by enhancing secondary ion yield of Cr^+, as shown in Fig. 2. Many other oxides were detected as well, but with much lower efficiency.

LE MeV SIMS profiles of detected secondary ions from inorganic species are shown in Fig. 3. The x-axis is expressed in "quasi-dose" (cumulative sputtering ion current x sputtering time, per sputter cycle) since the sputter ion dose density could not be calculated due to the inability to precisely define the sputtering area. The main constituents of both layers and substrate (Cr^+, In^+, Sn^+, Si^+) are detected as positive ions, together with their isotopes with expected abundancies. In the case of Cr and In, the depth profile represents the sum of normalized peak areas of secondary ions of all detected isotopes. The profiles demonstrate significant chemical sensitivity to inorganic secondary ions. No oxides were detected in both positive and negative secondary ion mode, possibly due to lower efficiency to eject oxides with 555 keV Cu^{2+} primary ion beam, and/or due to the presence of a higher amount of background in the mass spectra while operating in the low energy mode. Also, there is generally a significantly lower total secondary ion yield in negative than in positive secondary ion mode. No cluster secondary ions were detected in positive secondary ion mode.

The satisfactory quality of LE MeV SIMS depth profile is reflected in the depth resolution at the Cr-ITO interface that is comparable to that in keV SIMS: the estimated difference in depth between 16 and 84% of the plateau is roughly 10 nm and 11 nm, for keV SIMS (Cr_2^+) and LE MeV SIMS (Cr^+), respectively. This estimation was done by directly converting the x-axes to thickness (in nm) according to ERDA profiles. However, at the end of the dual-layer, the depth resolution in LE MeV SIMS worsens compared to keV SIMS, presumably due to Ar ion gun sputtering conditions during LE MeV SIMS analyses, which could potentially be improved. Another significant observation in LE MeV SIMS depth profile is the reduced matrix effect on Cr^+ secondary ion yield at the Cr-ITO interface where keV SIMS indicated the presence of oxidized Cr. There is no sharp increase in secondary ion yield at the surface and at the end of the Cr layer as it is observed in the keV SIMS analyses for the Cr^+ signal, instead the profile is rather steady. However, it is known that monoatomic metallic ions are more

www.nature.com/scientificreports/

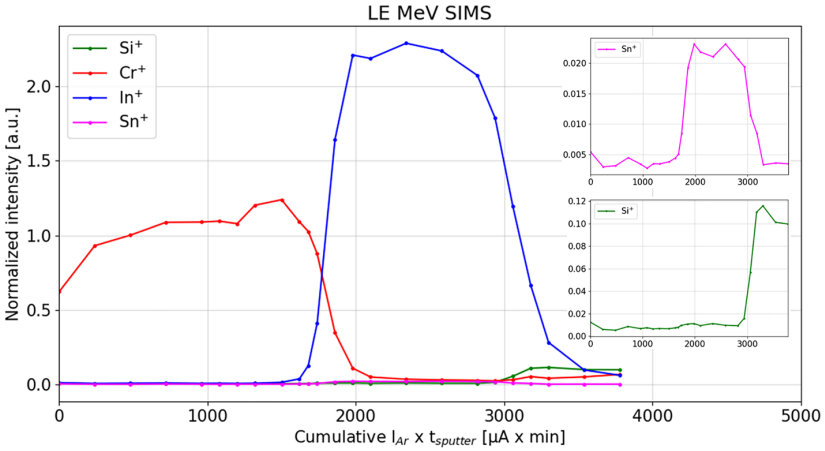

Figure 3. LE MeV SIMS depth profile of detected positive secondary ions from inorganic species from dual-layer Cr-ITO sample on a soda-lime glass. Low intensity ions are presented inside the plot: Sn^+ (top) and Si^+ (bottom).

prone to matrix effect than cluster ions, hence, in keV SIMS, such layers are usually displayed through metallic dimers or trimers.

AFM of the pre-sputtered sample was performed in several segments. For virgin surface (Cr), an average RMS of 3.6 ± 0.2 nm was obtained. Virgin ITO surface before deposition of Cr layer revealed an average RMS of 3.8 ± 0.1 nm. Because the glass plate came with an already deposited ITO layer, the roughness of the virgin substrate (soda-lime glass) was measured from the substrate backside with an average RMS of 4.6 ± 0.5 nm. In the case of LE MEV SIMS, the crater in the post-sputtered sample revealed an average RMS of 8.1 ± 2.4 nm, whereas for keV SIMS, an average RMS of 9.1 ± 0.4 nm was obtained for the crater. The depth resolution degradation at the end of the ITO layer in LE MeV SIMS compared to keV SIMS is obviously not a consequence of roughness since the crater RMS is comparable to that of keV SIMS. However, it could be attributable to inhomogeneous Ar^+ sputtering-induced non-horizontal crater bottom since Ar^+ beam was not focused as in keV SIMS, and the analysis beam covered a fairly large area of 300 × 300 µm^2.

Another difference between keV and LE MeV SIMS profiles concerns the ratio of the widths of Cr and ITO layer profiles. The width of each profile depends on the sputter yield of that element, given the energy and species of the etching ion beam (atoms/ion). Since profiles from both techniques were generated with the same type of etching beam (1 keV Ar^+), one would expect a linear dependence between their x-axes. However, the vacuum conditions during sputtering were notably different ($7{\cdot}10^{-7}$ mbar for keV SIMS, and $6{\cdot}10^{-5}$–$3{\cdot}10^{-4}$ mbar for LE MeV SIMS). There is evidence in the literature that the sputtering yield may be affected by background pressure[39]. Other than that, the authors have found no other explanation for this discrepancy.

Conclusions

Obtained LE MeV SIMS depth profiles of a dual-layer Cr-ITO sample demonstrate significant chemical sensitivity to inorganic secondary ions, as well as satisfactory depth resolution comparable to that of keV SIMS performed on the same type of sample using the same type of etching beam (1 keV Ar^+). However, at the end of the dual-layer, depth resolution in LE MeV SIMS worsens compared to keV SIMS, but this is probably due to Ar sputtering conditions, which could potentially be improved by focusing the beam and defining a more uniform beam rastering. A notable revelation was a sign of majorly reduced matrix effect on Cr + secondary ion at the partially oxidized locations in Cr layer (surface and interface with ITO), compared to keV SIMS. This phenomenon is worth further exploring systematically.

One should note that LE MeV SIMS depth profiling is not as straightforward as on the commercial keV SIMS instruments, providing a significantly fewer number of points per sputter cycle, which can be time-consuming. All things considered, all of the observed limitations in LE MeV SIMS profiles seem to be a consequence of the sputtering rather than the analysis conditions. Overall, this work shows the benefit for other IBA laboratories that possess MeV SIMS instrument in expanding its application to inorganic samples by lowering the energy of the primary ion beam, thus gaining multiple orders of magnitude higher efficiencies of inorganic ions and obtaining depth profiles of intermediate-thickness samples with satisfactory depth resolution. Moreover, this can be realized using a relatively low-cost sputtering source.

In theory, this also paves the way for MeV SIMS depth profiling of hybrid organic/inorganic samples such as OLED screens or hybrid solar cells, at least in terms of the ability to detect secondary ions of both organic and inorganic species simultaneously in the low energy mode.

Received: 18 March 2022; Accepted: 4 July 2022
Published online: 08 July 2022

References

1. Nakata, Y. *et al.* Matrix-free high-resolution imaging mass spectrometry with high-energy ion projectiles. *J. Mass Spectrom.* **44**, 128–136 (2009).
2. Bailey, M. J. *et al.* Depth profiling of fingerprint and ink signals by SIMS and MeV SIMS. *Nucl. Instrum. Methods Phys. Res., Sect. B* **268**, 1929–1932 (2010).
3. Moore, K. L. *et al.* Determination of deposition order of toners, inkjet inks, and blue ballpoint pen combining Mev-secondary ion mass spectrometry and particle induced x-ray emission. *Anal. Chem.* **91**, 12997–13005 (2019).
4. Malloy, M. C., Bogdanović Radović, I., Siketić, Z. & Jakšić, M. Determination of deposition order of blue ballpoint pen lines by MeV secondary ion mass spectrometry. *Forensic Chem.* **7**, 75–80 (2018).
5. Barac, M. *et al.* Comparison of optical techniques and MeV SIMS in determining deposition order between optically distinguishable and indistinguishable inks from different writing tools. *Forensic Sci. Int.* **331**, 111136 (2022).
6. Radović, I. B. *et al.* Identification and imaging of modern paints using secondary ion mass spectrometry with MeV ions. *Nucl. Instrum. Methods Phys. Res., Sect. B* **406**, 296–301 (2017).
7. Jenčič, B. *et al.* Molecular imaging of cannabis leaf tissue with MeV-SIMS method. *Nucl. Instrum. Methods Phys. Res., Sect. B* **371**, 205–210 (2016).
8. Jenčič, B. *et al.* MeV-SIMS TOF imaging of organic tissue with continuous primary beam. *J. Am. Soc. Mass Spectrom.* **30**, 1801–1812 (2019).
9. Wei, X., Zhao, L., Wang, J., Zeng, Y. & Li, J. Characterization of nitride-based LED materials and devices using TOF-SIMS: Characterization of LED materials and devices using TOF-SIMS. *Surf. Interface Anal.* **46**, 299–302 (2014).
10. Gong, B. & Marjo, C. E. Quantitative ToF-SIMS depth profiling of a multi-phased III-V semiconductor matrix via the analysis of secondary cluster ions: Quantitative TOF-SIMS depth profiling of III-V matrix. *Surf. Interface Anal.* **48**, 422–427 (2016).
11. Wang, L. *et al.* Study of the surface oxides and corrosion behavior of an equiatomic CoCrFeMnNi high entropy alloy by XPS and ToF-SIMS. *Corros. Sci.* **167**, 108507 (2020).
12. Mowat, I., Lindley, P. & McCaig, L. A correlation of TOF-SIMS and TXRF for the analysis of trace metal contamination on silicon and gallium arsenide. *Appl. Surf. Sci.* **203–204**, 495–499 (2003).
13. Rabbani, S., Barber, A. M., Fletcher, J. S., Lockyer, N. P. & Vickerman, J. C. TOF-SIMS with argon gas cluster ion beams: A comparison with C_{60}^+. *Anal. Chem.* **83**, 3793–3800 (2011).
14. Angerer, T. B., Blenkinsopp, P. & Fletcher, J. S. High energy gas cluster ions for organic and biological analysis by time-of-flight secondary ion mass spectrometry. *Int. J. Mass Spectrom.* **377**, 591–598 (2015).
15. Sheraz née Rabbani, S. *et al.* Prospect of increasing secondary ion yields in ToF-SIMS using water cluster primary ion beams: Examining new primary ion sources for ToF-SIMS. *Surf. Interface Anal.* **46**, 51–53 (2014).
16. Sheraz née Rabbani, S., Barber, A., Fletcher, J. S., Lockyer, N. P. & Vickerman, J. C. Enhancing secondary ion yields in time of flight-secondary ion mass spectrometry using water cluster primary beams. *Anal. Chem.* **85**, 5654–5658 (2013).
17. Baryshev, S. V. *et al.* High-resolution secondary ion mass spectrometry depth profiling of nanolayers: Depth profiling of nanolayers by high-resolution SIMS. *Rapid Commun. Mass Spectrom.* **26**, 2224–2230 (2012).
18. Chakraborty, P. Ultra-high depth resolution SIMS for the interface analysis of complex low-dimensional structures. *Nucl. Instrum. Methods Phys. Res., Sect. B* **266**, 1858–1865 (2008).
19. Mouhib, T. *et al.* Molecular depth profiling of organic photovoltaic heterojunction layers by ToF-SIMS: comparative evaluation of three sputtering beams. *Analyst* **138**, 6801 (2013).
20. ASTM. Standard Terminology Relating to Surface Analysis. *American Society for Testing and Materials, Committee E-42 on Surface Analysis*, 4 (1992).
21. Yan, X. L., Duvenhage, M. M., Wang, J. Y., Swart, H. C. & Terblans, J. J. Evaluation of sputtering induced surface roughness development of Ni/Cu multilayers thin films by Time-of-Flight Secondary Ion Mass Spectrometry depth profiling with different energies O2+ ion bombardment. *Thin Solid Films* **669**, 188–197 (2019).
22. Andersen, H. H. The depth resolution of sputter profiling. *Appl. Phys.* **18**, 131–140 (1979).
23. Hofmann, S. & Schubert, J. Determination and application of the depth resolution function in sputter profiling with secondary ion mass spectroscopy and Auger electron spectroscopy. *J. Vac. Sci. Technol., A: Vac., Surf. Films* **16**, 1096–1102 (1998).
24. Magee, C. W. & Honig, R. E. Depth profiling by SIMS?depth resolution, dynamic range and sensitivity. *Surf. Interface Anal.* **4**, 35–41 (1982).
25. Graham, D. J., Wagner, M. S. & Castner, D. G. Information from complexity: Challenges of TOF-SIMS data interpretation. *Appl. Surf. Sci.* **252**, 6860–6868 (2006).
26. Satori, K., Haga, Y., Minatoya, R., Aoki, M. & Kajiwara, K. Factors causing deterioration of depth resolution in Auger electron spectroscopy depth profiling of multilayered systems. *J. Vac. Sci. Technol., A: Vac., Surf. Films* **15**, 478–484 (1997).
27. Hofmann, S. Compositional depth profiling by sputtering. *Prog. Surf. Sci.* **36**, 35–87 (1991).
28. Zalar, A. Improved depth resolution by sample rotation during Auger electron spectroscopy depth profiling. *Thin Solid Films* **124**, 223–230 (1985).
29. Saha, B. & Chakraborty, P. MCs_n^+-SIMS: An innovative approach for direct compositional analysis of materials without standards. *Energy Procedia* **41**, 80–109 (2013).
30. Wilson, R. G. & Novak, S. W. Systematics of secondary-ion-mass spectrometry relative sensitivity factors versus electron affinity and ionization potential for a variety of matrices determined from implanted standards of more than 70 elements. *J. Appl. Phys.* **69**, 466–474 (1991).
31. Zanderigo, F., Ferrari, S., Queirolo, G., Pello, C. & Borgini, M. Quantitative TOF-SIMS analysis of metal contamination on silicon wafers. *Mater. Sci. Eng., B* **73**, 173–177 (2000).
32. Ekar, J., Panjan, P., Drev, S. & Kovač, J. ToF-SIMS depth profiling of metal, metal oxide, and alloy multilayers in atmospheres of H_2, C_2H_2, CO, and O_2. *J. Am. Soc. Mass Spectrom.* **33**, 31–44 (2022).
33. Priebe, A., Xie, T., Bürki, G., Pethö, L. & Michler, J. The matrix effect in TOF-SIMS analysis of two-element inorganic thin films. *J. Anal. At. Spectrom.* **35**, 1156–1166 (2020).
34. Barac, M., Brajković, M., Bogdanović Radović, I., Kovač, J. & Siketić, Z. MeV TOF SIMS analysis of hybrid organic/inorganic compounds in the low energy region. *J. Am. Soc. Mass Spectrom.* **32**, 825–831 (2021).
35. Siketić, Z., Radović, I. B. & Jakšić, M. Development of a time-of-flight spectrometer at the Ruder Bošković Institute in Zagreb. *Nucl. Instrum. Methods Phys. Res., Sect. B* **266**, 1328–1332 (2008).
36. Siketić, Z., Radović, I. B. & Jakšić, M. Quantitative analysis of hydrogen in thin films using time-of-flight elastic recoil detection analysis. *Thin Solid Films* **518**, 2617–2622 (2010).
37. Tadić, T. *et al.* Development of a TOF SIMS setup at the Zagreb heavy ion microbeam facility. *Nucl. Instrum. Methods Phys. Res., Sect. B* **332**, 234–237 (2014).
38. Arstila, K. *et al.* Potku – New analysis software for heavy ion elastic recoil detection analysis. *Nucl. Instrum. Methods Phys. Res., Sect. B* **331**, 34–41 (2014).
39. Husinsky, W., Betz, G., Girgis, I., Viehböck, F. & Bay, H. L. Velocity distributions and sputtering yields of chromium atoms under argon, oxygen and carbon ion bombardment. *J. Nucl. Mater.* **128–129**, 577–582 (1984).

Acknowledgements
Authors acknowledge support by the RADIATE project under the Grant Agreement 824096 from the EU Research and Innovation program HORIZON 2020 and by the European Regional Development Fund for the 'Center of Excellence for Advanced Materials and Sensing Devices' (Grant No. KK.01.1.1.01.0001), Ruđer Bošković Institute, Zagreb, Croatia. M. Brajković acknowledges support by the Croatian Science Foundation (CSF) project "Young Researchers' Career Development Project—Training of Doctoral Students" co-financed by the European Union, Operational Program "Efficient Human Resources 2014-2020".

Author contributions
M.B. planned and optimized the experimental setup and performed LE MeV SIMS measurements together with Z.S. and M.B. M.B. prepared the manuscript text, as well as interpreted the results together with Z.S., J.K., and I.B.R. KeV SIMS depth profile measurements performed by J.E. and J.K. TOF-ERDA measurements and analysis performed by Z.S. AFM measurements performed by I.Š.R. All authors reviewed the manuscript.

Competing interests
The authors declare no competing interests.

Additional information
Correspondence and requests for materials should be addressed to M.B.

Reprints and permissions information is available at www.nature.com/reprints.

Publisher's note Springer Nature remains neutral with regard to jurisdictional claims in published maps and institutional affiliations.

Chapter 3

Application of MeV ToF SIMS in the Standard Primary Ion Beam Energy Mode in Forensics of Questioned Documents, Supported by MVA Image Analysis

This chapter explores MeV ToF SIMS application in forensics of questioned documents, specifically imaging of intersecting lines made by inks from various types of writing tools using a standard MeV primary ion beam, with the aim of determining their deposition order. The most recognized techniques for looking at intersecting lines of any kind in forensic daily work are optical methods, which have the benefit of being affordable and entirely non-destructive, but they often struggle when the intersecting lines have similar colors or yield similar infra-red luminescence. Additionally, there is an element of interpretation, meaning the conclusion can vary between forensic examiners. Also, optical methods do not provide any information on chemical composition of used inks. This is where MeV SIMS is advantageous, offering rich molecular information on analyzed inks with higher sensitivity to heavier molecules (mainly dyes and pigments) as opposed to keV SIMS. Furthermore, MeV SIMS is a surface-sensitive technique, which makes it a perfect candidate for inspection of ink intersections. In Subchapter 3.1, a feasibility study is conducted using MeV SIMS with the aim to determine the deposition order of inks from various types of writing tools. Principal component analysis was employed in image processing, which proved to greatly enhance the contrast between different ink traces. Since MeV SIMS is an IBA technique with the potential of analyzing the sample with multiple different IBA methods, PIXE was conducted on cases that were left unsolved by MeV SIMS, because it provides information about elemental composition through characteristic X-ray spectra coming from greater depth, assuming it would yield additional information about the problematic intersections. Subchapter 3.2 deals with a more focused study, involving only the most often used writing tools in real forensic cases. Intersections were studied using optical techniques that are standardly applied for questioned documents, and MeV SIMS. The aim of this study was to compare the performance of optical techniques and MeV SIMS for several combinations of intersecting lines. MeV SIMS images were processed with PCA, except in cases with optically identical inks, where t-Stochastic Neighbor Embedding (t-SNE) was attempted instead, assuming better performance due to its non-linear nature and sensitivity to subtle variations in the dataset.

3.1 Determination of Deposition Order of Toners, Inkjet Inks, and Blue Ballpoint Pens Combining MeV SIMS and PIXE

A novel application of MeV SIMS coupled with particle-induced X-ray emission (PIXE) is presented in Subchapter 3.1 for determining the deposition order of intersecting lines made by a ballpoint pen ink, inkjet printer inks, and laser printer toners. In contrast to MeV SIMS, PIXE provides information about elemental composition through characteristic X-ray spectra coming from greater depth, under an assumption that both inks yield unique characteristic X-rays and that they are prominent enough to penetrate the ink above. Principal component analysis is employed for image processing of the data from both MeV SIMS and PIXE. MeV SIMS alone was sufficient to successfully determine the deposition order in 4 out of 6 cases. Cases that were not solved with MeV SIMS all involved inkjet ink, which proved to be challenging when it was on top. Thus, these were further analyzed by PIXE, which contributed to better understanding of the behavior of inkjet ink at the intersection and helped resolve the issue in most cases. Based on the fact that inkjet ink is mainly composed of water and tends to penetrate deep into the paper, and any remaining ink on the surface evaporates, the combination of both MeV SIMS and PIXE led to a conclusion that the presence of the other ink between the inkjet ink and the paper was preventing inkjet ink from adhering and penetrating into the paper entirely. It was concluded that MeV SIMS alone, therefore, generally has more success in determining the deposition order of oil-based inks, such as ballpoint pens, since they both penetrate into the paper and form a membrane on top, which is a necessary condition for a surface-sensitive technique.

Author's contribution: Performed image data pre-processing and data analysis, and jointly performed the experiments and wrote the paper with the co-authors.

analytical chemistry

Article

Cite This: *Anal. Chem.* 2019, 91, 12997−13005

pubs.acs.org/ac

Determination of Deposition Order of Toners, Inkjet Inks, and Blue Ballpoint Pen Combining MeV-Secondary Ion Mass Spectrometry and Particle Induced X-ray Emission

Katherine Louise Moore,[†,‡] Marko Barac,[†,§] Marko Brajković,[†] Melanie Jane Bailey,[‡] Zdravko Siketić,[†] and Iva Bogdanović Radović*[,†]

[†]Laboratory for Ion Beam Interactions, Ruđer Bošković Institute, Bijenička 54, HR-10000 Zagreb, Croatia

[‡]Department of Chemistry, University of Surrey, Guildford, Surrey GU2 7XH, U.K.

[§]Jožef Stefan International Postgraduate School, Jamova Cesta 39, 1000 Ljubljana, Slovenia

ABSTRACT: Determination of the deposition order of different writing tools is very important for the forensic investigation of questioned documents. Here we present a novel application of two ion beam analysis (IBA) techniques: secondary ion mass spectrometry using MeV ions (MeV-SIMS) and particle induced X-ray emission (PIXE) to determine the deposition order of intersecting lines made of ballpoint pen ink, inkjet printer ink, and laser printer toners. MeV-SIMS is an emerging mass spectrometry technique where incident heavy MeV ions are used to desorb secondary molecular ions from the uppermost layers of an organic sample. In contrast, PIXE provides information about sample elemental composition through characteristic X-ray spectra coming from greater depth. In the case of PIXE, the information depth depends on incident ion energy, sample matrix and self-absorption of X-rays on the way out from the sample to the X-ray detector. The measurements were carried out using a heavy ion microprobe at the Ruđer Bošković Institute. Principal component analysis (PCA) was employed for image processing of the data. We will demonstrate that MeV-SIMS alone was successful to determine the deposition order of all intersections not involving inkjet printer ink. The fact that PIXE yields information from deeper layers was crucial to resolve cases where inkjet printer ink was included due to its adherence and penetration properties. This is the first time the different information depths of PIXE and MeV-SIMS have been exploited for a practical application. The use of both techniques, MeV-SIMS and PIXE, allowed the correct determination of deposition order for four out of six pairs of samples.

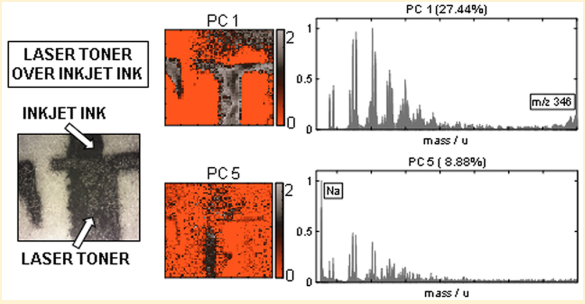

Determination of the deposition order of different writing tools is important in forensic science in the case when questioned documents are analyzed. Although most of the official documents produced today are printed using one of the commercially available printers, signatures are applied using different types of pen. The ability to determine the sequencing of pen and toner lines could help forensic scientists spot forgeries, alterations as well as establish a deposition order in case of questioned documents. Despite the usefulness of a technique for this purpose, most research has focused on identifying the components of pen inks or on intersections involving two pens. Due to printers not being commercially available until more recent years, work involving printed lines is less common,[1] but with the ever-growing use of digital technology is equally important to forensics.

The most recognized techniques for looking at intersecting lines of any kind in forensic daily work are optical methods.[2−4] Physical characteristics can be highlighted by varying light sources and angles giving indications of which line was written second. Optical methods have the benefit of being affordable and entirely nondestructive, but they often struggle when the intersecting lines have similar colors. Optical methods do not provide any information on writing tool chemical composition. Also, there is an element of interpretation meaning the conclusion can vary between examiners.

Lines that cannot be distinguished by optical methods require the use of more sophisticated instruments. Newer techniques for analysis include Raman spectroscopy,[5] atomic force microscopy (AFM),[6] attenuated total reflectance-Fourier transform infrared imaging (ATR-FTIR),[7] and scanning electron microscopy-energy dispersive spectroscopy (SEM-EDS).[8] Each technique has its own benefits and limitations, but still there is no definitive way of distinguishing different writing tools at an intersection.

Time-of-flight-secondary ion mass spectrometry (TOF-SIMS) is a highly sensitive surface technique that provides high lateral resolution information. It has already been applied

Received: July 6, 2019
Accepted: September 17, 2019
Published: September 17, 2019

DOI: 10.1021/acs.analchem.9b03058
Anal. Chem. 2019, 91, 12997−13005

for investigating the sequencing of inks and toners. In one study, three different black inks were tested[9] and the technique successfully distinguished the inks from each other, but one of the three inks dominated all the intersections leading to incorrect deposition order determinations. Another paper looked at the intersections of various colored pen inks with successful results.[10] TOF-SIMS has also been applied to inks, toners, and stamp inks in conjunction with ATR-FTIR.[11,12] Due to TOF-SIMS extended mass range and higher sensitivity, the intersections that could not be determined using ATR-FTIR were successfully determined using the TOF-SIMS instrument.

Secondary ion mass spectrometry using MeV ions (MeV-SIMS) is a technique where secondary molecular ions are desorbed from the sample surface after the passage of MeV ions. As MeV ions interact with the surface layer only through electronic stopping, less fragmentation is expected than in the case of TOF-SIMS with keV ions. So far, this technique has been applied to determine the deposition order of blue ballpoint pen ink lines.[13] Six different blue ballpoint pens were used, and the deposition order for all combinations of them was determined with success. It has also shown success determining if a fingerprint is above or below ink lines[14−16] and identifying and imaging of different synthetic organic pigments.[17]

Particle induced X-ray emission (PIXE) analysis has previously been relatively unused for order determination of intersecting lines because alone it provides very little information to distinguish depths. Furthermore, because it is not a surface technique, a lot of background from the bulk paper is present in spectra which interferes with the ink and toner line signals. However, it is frequently used for elemental analysis of pen samples and historical documents.[18] In the present work, the potential for applying MeV-SIMS and PIXE to intersecting ink/toner lines was investigated.

EXPERIMENTAL SECTION

Measurements were performed using the Ruđer Bošković Institute (RBI) heavy ion microprobe. MeV-SIMS measurements were performed using an attached MeV-SIMS setup with a time-of-flight spectrometer described in detail in Tadić et al.[19] MeV-SIMS measurements were performed prior to PIXE because we have previously shown that MeV-SIMS solely was sufficient to determine the correct deposition order for all cases where blue ballpoint pens were involved, due to the technique's surface sensitivity.[13] Measurements were carried out under vacuum (10^{-6}−10^{-7} mbar), and 8 MeV Si^{4+} ions were employed for the analysis with a lateral beam resolution of approximately 5 μm × 5 μm. Smaller sample areas (100 × 100 μm) were scanned first, far from the intersection region to define the mass spectrum of each ink and toner. After that, the intersection region up to 1200 μm × 1200 μm was scanned for imaging. The beam current in pulsed mode was about 0.2 fA. Primary ion fluence corresponding to approximately 15 min of measurement for each sample was 2×10^7 ions/cm^2. A +5 kV voltage was applied to the sample holder to direct the secondary molecular ions toward the TOF extractor. A multistop time-to-digital converter (TDC) data acquisition system in the heavy ion deflection start mode was used with 100 μs between the ion pulses of 4 ns duration.

PIXE was employed on the same set of samples in the same microprobe chamber using a 2 MeV proton beam with a lateral beam resolution of approximately 5 × 5 μm^2. The scanned intersection region was 800 × 800 μm^2, and the beam current was about 80 pA. Primary ion fluence corresponding to approximately 10 min of measurement for each sample was 4.6×10^{13} ions/cm^2. SPECTOR[18,20] software was used to control all parameters and data acquisition during the experiment. Basic spectra inspection was carried out using mMass.[21] Principal component analysis (PCA) was employed on images using the Matlab tool simsMVA[22] to enhance the contrast between different chemical compositions of each pixel. The manufacturers and models of each of the writing tools used in samples are presented in Table 1. Samples for the measurements were produced using one blue ballpoint pen, three different laser printers, and two different inkjet printers, to give a total of 12 samples.

Table 1. Writing Tools Manufacturers and Models

writing tool	manufacturer	model	color of ink
ballpoint pen	HiText	Grip 901	blue
laser printer 1	HP	Laser Jet pro 400 color MFP m475	black
laser printer 2	HP	Laser Jet p1606dn	black
laser printer 3	HP	Color Laser Jet 4600 hdn	black
inkjet printer 1	Canon	PIXMA ix6550	black
inkjet printer 2	HP	PHOTOSMART C5180 ALL-IN-ONE	black

Each combination of one ink/toner above the other was made. The pen lines were all deposited by the same person maintaining a normal writing pressure. A section of the paper roughly 1 × 1 cm^2 incorporating the intersection was cut using tweezers and scissors and mounted on a silicon wafer using double-sided carbon tape. A microscope photo was also taken of each sample to give a reference image. Given that the primary ion fluence for MeV-SIMS does not exceed the static limit, radiation damage to the samples is presumed to be negligible. Thus, it was assumed that the same samples could be reused for the PIXE measurements with no alterations necessary. Figure 1

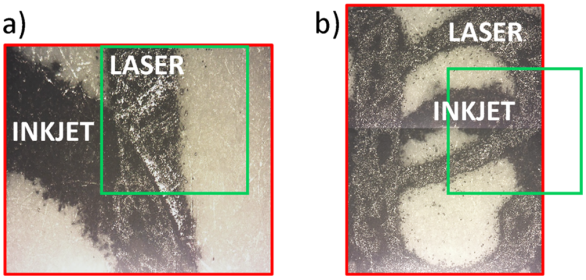

Figure 1. Microscopic images of samples: (a) laser toner 3 on inkjet ink 2 and (b) inkjet ink 2 on laser toner 3. Red and green frame colors indicate MeV-SIMS and PIXE approximate scan areas, respectively.

shows microscopic images of samples: (a) laser toner 3 on inkjet ink 2 and (b) inkjet ink 2 on laser toner 3. Rectangles indicate MeV-SIMS (red) and PIXE (green) approximate scan area. Corresponding MeV-SIMS mass and PIXE X-ray spectra of ballpoint pen ink, inkjet ink 2, laser toner 3, and plain paper are displayed in Figures 2 and 3, respectively. PIXE X-ray spectra of ballpoint pen ink did not yield any significant peaks that are different from the X-ray spectrum of the paper.

DOI: 10.1021/acs.analchem.9b03058
Anal. Chem. 2019, 91, 12997−13005

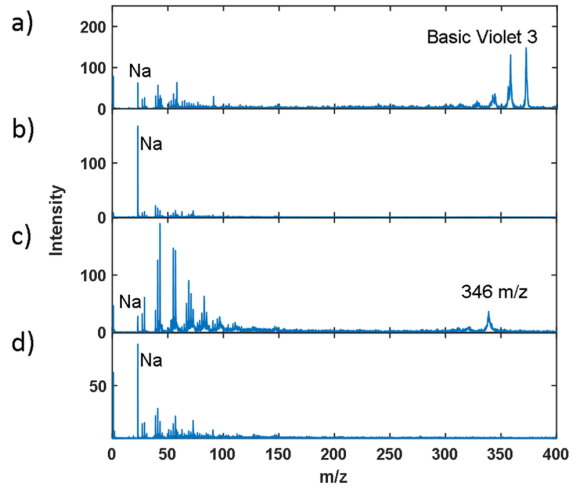

Figure 2. Individual mass spectra of (a) ballpoint pen ink, (b) inkjet ink 2, (c) laser toner 3, and (d) plain paper.

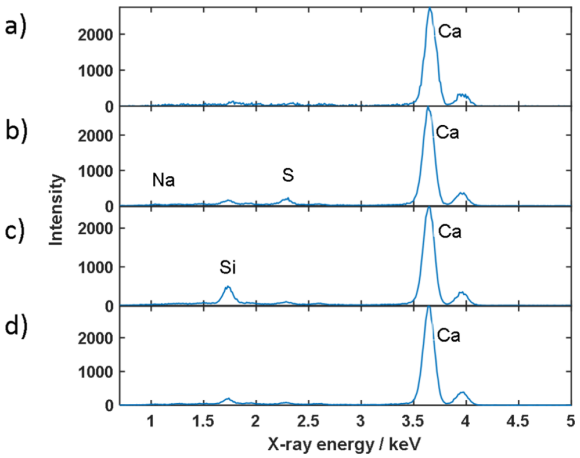

Figure 3. Individual PIXE spectra of (a) ballpoint pen ink, (b) inkjet ink 2, (c) laser toner 3, and (d) plain paper.

RESULTS AND DISCUSSION

MeV-SIMS. All 12 samples were analyzed with MeV-SIMS. Because MeV-SIMS is a surface technique, it means that only molecules desorbed from the uppermost layer of the sample are detected, and therefore the deposition order can be determined by looking at breaks in mapped image lines. The line deposited first should have a break while the line deposited second should be continuous. Also, the continuous line should have a thickness that matches that of the break.

PCA, a multivariate statistical analysis, was employed on all obtained hyperspectral images. In some cases, a pixel binning of factor 2 was used due to a small number of counts per pixel, resulting in images of 64 × 64 pixels. Poisson scaling together with mean centering was applied in the preprocessing of images. PCA was performed via singular value deposition (SVD) with the use of sparse matrices. A predetermined number of 6 PCs for each case was set. Score maps of those PCs that represent the best contrast between writing tools or highlight a specific tool in an image are shown in Figures 4−9, with the results marked as correct or incorrect. Loading plots, showing significant mass peaks that contribute the most to the contrast of associated score map, are shown only in Figures 4 and 5 for simplicity (corresponding microscopic images of the two cases are shown in Figure 1). A discussion on the nature of the incorrect results is given later on.

PCA analysis yielded good image contrast and mostly managed to distinguish between different writing tools based on the full mass spectra variance across pixels. It also detected major peaks contributing to those variances. Some peaks were already used in a simple preliminary RGB analysis prior to PCA, as they were easily recognized looking at the differences between spectra: lithium (m/z 7) for inkjet ink 1, sodium (m/z 23) for laser toner 1 and 2, and Basic Violet 3 (BV3) (m/z 372) for blue ballpoint pen ink. However, in the case of laser toners 1 and 2, PCA managed to detect some peaks in the lower mass region (m/z 55, 69, and 83) that have slightly higher intensities in laser toners 1 and 2 than in paper or inkjet ink 1. Similar to the inkjet ink 1, inkjet ink 2 is easily distinguishable from laser toner 3 using its most prominent sodium peak (m/z 23), but it does not contain any lithium. Laser toner 3 has an unknown peak at around m/z 346 and 648 and a lack of sodium which was used to identify it.

Out of the six pairs of samples, each pair is comprised of two combinations with respect to deposition order of the present writing tools, and two pairs correctly showed a break in the line deposited first, the pair containing ballpoint pen and laser toner 1 and the pair containing ballpoint pen and laser toner 2 (the latter is shown in Figure 9a,b). All the pairs involving inkjet ink caused problems when the inkjet ink was on top (Figures 5−8a). Whether the inkjet line was deposited first or second, it always showed a break and the other line was always continuous, meaning that all interactions including inkjet ink could not be reliably established using MeV-SIMS alone. Because MeV-SIMS is a surface technique, this leads to a hypothesis that (a) either the inkjet ink must be going below the other line into the paper or (b) the inkjet ink was not adhering at the intersection at all. If it was not adhering, one may expect to see unabsorbed drops of ink. Unabsorbed drops of inkjet ink left on a layer of another writing tool at the intersection are usually noticed by microscopic methods, meaning it should also be possible for MeV-SIMS to detect them since they are present at the surface. However, in our case the inkjet ink 1 is characterized by a unique but low abundance of lithium, whereas the inkjet ink 2 is distinguished using different amounts of sodium with respect to the rest of the sample. In both cases, the attributes are not prominent or specific enough to significantly contribute to the overall mass spectrum in areas possibly containing drops. Consequently, it could be said that the detection limit is too low. Unfortunately, there were no higher-order PCs that highlighted a combination of laser toner and inkjet ink in the overlapping areas.

PIXE. In order to further investigate the behavior of inkjet inks interacting with other writing tools at the intersection, PIXE was used on the eight remaining samples involving inkjet ink. The laser toner 1 and laser toner 2 with ballpoint pen line combinations were not analyzed using PIXE because these were adequately differentiated using solely MeV-SIMS, so no further analysis was necessary. As opposed to MeV-SIMS, PIXE is not surface sensitive and it gives information from larger depths requiring only that the characteristic X-rays emitted from the sample are energetic enough to leave the sample and reach the X-ray detector.

DOI: 10.1021/acs.analchem.9b03058
Anal. Chem. 2019, 91, 12997−13005

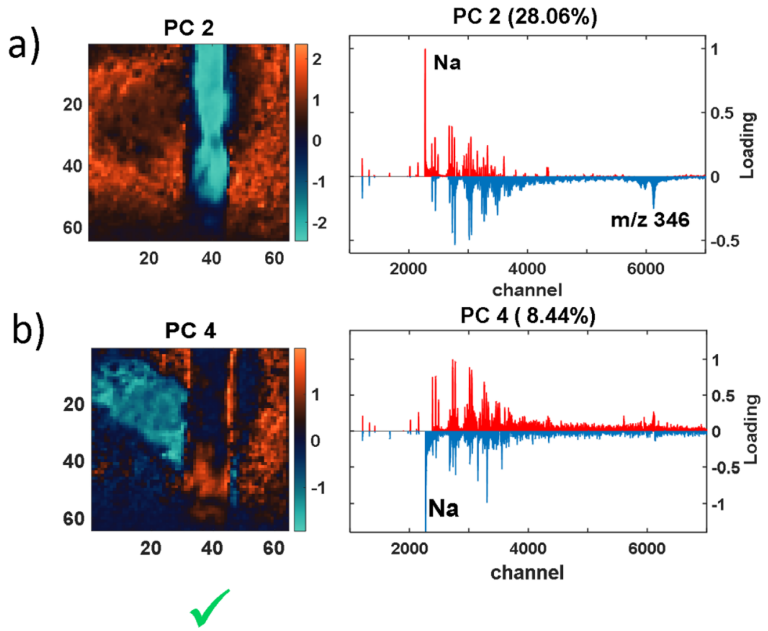

Figure 4. MeV-SIMS of laser toner 3 on inkjet ink 2: (a) PC2 (28.06%) map of laser toner 3 and the corresponding loading plot and (b) PC4 (8.44%) map of inkjet ink 2 and the corresponding loading plot.

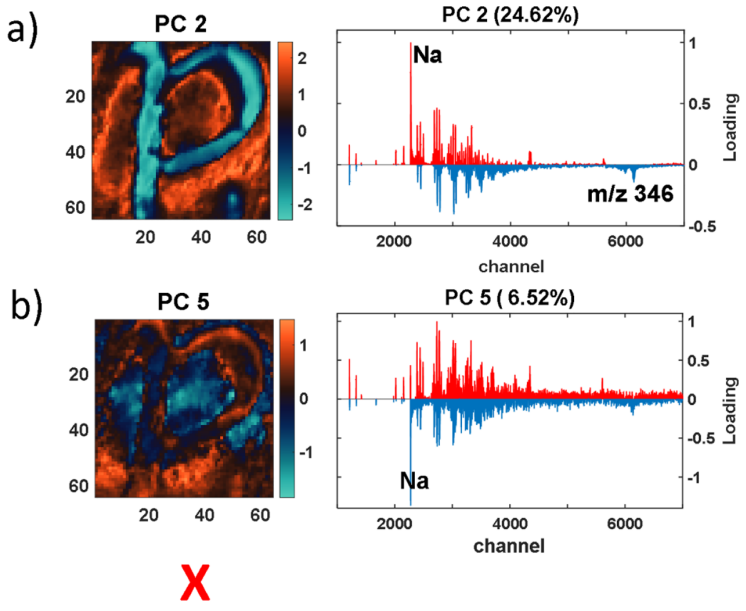

Figure 5. MeV-SIMS of inkjet ink 2 on laser toner 3: (a) PC2 (24.62%) map of laser toner 3 and the corresponding loading plot and (b) PC5 (6.52%) map of inkjet ink 2 and the corresponding loading plot.

PCA analysis of PIXE maps gave a clearer explanation for some of the cases. The line belonging to the inkjet ink will appear continuous at the intersection in two cases, the first is when the inkjet ink was deposited first, and the second when the inkjet ink is deposited second but is penetrating through the layer of the other writing tool (laser toner or ballpoint pen). The line belonging to the inkjet ink will have a break at the intersection only in the case when it is deposited second and when it is not adhering to the already deposited writing tool.

PCA analysis of PIXE maps of a pair of samples involving laser toner 3 and inkjet ink 2 resulted in maps shown in Figures 10 and 11. Data was standardized (centered to have mean 0 and scaled to have standard deviation 1) prior to the analysis. Microscopic images of these samples, together with labeled writing tools, are shown in Figure 1.

Loading plots for PC1 in both cases represent the paper and are not shown here. It is clear from Figure 10b that PIXE detected inkjet ink 2 from below laser toner 3 at the point of intersection, mainly from sulfur X-rays (sodium X-rays are

DOI: 10.1021/acs.analchem.9b03058
Anal. Chem. 2019, 91, 12997−13005

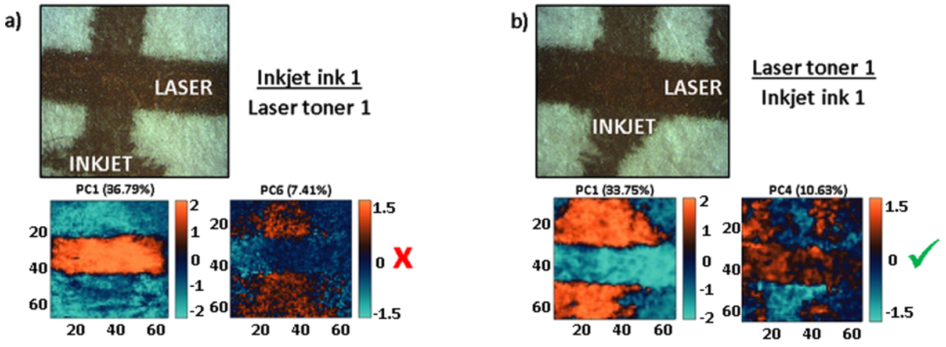

Figure 6. MeV-SIMS microscopic images of inkjet ink 1 and laser toner 1 and the corresponding PCA maps, highlighting the differences. Parts a and b denote two possible combinations of order.

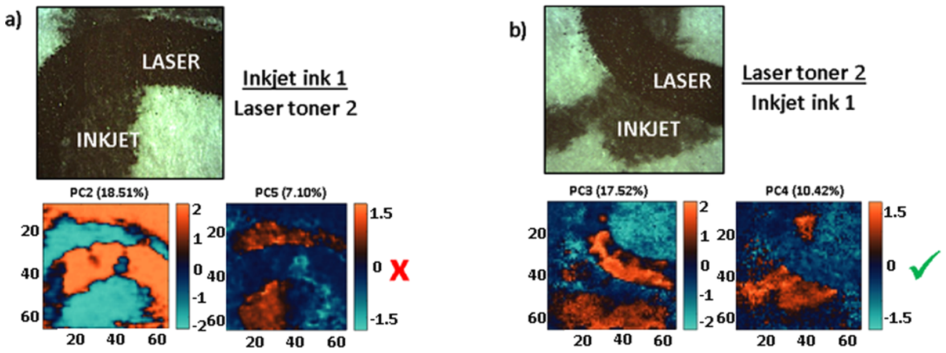

Figure 7. MeV-SIMS microscopic images of inkjet ink 1 and laser toner 2 and the corresponding PCA maps, highlighting the differences. Parts a and b denote two possible combinations of order.

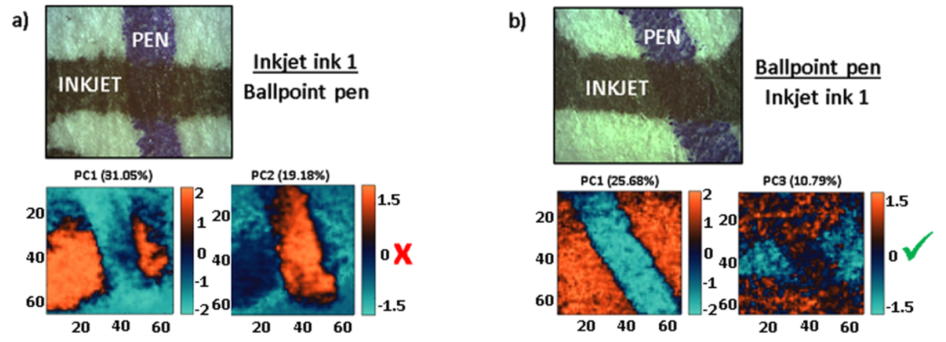

Figure 8. MeV-SIMS microscopic images of inkjet ink 1 and ballpoint pen and the corresponding PCA maps, highlighting the differences. Parts a and b denote two possible combinations of order.

mostly absorbed in the sample before they reach the surface, except in areas away from the intersection). However, in the case when inkjet ink 2 was on top as in Figure 11b, there is an evident break in the line at the point of intersection, which leads to a conclusion that there is no inkjet ink 2 deposited at all and that the substance below has prevented its absorption in the paper, in this case, laser toner 3. Also, there is a higher amount of sodium X-rays detected with respect to sulfur, which favors a hypothesis that there is no "hidden" area of inkjet ink 2 under a layer of laser toner 3 which would absorb emitted low energy sodium X-rays. Similarly, score maps for the rest of the samples and their microscopic images are shown in Figures 12−14, with the results marked as correct or incorrect. Significant X-ray peak that contributed to highlighting of all laser toners is the Si peak and the one highlighting all inkjet inks is the S peak.

■ DISCUSSION

Table 2 shows the complete collection of results obtained using both MeV-SIMS and PIXE. We successfully determined the deposition order of 4 out of the 6 pairs of samples. Figure 15 shows a basic diagram depicting the different properties of the three writing tools, based on assumptions from this experiment. There is some variation between brands and types of printer. However, most commonly inkjet printers use water-based ink, ballpoint pen uses oil-based ink, and laser printers use a wax-based toner. Inkjet ink tends to be mainly composed of water,[23]

DOI: 10.1021/acs.analchem.9b03058
Anal. Chem. 2019, 91, 12997−13005

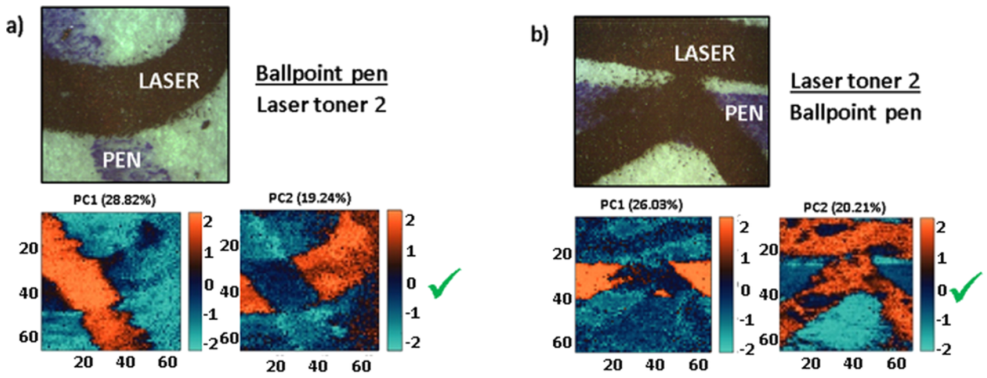

Figure 9. MeV-SIMS microscopic images of ballpoint pen and laser toner 2 and the corresponding PCA maps, highlighting the differences. Parts a and b denote two possible combinations of order. Samples involving combinations of a ballpoint pen and laser toner 1 are not shown because they yielded the same results as the samples involving combinations of a ballpoint pen and laser toner 2.

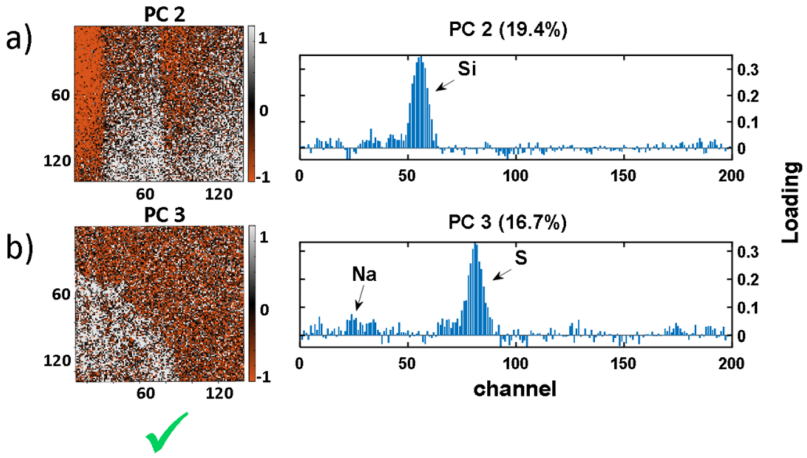

Figure 10. Laser toner 3 on inkjet ink 2: (a) PC2 map of laser toner 3 and its loading plot and (b) PC3 map of inkjet ink 2 and its loading plot.

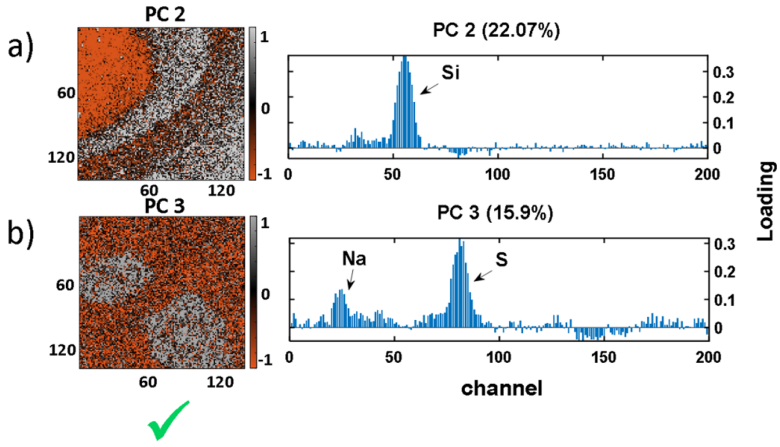

Figure 11. Inkjet ink 2 on laser toner 3: (a) PC2 map of laser toner 3 and its loading plot and (b) PC3 map of inkjet ink 2 and its loading plot.

meaning it penetrates deep into the paper and any remaining ink on the surface evaporates. Ballpoint pen ink, on the other hand, is oil-based, it has a relatively similar composition with the main difference being the choice of solvent and, as a result, the viscosity. It both penetrates into the paper and forms a membrane on top.[24] Laser printers work by melting a layer of resin to the surface of the paper.[25]

MeV-SIMS indicated that the inkjet ink was not present on top of the intersection in the case where it should have been. Initially, it was proposed this may be because the inkjet ink was

DOI: 10.1021/acs.analchem.9b03058
Anal. Chem. 2019, 91, 12997−13005

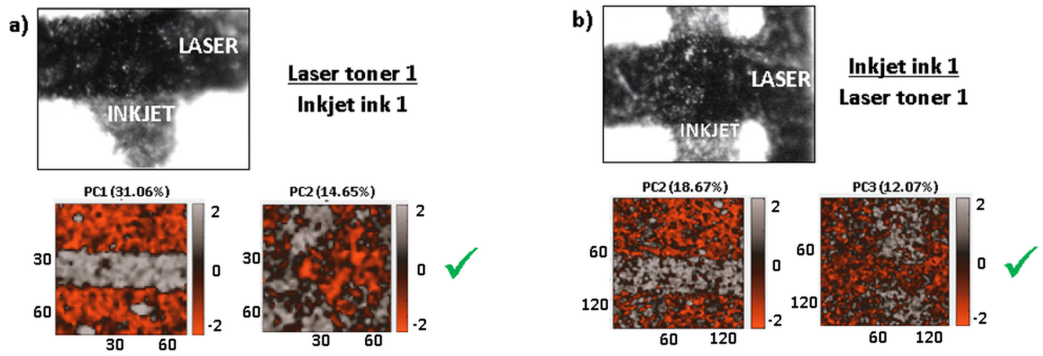

Figure 12. PIXE microscopic images of inkjet ink 1 and laser toner 1 and the corresponding PCA maps highlighting differences.

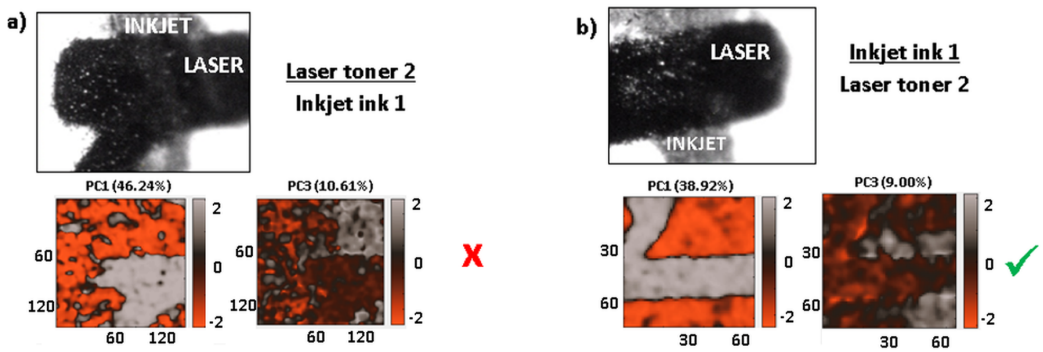

Figure 13. PIXE microscopic images of inkjet ink 1 and laser toner 2 and the corresponding PCA maps highlighting differences.

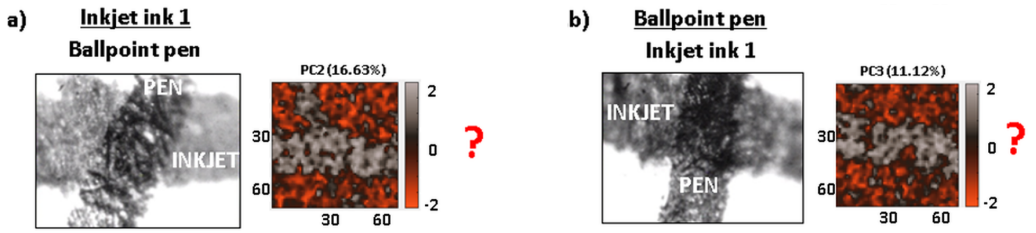

Figure 14. PIXE microscopic images of inkjet 1 and ballpoint pen and the PCA maps showing traces of inkjet ink because the ballpoint pen has not emitted any detectable X-rays.

Table 2. Overall Results of MeV-SIMS and PIXE Measurements of Intersecting Lines[a]

	MeV-SIMS results				MeV-SIMS and PIXE combined results			
combination	break	continuous	success	reliably distinguishable	break	continuous	success	reliably distinguishable
inkjet ink 1/laser toner 1	inkjet ink	laser	×	×	inkjet ink	laser	√	√
laser toner 1/inkjet ink 1	inkjet ink	laser	√			inkjet ink, laser	√	
inkjet ink 1/laser toner 2	inkjet ink	laser	×	×	inkjet ink	laser	√	×
laser toner 2/inkjet ink 1	inkjet ink	laser	√		inkjet ink	laser	×	
inkjet ink 1/ballpoint pen	inkjet ink	ballpoint pen	×	×	?	inkjet ink, ?	×	×
ballpoint pen/inkjet ink 1	inkjet ink	ballpoint pen	√		?	inkjet ink, ?	×	
ballpoint pen/laser toner 1	laser	ballpoint pen	√	√				
laser toner 1/ballpoint pen	ballpoint pen	laser	√					
ballpoint pen/laser toner 2	laser	ballpoint pen	√	√				
laser toner 2/ballpoint pen	ballpoint pen	laser	√					
inkjet ink 2/laser toner 3	inkjet ink	laser	×	×	inkjet ink	laser	√	√
laser toner 3/inkjet ink 2	inkjet ink	laser	√			inkjet ink, laser	√	

[a]Two pairs of cases remained unresolved.

DOI: 10.1021/acs.analchem.9b03058
Anal. Chem. 2019, 91, 12997−13005

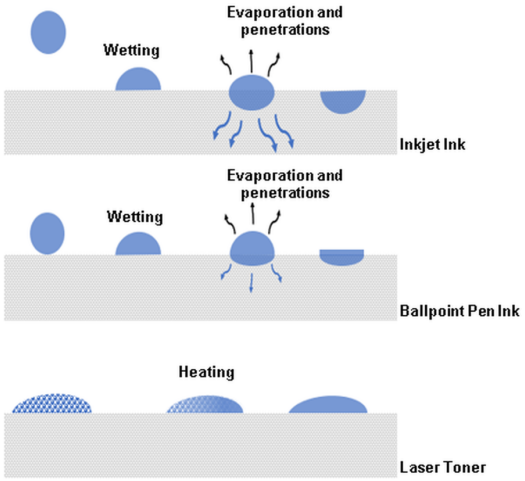

Figure 15. Diagram of ink penetration and drying methods

penetrating through the other inks deep into the paper. However, by using PIXE we were able to image the intersection below the surface and see this was not the case. It was then proposed that perhaps the presence of the other ink between the inkjet ink and the paper was preventing it from adhering and penetrating into the paper entirely.

By combining both MeV-SIMS and PIXE, one can say that if there is a break in the inkjet line in both SIMS and PIXE, then there is no ink at the intersection and conclude that it must have been prevented from adhering to the paper, therefore deposited second. However, two of the six pairs of samples were unsuccessfully distinguished even with both MeV-SIMS and PIXE. When mapped, the sample with laser printer 2 and inkjet ink 1 showed a break in the inkjet ink line whether it was above or below at the intersection. This is most likely due to the thickness of this particular laser toner and the amount of iron in its composition preventing the X-rays from the inkjet ink line reaching the detector. The other unsuccessful pair of samples was those containing the ballpoint pen and inkjet ink 1. The pen had no characteristic X-rays that could be used for mapping and distinguishing it from inkjet ink and paper. This means that the samples could not be mapped with PIXE and so were also unable to be distinguished.

CONCLUSIONS

The MeV-SIMS technique successfully determined the deposition order of intersections involving laser toners 1 and 2 and ballpoint pen. However, the sequencing of lines involving inkjet ink proved to be more challenging when the inkjet ink was on top. PIXE measurements of the problematic cases together with MeV-SIMS results contributed to understanding the behavior of inkjet ink at the intersection and helped resolve the issue in most cases. Further analysis using more inkjet inks in combination with different writing tools is needed to establish the wider benefits of MeV-SIMS and PIXE. Also, optimizing the MeV-SIMS setup to detect unabsorbed drops of inkjet ink left on the intersection could improve incorrect results and should be investigated.

MeV-SIMS has proved to be a promising technique. Because of the limitations of chamber size, the technique as it is requires sampling (a sample needs to be cut and mounted on a sample holder in a vacuum chamber), which is not ideal for forensic purposes. However, there is work underway for ambient pressure MeV-SIMS (AP MeV-SIMS),[26] which would remove the restraints of chamber size meaning the document would remain intact even after the analysis. On the other hand, AP MeV-SIMS is struggling with some difficulties which do not exist in vacuum MeV-SIMS measurements, such as limitations in term of available heavy-ion beams due to the exit window thickness and more complex mass spectra due to the signal coming from the ambient. Also, the extraction of the secondary molecular ions from the sample to the mass spectrometer is currently inefficient.

AUTHOR INFORMATION

Corresponding Author

*E-mail: iva@irb.hr.

ORCID

Melanie Jane Bailey: 0000-0001-9050-7910

Iva Bogdanović Radović: 0000-0002-4100-736X

Notes

The authors declare no competing financial interest.

ACKNOWLEDGMENTS

K.L.M. acknowledges that the project was cofunded by the Erasmus+ program of the European Union. The European Commission's support for the production of this publication does not constitute an endorsement of the contents, which reflects the views only of the authors, and the Commission cannot be held responsible for any use which may be made of the information contained therein. I.B.R. and Z.S. acknowledge support by the HORIZON 2020 Project RADIATE under the Grant Agreement 824096, COST Action Grant CA16101 (Multi-Foresee), and IAEA CRP F11021. The authors also acknowledge Ms. Andrijana Filko from the Forensic Science Center "Ivan Vučetić" for providing some of the samples and fruitful discussion. M. Brajković acknowledges support by the Croatian Science Foundation Project "Young Researchers' Career Development Project—Training of Doctoral Students" cofinanced by the European Union, Operational Program "Efficient Human Resources 2014—2020", and the ESF. M. J. Bailey acknowledges EPSRC Grant EP/R031118/1: Ion Beam Analysis for the 2020s and beyond: An Integration of Elemental Mapping and 'omics', for contributing her time to work on this project

REFERENCES

(1) e Brito, L. v. R.; Martins, A. R.; Braz, A.; Chaves, A. B.; Braga, J. W.; Pimentel, M. F. *TrAC, Trends Anal. Chem.* **2017**, *94*, 54—69.

(2) Saini, K.; Kaur, R.; Sood, N. C. *Sci. Justice* **2009**, *49*, 286—291.

(3) Ozbek, N.; Braz, A.; Lopez-Lopez, M.; Garcia-Ruiz, C. *Forensic Sci. Int.* **2014**, *234*, 39—44.

(4) Saini, K.; Kaur, R.; Sood, N. C. *Forensic Sci. Int.* **2009**, *193*, 14—20.

(5) Borba, F. d. S. L.; Jawhari, T.; Saldanha Honorato, R.; de Juan, A. *Analyst* **2017**, *142*, 1106—1118.

(6) Kasas, S.; Khanmy-Vital, A.; Dietler, G. *Forensic Sci. Int.* **2001**, *119*, 290—298.

(7) Bojko, K.; Roux, C.; Reedy, B. J. *J. Forensic Sci.* **2008**, *53*, 1458—1467.

(8) Kim, J.; Kim, M.; An, J.; Kim, Y. *J. Forensic Sci.* **2016**, *61*, 803—808.

(9) Goacher, R. E.; DiFonzo, L. G.; Lesko, K. C. *Anal. Chem.* **2017**, *89*, 759—766.

(10) He, A.; Karpuzov, D.; Xu, S. *Surf. Interface Anal.* **2006**, *38*, 854—858.

(11) Lee, J.; Nam, Y. S.; Min, J.; Lee, K.-B.; Lee, Y. *J. Forensic Sci.* **2016**, *61*, 815—822.

DOI: 10.1021/acs.analchem.9b03058
Anal. Chem. 2019, 91, 12997—13005

(12) Lee, J.; Kim, S. H.; Cho, Y.-J.; Nam, Y. S.; Lee, K.-B.; Lee, Y. *Surf. Interface Anal.* **2014**, *46*, 317−321.
(13) Malloy, M. C.; Bogdanović Radović, I.; Siketić, Z.; Jakšić, M. *Forensic Chem.* **2018**, *7*, 75−80.
(14) Bailey, M. J.; Jones, B. N.; Hinder, S.; Watts, J.; Bleay, S.; Webb, R. P. *Nucl. Instrum. Methods Phys. Res., Sect. B* **2010**, *268*, 1929−1932.
(15) Bright, N. J.; Webb, R. P.; Bleay, S.; Hinder, S.; Ward, N. I.; Watts, J. F.; Kirkby, K. J.; Bailey, M. J. *Anal. Chem.* **2012**, *84*, 4083−4087.
(16) Attard Montalto, N.; Ojeda, J. J.; Jones, B. J. *Sci. Justice* **2013**, *53*, 2−7.
(17) Bogdanović Radović, I.; Siketić, Z.; Jembrih-Simbürger, D.; Marković, N.; Anghelone, M.; Stoytschew, V.; Jakšić, M. *Nucl. Instrum. Methods Phys. Res., Sect. B* **2017**, *406*, 296−301.
(18) Budnar, M.; Uršič, M.; Simčič, J.; Pelicon, P.; Kolar, J.; Šelih, V. S.; Strlič, M. *Nucl. Instrum. Methods Phys. Res., Sect. B* **2006**, *243*, 407−416.
(19) Tadić, T.; Bogdanović Radović, I.; Siketić, Z.; Cosic, D. D.; Skukan, N.; Jakšić, M.; Matsuo, J. *Nucl. Instrum. Methods Phys. Res., Sect. B* **2014**, *332*, 234−237.
(20) Bogovac, M.; Bogdanović, I.; Fazinić, S.; Jakšić, M.; Kukec, L.; Wilhelm, W. *Nucl. Instrum. Methods Phys. Res., Sect. B* **1994**, *89*, 219−222.
(21) Strohalm, M.; Hassman, M.; Kosata, B.; Kodicek, M. *Rapid Commun. Mass Spectrom.* **2008**, *22*, 905−908.
(22) Trindade, G. F.; Abel, M.-L.; Watts, J. F. *Chemom. Intell. Lab. Syst.* **2018**, *182*, 180−187.
(23) Le, H. P. *J. Imaging Sci. Technol.* **1998**, *42*, 49−62.
(24) Kobilinsky, L. *Forensic Chemistry Handbook*; John Wiley & Sons, Inc., 2011.
(25) Li, B.; Ouyang, G. l.; Zhao, P. n. *J. Forensic Sci.* **2018**, *63*, 577−582.
(26) Matjačić, L.; Palitsin, V.; Grime, G. W.; Abdul-Karim, N.; Webb, R. P. *Nucl. Instrum. Methods Phys. Res., Sect. B* **2019**, *450*, 353−356.

DOI: 10.1021/acs.analchem.9b03058
Anal. Chem. 2019, 91, 12997−13005

3.2 Comparison of Optical Techniques and MeV SIMS in Determining Deposition Order Between Optically Distinguishable and Indistinguishable Inks from Different Ballpoint Pens

In this subchapter, intersections of inks from several writing tools were studied using optical techniques that are standardly applied for questioned documents examination in the Forensic Science Centre "Ivan Vučetić", and MeV SIMS that is applied in the accelerator facility at Ruđer Bošković Institute. The aim of this study was to compare the performance of optical techniques and MeV SIMS for several combinations of intersecting lines. For that reason, cases were divided into those in which optical techniques can distinguish used inks and those which are optically completely indistinguishable. Optical methods generally proved to have difficulties with water-based inks, similar to MeV SIMS, which was established in the previous study. Nevertheless, optical techniques slightly outperformed MeV SIMS in determining the deposition order for intersections of optically distinguishable inks from different writing tools where both oil-based and water-based inks were used. MeV SIMS images were processed with PCA, although in cases with optically identical inks PCA could not distinguish the two inks in a system and only managed to describe the variance between the paper and the two inks together. In these cases, both inks in a system happened to yield almost identical mass spectra, as well. Thus, t-SNE was applied instead, assuming better performance due to its non-linear nature and sensitivity to subtle variations in the dataset. This resulted in successful differentiation of both inks in both optically identical cases, and successful determination of deposition order in one case. To the best of author's knowledge, at the time of publishing, utilizing t-SNE with MeV SIMS images has not yet been attempted.

Author's contribution: Performed image data pre-processing and data analysis, and jointly performed the experiments and wrote the paper with the co-authors.

Forensic Science International 331 (2021) 111136

Contents lists available at ScienceDirect

Forensic Science International

journal homepage: www.elsevier.com/locate/forsciint

Comparison of optical techniques and MeV SIMS in determining deposition order between optically distinguishable and indistinguishable inks from different writing tools

Marko Barac[a,*], Andrijana Filko[b], Zdravko Siketić[a], Marko Brajković[a], Andrea Ledić[b], Iva Bogdanović Radović[a]

[a] Division of Experimental Physics, Ruđer Bošković Institute, Bijenička 54, 10000 Zagreb, Croatia
[b] Forensic Science Centre "Ivan Vučetić", Ilica 335, 10000 Zagreb, Croatia

ARTICLE INFO

Article history:
Received 28 September 2021
Received in revised form 9 November 2021
Accepted 1 December 2021
Available online 3 December 2021

Keywords:
Forensic document examination
Crossing ink lines
Optical techniques
MeV SIMS

ABSTRACT

In the forensic investigation of questioned documents, it is often very important to know the deposition order of ink traces from two different writing tools at their intersection on a paper. In the present work, intersections of inks from several writing tools were studied using optical techniques that are standardly applied for questioned documents examination in a forensic laboratory, and an accelerator-based Ion Beam Analysis (IBA) technique called Secondary Ion Mass Spectrometry using MeV ions (MeV SIMS) that is applied in an accelerator facility. MeV SIMS provides molecular information about the studied inks from writing tools, which is an added value and can be also applied for determination of deposition order but was so far relatively rarely used in forensic studies. Aim of this paper is to compare performance of optical techniques and MeV SIMS for several combinations of intersecting lines. Cases were divided into those in which optical techniques can distinguish used inks and those which are optically completely indistinguishable. In the latter cases, we show that although mass spectra of used inks (from blue ballpoint pens) had extremely small differences, these in combination with advanced and most importantly objective multivariate algorithms could be very beneficial in resolving the deposition order at the intersection of optically indistinguishable inks. In general, MeV SIMS proved to be more efficient for oil-based inks while difficulties were encountered with water-based ones, similar to optical methods.

1. Introduction

Today, most of the official documents, such as contracts or testaments, which are often the subject of counterfeiting, are produced with commercially available printers. On such documents, a stamp impression or signatures using different types of pens are also applied. The places where such ink traces intersect may reveal if the document is original or was modified in any way after the moment it was produced. Various techniques have been introduced in the forensic work to solve the problem of intersecting lines. Recently, a comprehensive review of different methods that were used so far was given in the work of e Brito et al. [1]. In their work, all the techniques ranging from optical methods, introduced in the '60s and '70s, over lifting techniques, electronic microscopy, chemical and surface analysis, introduced at the beginning of this century, and finally hyperspectral imaging and chemometrics, introduced in the last decade, were critically assessed. The advantages and limitations of all the techniques, as well as their efficiency in revealing proper deposition order were also discussed. It was emphasized that optical methods that are non-destructive, fast, and easy to apply will probably remain prevalent in the daily forensic work and that the need for other analytical techniques, which are more expensive and complicated to perform, sometimes destructive and time consuming would appear in more complex cases where the information obtained from optical methods is inconclusive and not sufficient to give a proper answer.

The forensic laboratory in which the analysis of intersections is conducted is the only specialized institution for forensic examination in the Republic of Croatia. Handwriting and document examination has been conducted ever since the very establishment in 1953. In 1998, handwriting and document experts became full members of handwriting and document expert working groups

* Correspondence to: Ruđer Bošković Institute, Bijenička 54, 10000 Zagreb, Croatia.
E-mail address: mbarac@irb.hr (M. Barac).

https://doi.org/10.1016/j.forsciint.2021.111136
0379-0738/

within the European Network of Forensic Science Institutes (ENFSI) [2]. In 2010, the Centre formally became an accredited laboratory in accordance with the international standard ISO 17025. The Laboratory for forensic handwriting and document examination is equipped with state-of-the-art instruments. Document forensic experts are conducting analyses of questioned documents on a daily basis. From a total number of questioned document cases, only about 10% of the cases involve determination of chronological sequence of inks from two or more writing tools, i.e. intersecting lines. The examination procedures depend on the nature of the intersection areas and no technique is known which is applicable to the whole range of cases with intersecting lines [3]. The examination is most often conducted by using non-destructive techniques, but in some cases, semi-destructive techniques such as Raman spectroscopy may also be applied. Standard non-destructive examinations, including optical microscopic techniques and IR absorption/luminescence, are performed first. The forensic document and handwriting experts at the forensic laboratory conduct examination of intersecting lines mainly using non-destructive optical methods, but these are not sufficient in some real-life cases. The purpose of this paper was to seek another reliable method to help resolve such cases, specifically the ones that involve inks with very similar composition.

Time-of-flight Secondary Ion Mass Spectrometry (TOF-SIMS) using keV ions is a surface technique that provides chemical information from the uppermost few monolayers with superior lateral resolution and was applied for the first time to determine deposition order on intersecting lines for different ballpoint and fountain pens by He et al [4]. In combination with attenuated total reflectance-Fourier transform infrared imaging (ATR-FTIR), TOF-SIMS was used to analyze inks, toners, and stamp inks [5,6]. Also, sequences of intersections made with black ballpoint pens were studied recently by Goacher et al [7]. Those studies have shown high potential of the technique in analyzing intersecting lines, but also introduced a problem in solving cases that involve inks from writing tools that penetrate deeper into the paper. For the last ten years, several laboratories around the world, among them the accelerator facility in which the analysis of intersections is performed, have started to use MeV ions for desorption of secondary molecular ions from the sample surface, the so-called MeV Secondary Ion Mass Spectrometry (MeV SIMS) technique. In case when MeV ions are used instead of keV ions, higher secondary molecular ion yields are expected as well as less fragmentation of large molecules, since the dominant mechanism of interaction of MeV ions with the sample surface is electronic instead of nuclear stopping, which dominates when keV ions are used. Concerning forensic examination of questioned documents, the technique has demonstrated success in determining deposition order of fingerprints and inks on paper [8]. In the case of intersecting lines made by blue ballpoint pens [9], deposition order of all studied combinations was determined with success. The situation was not so clear in some cases when deposition order of laser toners, inkjet inks and ballpoint pens was studied [10]. The cases including laser toner and ballpoint pen were solved successfully using only MeV SIMS technique, but the problem to reveal deposition order in cases where inkjet ink was present remained unsolved. Some of the problematic cases were further resolved by combining MeV SIMS with Particle Induced X-Ray Emission (PIXE) technique which, contrary to surface-sensitive MeV SIMS, provides information from deeper layers. The cases left unsolved concern a lack of presence of unique characteristic X-rays for either the inkjet ink or ink from the other writing tool. The use of MeV SIMS requires access to an ion beam accelerator facility, which is not always available to the members of the forensic community.

In the present work, intersections of inks from several different writing tools (ballpoint pens, a fountain pen, and a stamp) that can be divided into two groups - optically distinguishable and optically indistinguishable, were studied using standard forensic optical techniques, which include microscopic and infrared luminescence techniques, and MeV SIMS. In MeV SIMS, molecules are desorbed from the uppermost layers of the sample thus ensuring the technique is surface sensitive. Obtained results were compared and discussed.

2. Materials and methods

2.1. Optical methods

Optical non-destructive techniques used for determination of deposition order at intersecting lines were performed using existing equipment for questioned document examination in the forensic science laboratory. Firstly, the intersections were examined microscopically to determine the nature of the intersecting material, particularly the type of the inks involved. Physical characteristics at the point of intersections were observed under Leica M205C stereo microscope from accompanying Video Spectral Comparator VSC6000/HS workstation (Foster + Freeman, UK), which has multi-angle LED illumination modules. Images were captured at magnification of 30x and were transferred to a computer with VSC6000HS imaging software. The intersections were examined with Olympus BX51 optical microscope from accompanying SENTERRA dispersive Raman spectrometer (Bruker, USA). Images were taken at magnification of 500x with objective 50x, NA = 0.90, wd:0.3 mm. The images represent an area of 150 × 62 μm^2. At least three different regions at the intersection were examined. The intersections were also examined using the spot infra-red light source with a VSC6000/HS workstation (Foster + Freeman, UK). It should be noted that by using a spot infra-red light source it was possible to determine the sequence of lines only if ink dyes have the property of infrared luminescence and hence the inks containing these dyes show infrared luminescence. This light source is a high-intensity source that is filtered to provide the user with a choice of excitation wavebands of light. In these cases, a 645 nm camera filter with a 485–500 nm green spot filter has been automatically selected. Samples were viewed and captured at 30x digital magnification in autofocus mode.

2.2. MeV TOF SIMS

MeV SIMS measurements were performed in a vacuum using a heavy ion microprobe available at the accelerator facility. The setup with the time-of-flight spectrometer described in detail in Tadic et al. [11]. was used. An 8 MeV Si^{4+} beam focused to approximately 5 × 5 μm^2 was employed to extract the secondary molecular ions. First, a mass spectrum of ink from each writing tool was measured by scanning smaller areas (100 × 100 μm^2) at the sample, far from the intersection region. After that, the intersection region of up to 1400 × 1400 μm^2 was scanned for imaging, and 2D molecular maps of intersections were created. The beam current in pulsed mode was about 0.2 fA. The sample holder was set at +5 kV to accelerate secondary molecular ions toward a TOF extractor. A multi-stop time-to-digital converter (TDC) data acquisition system in heavy-ion-deflection start-mode was used with 100 μs between the ion pulses of 4 ns duration.

2.3. Data analysis

An in-house built data acquisition system SPECTOR [12] was used to control all parameters and data acquisition during the experiment. Basic spectra inspection was carried out using mMass [13]. Principal component analysis (PCA) was employed on molecular images using MATLAB tool simsMVA [14] to enhance the contrast between different chemical compositions of each pixel. All images were binned by a factor of 2 (resulting in 64 × 64 pixels from the original 128 × 128 pixels), due to small number of counts per pixel. It

Table 1
Writing tools manufacturers and models.

Writing tool	Manufacturer	Model	Color of ink
Ballpoint pen	Pilot	unknown	blue
Ballpoint pen	BIC	unknown	black
Fountain pen	unknown	unknown	blue
Stamp	Trodat Printy	4912	blue
Ballpoint pen (BP1)	unknown	unknown	blue
Ballpoint pen(BP4)	unknown	unknown	blue
Ballpoint pen(BP2)	unknown	unknown	blue
Ballpoint pen(BP5)	unknown	unknown	blue

Table 2
List of studied combinations of inks from writing tools.

Pair no.	Combination
	Optically distinguishable
1	Fountain pen & BIC
2	Pilot & BIC
3	Trodat Printy & Pilot
4	Trodat Printy & Fountain pen
	Optically indistinguishable
5	BP1 & BP4
6	BP2 & BP5

is important to mention that some images were cropped due to scattering recorded on the edges of the scan area and appear in different sizes, but all maps contain the whole intersection area and a part of the surrounding region for context. MeV SIMS images were pre-processed using Poisson scaling (or in some cases square root scaling) with mean centering, and 2D Gaussian smoothing with varying standard deviation, as appropriate. Additionally, the score matrices were standardized for contrast enhancement (to have a mean of zero and standard deviation of one). K-means clustering was performed on the most informative principal components to produce the final image with a predetermined number of three clusters (inks from two writing tools and the paper), having the highest silhouette score. In the case of the last two combinations from Table 2, t-distributed stochastic neighbor embedding (t-SNE) algorithm was employed within Orange software [15] on normalized, binned, Poisson scaled and mean-centered data, and 2D Gaussian smoothed with SD = 0.8.

2.4. Sample preparation

The intersections were prepared in a way that the first line deposited was left to dry out on a blank white A4 paper for about 1 h before the deposition of the second line with ink from a different writing tool. In order to perform MeV SIMS analysis, it is necessary to cut out a small portion of the sample which includes the intersection as well as a bit of the surrounding individual ink. Then, the sample is put inside a vacuum chamber, where the analysis is conducted under a pressure of around 10–6 mbar. Hence, this is a destructive process and is meant to be carried out, if necessary, as a last resort. However, in the sense of chemical consistency of the sample, MeV SIMS is not considered destructive, since the achieved primary ion beam dose is well below the so-called static limit of 1012 ions/cm^2. The list of all writing tools from which inks are studied in the present work is given in Table 1. There are two different types of inks present. The first type involves oil-based inks such as ballpoint pens, which leave a trace at the surface of the paper. The second type are fountain pen and stamp, which are water-based and penetrate deeper into the paper. Pairs of samples have been produced containing ink from these writing tools; each pair is comprised of two combinations with respect to deposition order of inks from the writing tools present. Not all inks from different writing tools have been paired. Deposition order of each combination is emphasized in all figures. The studied pairs of samples are given in Table 2. The last two combinations were impossible to distinguish using optical techniques available at the forensic laboratory, hence these cases are deemed especially interesting.

3. Results and discussion

During image inspection, MeV SIMS, being a surface technique, should yield a discontinued trace from an ink deposited first, with a break located at the point of an intersection of inks from two writing tools. The trace from an ink deposited second should appear continuous. As shown in our previous work, this is the case if oil-based inks from ballpoint pens are used [9], while situation is not so simple if water-based inks are used [10].

Mass spectra of inks from all writing tools involved in the study are shown in Fig. 1. For simplicity, the spectra are ordered according to Table 1. The data were normalized to the total number of counts. The most discriminating features for each spectrum are pointed out. Some inks contain prominent peaks at high masses (most often dyes and pigments) which make their identification in images easier. On the other hand, fountain pen ink does not contain any heavy compounds and instead yields sodium with intensities quite different than the other ink in the sample, which is then used for separation. It should be noted that the success in separating inks in an image largely depends on the combination of inks in the sample (i.e. similarity of their compositions). On that note, the last two combinations from Table 2, which are indistinguishable by optical methods, involve two pairs of ballpoint pens having very similar, almost identical mass spectra. Here, all four ballpoint pens possess Basic Violet 3 and Basic Blue 7, common dye components present in most blue and black ballpoint pens.

Non-destructive optical techniques could be applied to determine the sequence of intersecting lines and are routinely employed in the area of forged document forensics. According to the ENFSI-EDEWG Methods [2], it should be noted that in real cases it is often useful to be able to replicate the intersection to be studied under a variety of conditions prior to the examination. If the writing tool involved in the creation of an intersection is available, or the type of the writing tool can be determined, it is desirable to recreate the intersections, or, if not available, with the same types of inks and pigments. Test intersections should represent both line sequences (line 1 on top of line 2; line 2 on top of line 1). Conditions in the test intersection should replicate conditions in the questioned document as much as possible. For instance, the quantity of ink should correspond to the ink quantity of the questioned lines, as well as the applied pressure. Also, the test intersection should be produced under different degrees of ink drying, as the time that the first ink was on the surface before the second one was applied will affect the appearance of the intersection. Test intersection should be made on a paper similar to or the same as the paper containing the intersection to be examined. The examination results obtained from these test intersections are compared to the ones from the unknown intersections. A variety of techniques can be employed to inspect an intersection and the choice of the technique will depend on the type of ink from writing tools involved in the intersection.

Caution has to be taken when one of the inks involved in the intersection is aqueous-based (e.g. fountain pen inks, fiber tip pen inks, highlighter inks, stamp inks, and some inkjet inks) because these inks tend to diffuse into the paper fibers (often no ink deposition occurs on the paper surface, depending on the paper quality), making determination of the sequence difficult and often extremely risky. Therefore, many examinations of intersecting lines result in an inconclusive opinion, particularly if the same ink type and color are involved. The examination of a line intersection

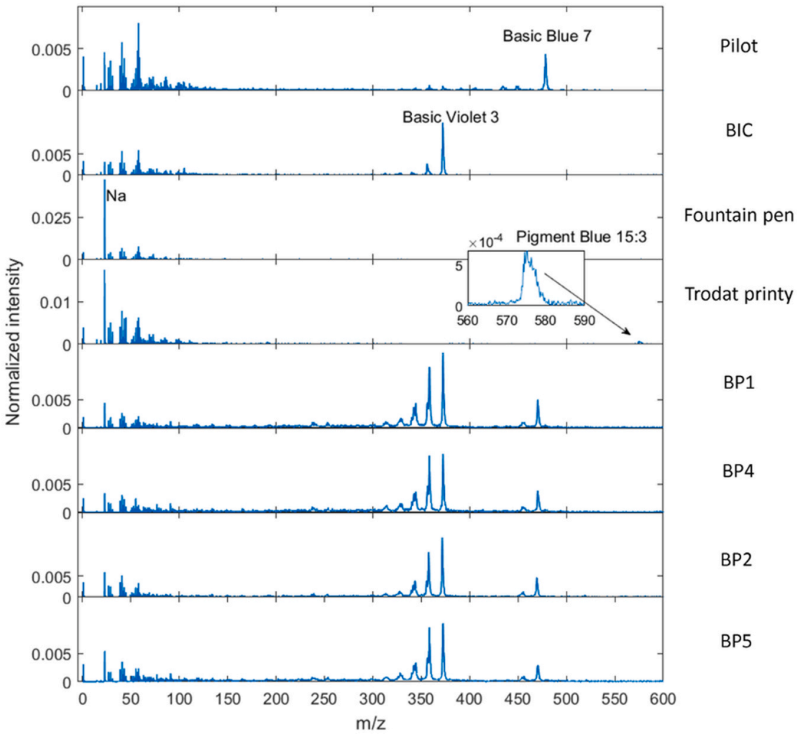

Fig. 1. MeV SIMS spectra of inks from individual writing tools ordered from top to bottom according to Table 1.

problem requires knowledge of inks and their behavior once on a paper surface. Determination of the type of ink is important so that the appropriate test intersections can be made. Thus, a forensic document expert possessing a great deal of practical experience plays a key role in successful determination of intersecting lines.

In the current study, IR luminescence proved to be especially efficient when one of the inks from two writing tools involved appeared IR-luminescent. Under the optical microscope, the ink colors are clearly different from the colors seen by the stereo microscope. For instance, in a blue vs. black system, the blue ink appears blue and the black ink appears reddish.

It should be noted that the expert examining optical images draws a subjective conclusion based on previous experience, as well. The images presented in this study may not be entirely representative of the actual images examined at the time of analysis directly on the instruments, i.e. some conclusions may not be as obvious as to the examiner during the analysis.

3.1. Intersections of optically distinguishable inks from different writing tools

3.1.1. Fountain pen and black ballpoint pen (BIC)

Both combinations of deposition order of fountain pen and ballpoint pen are shown in Fig. 2, along with the results from both the optical techniques and MeV SIMS. Based on the optical methods, it was found that the fountain pen was deposited above the ballpoint pen in Fig. 2a. Under the stereo microscope, it is visible that the fountain pen pulled the black ballpoint pen ink a bit downwards, leaving a trace of black ballpoint pen ink over the blue fountain pen ink line. Under the optical microscope, it can be seen that the blue color of the fountain pen ink predominates. Fountain pen ink spreading and diffusion phenomena [16,17] over the ballpoint pen ink line is visible under the spot infra-red light at the intersection area. This is due to the fact that fountain ink is liquid-based with high tendency for being absorbed into the paper fibers, while ballpoint pen ink is oil-based ink with a very small tendency for being absorbed. Hence, most of the ballpoint pen ink stays adherent to the paper surface. Consequently, when the fountain pen crosses over the ballpoint pen ink line, it immediately reacts in contact with ballpoint pen ink by spilling to the sides. In Fig. 2b the situation is reversed – under the spot infra-red light there is no visible reaction when the ballpoint pen crossed over the fountain ink line, and there is no difference in the ink line latitude. The black ballpoint pen ink line is over the blue fountain pen ink line and it is also visible from the colors under the optical microscope.

K-means clustering of MeV SIMS images produced a discontinued trace for a line deposited second with a fountain pen (Fig. 2a) when it should have been continuous. It also assigned an area just outside of the intersection region to the line deposited first with a ballpoint pen, indicating that diffusion of ballpoint pen ink occurred on neighboring paper fibers before the deposition of a fountain pen on top of it. This can also be seen from the stereo microscope image. The combination in Fig. 2b correctly showed deposition order. Nevertheless, there was not enough information to draw an absolute conclusion. Details on multivariate analysis of MeV SIMS images for fountain pen over BIC case can be seen in Figs. S-1 (PCA) and S-2 (k-means), and for BIC over fountain pen case in Figs. S-3 (PCA) and S-4 (k-means).

3.1.2. Blue ballpoint pen (Pilot) and black ballpoint pen (BIC)

Both combinations of deposition order of blue and black ballpoint pens are shown in Fig. 3, along with the results from both the optical techniques and MeV SIMS. Under the stereo microscope in this case in both combinations the deposition order cannot be determined, but under the optical microscope it is possible – in Fig. 3a the color of Pilot ballpoint pen ink predominates (blue effect) and in Fig. 3b the BIC ballpoint pen ink predominates at the intersection (reddish effect). Also, in Fig. 3a under the spot infra-red light it can

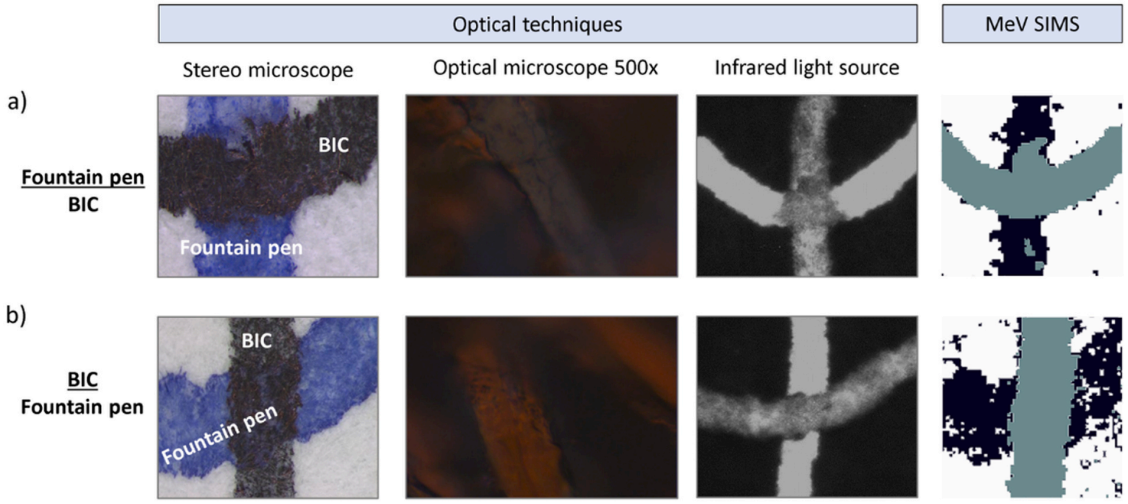

Fig. 2. Fountain pen and BIC. The first column shows microscopic images of samples. The next two columns show results from optical techniques. The last columns show results from MeV SIMS.

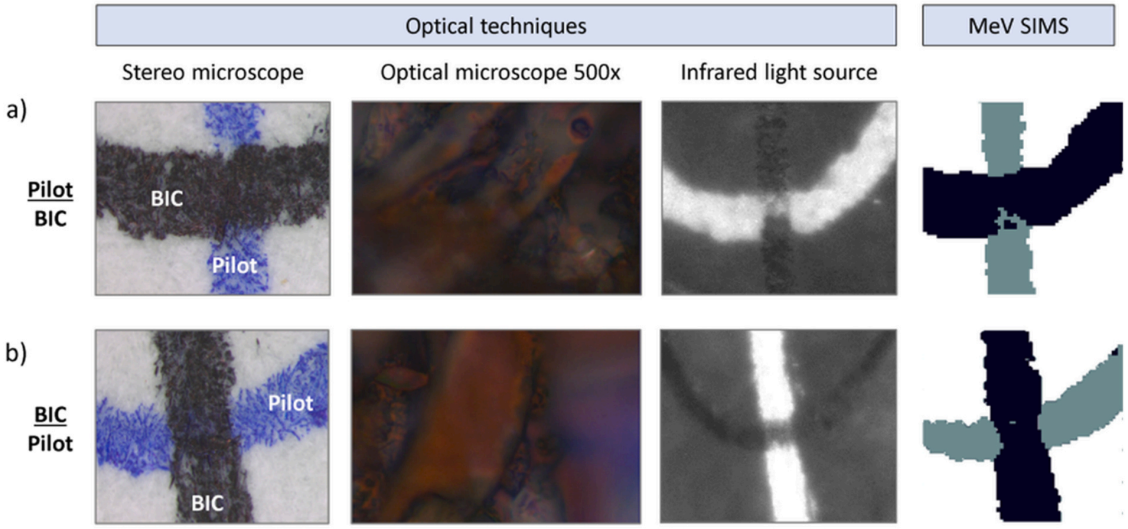

Fig. 3. Pilot and BIC. The first column shows microscopic images of samples. The next two columns show results from optical techniques. The last columns show results from MEV SIMS.

be seen that the Pilot ballpoint pen ink partially attenuates the IR luminescence of the BIC ballpoint pen ink line, indicated by the Pilot ballpoint pen ink line latitude difference before and after the intersection. Hence, it was concluded that the Pilot ballpoint pen ink is deposited above the BIC ballpoint pen ink. In Fig. 3b the situation is reversed and it was concluded that the BIC ballpoint pen ink is deposited over the Pilot ballpoint pen ink.

In MeV SIMS images, it looks as though the black ballpoint pen is deposited second in both combinations, which is not the case. K-means clustering produced a discontinued trace for a line deposited second with the blue ballpoint pen (Fig. 3a), although it does show a small area of Pilot ballpoint pen ink inside the intersection, also visible in the IR image. The combination in Fig. 3b correctly showed deposition order. Details on multivariate analysis of MeV SIMS images for BIC over Pilot case can be seen in Figs. S-5 (PCA) and S-6 (k-means), and for Pilot over BIC case in Figs. S-7 (PCA) and S-8 (k-means).

3.1.3. Stamp (Trodat Printy) and blue ballpoint pen (Pilot)

Both combinations of deposition order of Pilot and BIC are shown in Fig. 4, along with the results from both the optical techniques and MeV SIMS. In this case, it was not possible to determine deposition order of intersecting lines using optical methods. Under the optical microscope and especially under the spot infra-red light, it seems that the stamp ink is deposited over ballpoint pen ink (Fig. 4a), while in Fig. 4b it seems that ballpoint pen ink is deposited over stamp ink, which is incorrect.

MeV SIMS image correctly reveals deposition order for the case in Fig. 4a (Pilot trace is continuous, while stamp ink shows a break), but for the case in Fig. 4b, it shows the Pilot trace as deposited second, which is not the case. Details on multivariate analysis of MeV SIMS images for Pilot over Trodat Printy case can be seen in Figs. S-9 (PCA) and S-10 (k-means), and for Trodat Printy over Pilot case in Figs. S-11 (PCA) and S-12 (k-means).

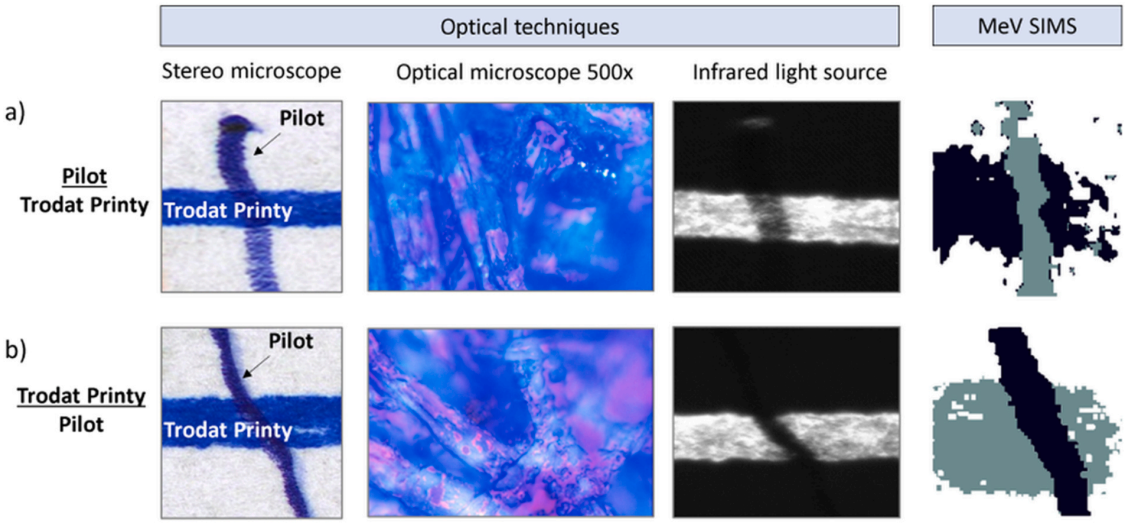

Fig. 4. Trodat Printy and Pilot. The first column shows microscopic images of samples. The next two columns show results from optical techniques. The last columns show results from MeV SIMS.

3.1.4. Fountain pen and stamp (Trodat Printy)

Both combinations of deposition order of fountain pen and stamp (Trodat Printy) are shown in Fig. 5, along with the results from both the optical techniques and MeV SIMS. The results of optical methods correctly showed deposition order in both combinations and they are very similar to the results from the case involving fountain pen and black ballpoint pen (BIC). In Fig. 5a, it is clearly visible that the fountain pen is deposited over the stamp – the blue color of the fountain pen ink predominates under the optical microscope, ink spreading and diffusion phenomena are evident under spot infra-red light. In Fig. 5b the situation is reversed, the stamp is deposited over the fountain pen – the blue color of the stamp predominates, the stamp ink attenuates the IR luminescence of fountain pen ink with no visible ink diffusion.

After k-means clustering, MeV SIMS images correctly revealed deposition order in both cases, that is, the line deposited first yields a trace with a break, and the line deposited second yields a continuous trace. Details on multivariate analysis of MeV SIMS images for fountain pen over Trodat Printy case can be seen in Figs. S-13 (PCA) and S-14 (k-means), and for Trodat Printy over fountain pen case in Figs. S-15 (PCA) and S-16 (k-means).

3.2. Intersections of optically indistinguishable inks from different writing tools

Four different blue ballpoint pens marked as BP1, BP2, BP4 and BP5 of unknown producer were obtained from the forensic laboratory, as it was not possible to conclude anything about the deposition order for combinations BP1 & BP4 and BP2 & BP5 using standard optical methods.

3.2.1. BP1 and BP4

Both combinations of deposition order of BP1 and BP4 are shown in Fig. 6, along with the results from both the optical techniques and

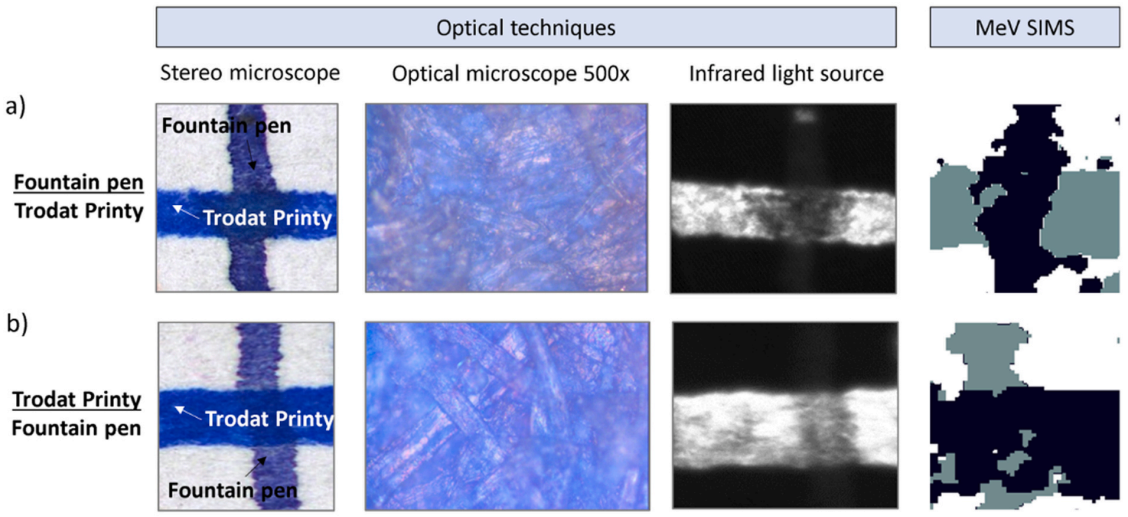

Fig. 5. Fountain pen and Trodat Printy. The first column shows microscopic images of samples. The middle columns show results from optical techniques. The last column shows results from MeV SIMS.

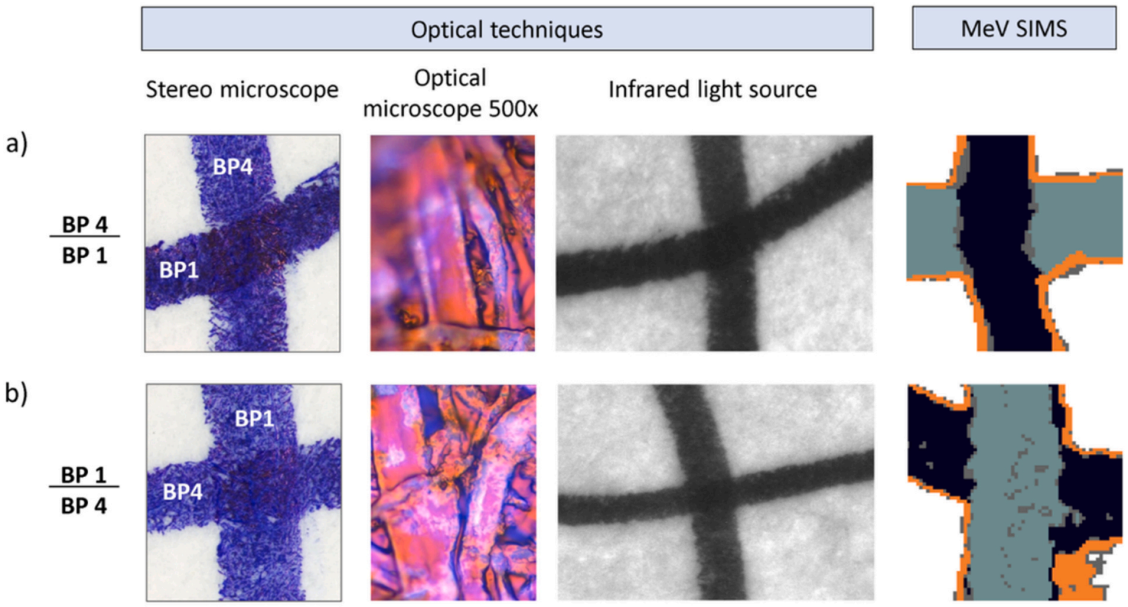

Fig. 6. BP1 and BP4. The first column shows microscopic images of samples. The middle columns show results from optical techniques. The last column shows the results from t-SNE performed on MeV SIMS dataset.

MeV SIMS. It is evident from Fig. 6 that neither optical nor IR images can distinguish these two very similar ballpoint pens. Also, it can be concluded from the mass spectra in Fig. 1 that ballpoint pens BP1 and BP4 are also chemically very similar and not easy to distinguish through mass peaks belonging to binders (in the lower mass region) or mass peaks belonging to pigments (in the high mass region). In such cases involving a combination of very similar pens, PCA analysis sometimes could not distinguish two pens and would characterize both deposited lines (including the intersection) as one type of pen. Therefore, t-SNE algorithm [18] was attempted to try to differentiate the two pens, on the assumption that the linearity constraint of PCA may limit its sensitivity to subtle differences throughout the sample. T-SNE uses non-linear embeddings of high-dimensional spectral information (input dataset) to form clusters in a single 2D map representation, preserving both local detail and the global data structure. Unlike PCA, which is only an orthogonal transformation of correlated variables to a set of uncorrelated variables while preserving global structure, t-SNE tries to preserve the local structure of the data by minimizing the Kullback-Leibler divergence between the two probability distributions (original, high-dimensional, and embedded, low-dimensional) with respect to the locations of the points in the map. The perplexity parameter for t-SNE was conditioned by combining two different perplexity values (50 and 500) to try to preserve both the local and global structure. Clustering of pixels represented in t-SNE space was performed using DBSCAN code, within Orange software, which is a density-based clustering algorithm. The optimal number of clusters was defined by selecting the neighborhood distance parameter to the value in the first "valley", as suggested by the authors of the algorithm [19]. Hence, the final MeV SIMS images are presented in the form of pixels colored according to clusters in the resulting t-SNE space. As can be seen from MeV SIMS results in Fig. 6, BP1 and BP4 are successfully distinguished and the deposition order is correctly identified in both combinations. Additionally, the DBSCAN clustering algorithm recognized trace edges (marked in orange) as a transient region of pixels between paper and pens in t-SNE space (Fig. 7). Details on t-SNE clustering results for the BP1 over BP4 case can be found in Fig. S-17.

Moreover, average pixel spectra of BP1 and BP4 from both samples (combinations) were derived from clusters in t-SNE space, shown in Fig. 8. Upon simple manual inspection, subtle differences in several peaks or groups of peaks are evident. For example, BP4 has a small unknown peak at *m/z* 123, which BP1 does not have. Also, Basic Violet 3 seems to be slightly lower in BP4 than in BP1. All perceived differences are not pronounced enough for a standard manual RGB representation of ink intersections. Yet, t-SNE takes all this information at once into account and is able to represent a clear picture of the intersection.

3.2.2. BP2 and BP5

Both combinations of deposition order of BP2 and BP5 are shown in Fig. 9, along with the results from both the optical techniques and MeV SIMS. As with the previous case, it is evident from Fig. 9 that neither optical nor IR images can distinguish these two very similar ballpoint pens. Mass spectra of BP2 and BP5 pens are also chemically very similar, as seen on Fig. 1. MeV SIMS analysis was done in the same way as in the previous case, resulting in correct determination of deposition order in case where BP5 was deposited on BP2 (Fig. 9a), but failing in the opposite combination (Fig. 9b). T-SNE algorithm recognized the intersection in Fig. 9b as different from both inks (marked as red). It should be noted that the deposition of BP5 ink was difficult due to dryness, even after minutes of restarting the ink flow, this being a potential cause of partially unsuccessful MeV SIMS results. A slight difference in deposition intensity between BP2 and BP5 can be observed on a stereo microscope in both combinations, as well. Details on t-SNE clustering results of MeV SIMS images for BP5 over BP2 case can be seen in Fig. S-18, and for BP2 over BP5 case in Fig. S-19.

A summary of results from all presented cases obtained from optical methods and MeV SIMS is given in Table 3. The first four rows show cases where optical methods are able to distinguish inks from

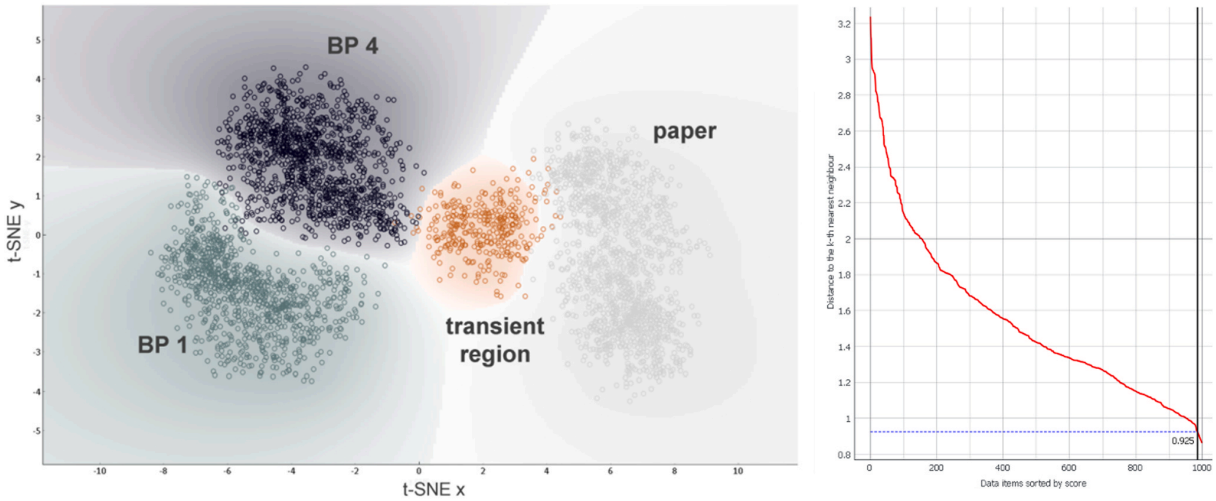

Fig. 7. BP4 over BP1 combination. Clustered pixels originating from BP1, BP4, paper, and a transient region, represented in t-SNE space (left). Optimal number of clusters is defined by DBSCAN, by selecting the neighborhood distance parameter to the value in the first "valley" (right).

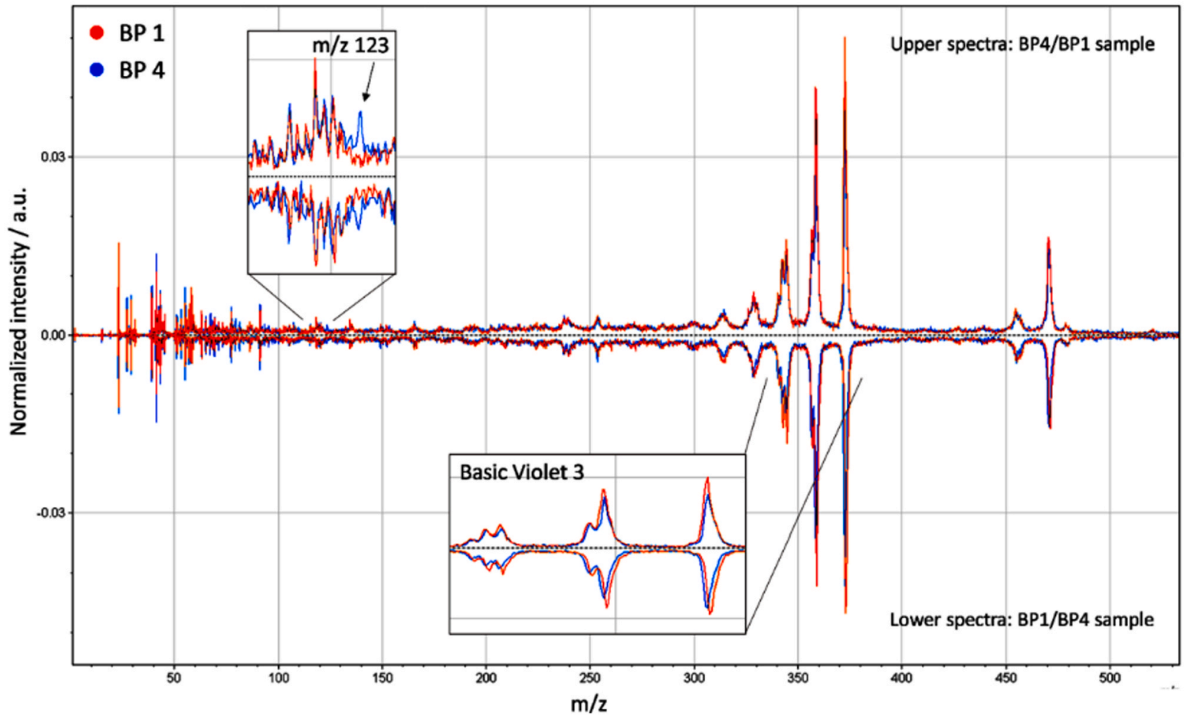

Fig. 8. Average pixel spectra derived from clusters in t-SNE space; BP1 (orange), BP4 (blue). Upper and lower spectra are acquired from BP4 over BP1 sample and BP1 over BP4 sample, respectively. (For interpretation of the references to color in this figure legend, the reader is referred to the web version of this article.)

writing tools in question, while the last two rows concern cases where no optical method available at the forensic laboratory can distinguish inks from the two writing tools. MeV SIMS in combination with PCA image processing slightly underperforms in comparison to optical methods for the first four pairs of intersecting lines but was definitely superior to optical methods for the last two pairs after employing t-SNE. For the last pair, even though MeV SIMS managed to correctly reveal the deposition order in one combination, the result was incorrect for the other combination, thus this case is generally unresolvable. Nevertheless, it is worth to mention that although BP2 and BP5 are optically identical, MeV SIMS still managed to identify independent parts of inks (away from the intersection) as of different origin.

As mentioned in the introduction, inks from water-based writing tools (in this case fountain pen and stamp) tend to be problematic for MeV SIMS when they are deposited on top of another ink, since

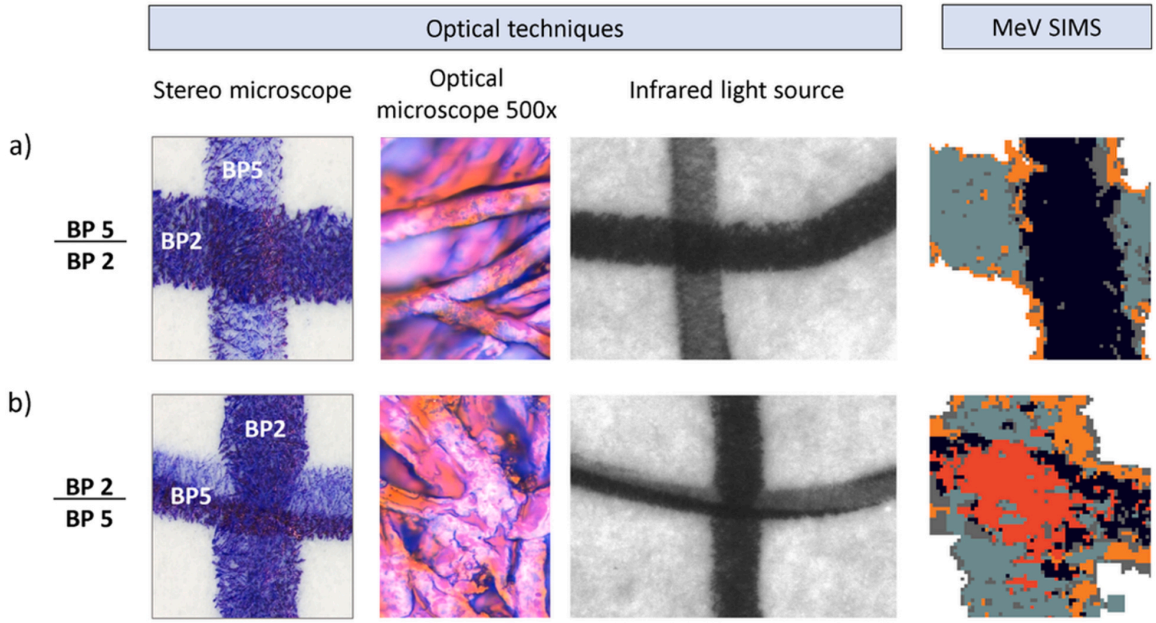

Fig. 9. BP2 and BP5. The first column shows microscopic images of samples. The middle columns show results from optical techniques. The last column shows the results from t-SNE performed on MeV SIMS dataset.

Table 3
A summary of all results obtained by optical methods and MeV SIMS.

Pair no.	Combination	Order	Optical methods		MeV SIMS	
			Success	Deposition order differentiable	Success	Deposition order differentiable
Optically distinguishable cases						
1	Fountain pen & BIC	Fountain pen /	✓*	✓*	×	×
		BIC / Fountain	✓*		✓	
2	Pilot & BIC	Pilot / BIC	✓	✓	×	×
		BIC / Pilot	✓		✓	
3	Trodat Printy & Pilot	Stamp / Pilot	×	×	×	×
		Pilot / stamp	×		✓	
4	Trodat Printy & Fountain pen	Stamp /	✓*	✓*	✓	✓
		Fountain pen /	✓*		✓	
Optically indistinguishable cases						
5	BP 1 & BP 4	BP 4 / BP 1	×	×	✓	✓
		BP 1 / BP 4	×		✓	
6	BP 2 & BP 5	BP 5 / BP 2	×	×	✓	×
		BP 2 / BP 5	×		×	

the deposition is often not as effective as on a paper. In the current study, PIXE that was very useful in some previous cases [10] could not reveal any additional information for unresolved cases because at least one writing tool per case did not yield any unique characteristic X-rays. On the other hand, results from optical methods marked with asterisk in Table 3 indicate that the conclusion is partially based on analyst's previous experience with fountain pen behavior under IR light source – while optical microscope shows

predominance of the ink above, there was no clear attenuation of IR luminescence.

4. Conclusions

In the present work, non-destructive optical techniques used in daily forensic work for solving problems related to intersecting lines on questioned documents used in the forensic laboratory were compared with a new and emerging IBA technique MeV SIMS available at the accelerator facility. Several cases of intersecting lines made by combining ballpoint pens, a stamp, and a fountain pen were prepared and examined. The intersecting lines were divided into those that are distinguishable by optical techniques used at the forensic laboratory and those that are not. Optical techniques slightly outperform MeV SIMS in determining the deposition order for intersections of optically distinguishable inks from different writing tools where both oil-based and water-based inks were used. MeV SIMS proved to be more efficient for oil-based inks while difficulties were encountered with water-based ones, similar to optical methods. However, in some cases, the experience of a forensic analyst proved to be important in decision making. The situation was quite different for two combinations of intersecting lines from four very similar blue ballpoint pens which were completely indistinguishable by optical methods. Although their mass spectra were also very similar and had negligible differences, when combined with advanced non-linear multivariate analysis tools such as t-SNE, which are more objective and independent of the analyst, these differences were sufficient to correctly determine the deposition order in one case and partially in the other. Therefore, MeV SIMS outperforms standard forensic optical techniques in some of these cases. However, although this preliminary study shows certain positive results, due to a low number of samples, reproducibility has not yet been established and should be further investigated.

It seems reasonable to conclude that in some cases where standard forensic optical methods fail, MeV SIMS could play an important role and be a method of choice in revealing the deposition order of two very similar ballpoint pens which are optically indistinguishable, by using multivariate analysis tools to extract critical latent information from the obtained hyperspectral molecular data. No matter the ability to determine the deposition order, if the inks involved can be differentiated using MeV SIMS (e.g. BP2 and BP5 pair), such valuable information can be exploited in other cases of official document forgery, such as alteration or addition of letters and numbers, where no overlapping traces are present or relevant.

A logical future direction would be data fusion of several complementary techniques, both conventional and unconventional in forensic sciences, which could undoubtedly strengthen the evidential value in forensics of forged documents.

CRediT authorship contribution statement

Marko Barac: Conceptualization, Methodology, Software, Formal analysis, Investigation, Writing – original draft, Writing – review & editing, Visualization. **Andrijana Filko:** Conceptualization, Formal analysis, Investigation, Resources, Writing – original draft. **Zdravko Siketić:** Investigation. **Marko Brajković:** Investigation. **Andrea Ledić:** Conceptualization, Supervision. **Iva Bogdanović Radović:** Conceptualization, Supervision, Project Administration, Writing – original draft, Writing – review & editing.

Acknowledgments

I.B.R. and Z.S. acknowledge support by the European Union's Horizon 2020 Project RADIATE under the Grant Agreement 824096, COST Action CA16101 MULTi-modal imaging of FOREnsic SciEnce Evidence (MULTI-FORESEE), and IAEA CRP F11021: "Enhancing Nuclear Analytical Techniques to meet the needs of forensic science". M. Brajković acknowledges support by the Croatian Science Foundation Project "Young Researchers' Career Development Project – Training of Doctoral Students" financed by Croatia and co-financed by the European Union, Operational Program "Efficient Human Resources 2014–2020".

Appendix A. Supporting information

Supplementary data associated with this article can be found in the online version at doi:10.1016/j.forsciint.2021.111136.

References

[1] L.R. e Brito, A.R. Martins, A. Braz, A.B. Chaves, J.W. Braga, M.F. Pimentel, Critical review and trends in forensic investigations of crossing ink lines, TrAC Trends Anal. Chem. 94 (2017) 54–69.
[2] EDEWG, Examination of Intersecting Lines, ENFSI, September 2004.
[3] K. Saini, R. Kaur, N.C. Sood, Determining the sequence of intersecting gel pen and laser printed strokes—a comparative study, Sci. Justice 49 (4) (2009) 286–291.
[4] A. He, D. Karpuzov, S. Xu, Ink identification by time-of-flight secondary ion mass spectroscopy, Surf. Interface Anal. 38 (2006) 854–858.
[5] J. Lee, S.H. Kim, Y.-J. Cho, Y.S. Nam, K.-B. Lee, Y. Lee, Characterization and sequence determination of pen inks, red sealing inks, and laser toners by TOF-SIMS and ATR FTIR, Surf. Interface Anal. 46 (2014) 317–321.
[6] J. Lee, Y.S. Nam, J. Min, K.-B. Lee, Y. Lee, TOF-SIMS analysis of red color inks of writing and printing tools on questioned documents, J. Forensic Sci. 61 (2016) 815–822.
[7] R.E. Goacher, L.G. DiFonzo, K.C. Lesko, Challenges determining the correct deposition order of different intersecting black inks by time-of-flight Secondary Ion Mass Spectrometry, Anal. Chem. 89 (2016) 759–766.
[8] M.J. Bailey, B.N. Jones, S. Hinder, J. Watts, S. Bleay, R.P. Webb, Depth profiling of fingerprint and ink signals by SIMS and MeV SIMS, Nucl. Instrum. Methods Phys. Res. Sect. B: Beam Interact. Mater. At. 268 (2010) 1929–1932.
[9] M.C. Malloy, I. Bogdanović Radović, Z. Siketić, M. Jakšić, Determination of deposition order of blue ballpoint pen lines by MeV Secondary Ion Mass Spectrometry, Forensic Chem. 7 (2018) 75–80.
[10] K.L. Moore, M. Barac, M. Brajković, M.J. Bailey, Z. Siketić, I. Bogdanović Radović, Determination of deposition order of toners, inkjet inks, and blue ballpoint pen combining MeV-Secondary Ion Mass Spectrometry and Particle Induced X-ray Emission, Anal. Chem. 91 (2019) 12997–13005.
[11] T. Tadić, I. Bogdanović Radović, Z. Siketić, D.D. Cosic, N. Skukan, M. Jakšić, J. Matsuo, Development of a TOF SIMS setup at the Zagreb heavy ion microbeam facility, Nucl. Instrum. Methods Phys. Res. Sect. B: Beam Interact. Mater. At. 332 (2014) 234–237.
[12] D. Cosic, M. Bogovac, M. Jakšić, Data acquisition and control system for an evolving nuclear microprobe, Nucl. Instrum. Methods Phys. Res. Sect. B: Beam Interact. Mater. At. 451 (2019) 122–126.
[13] M. Strohalm, M. Hassman, B. Košata, M. Kodíček, mMass data miner: an open source alternative for mass spectrometric data analysis, Rapid Commun. Mass Spectrom. 22 (2008) 905–908.
[14] G.F. Trindade, M.-L. Abel, J.F. Watts, simsMVA: a tool for multivariate analysis of ToF-SIMS datasets, Chemom. Intell. Lab. Syst. 182 (2018) 180–187.
[15] J. Demsar, T. Curk, A. Erjavec, C. Gorup, T. Hocevar, M. Milutinovic, M. Mozina, M. Toplak, P.M. Toplak M., A. Staric, M. Stajdohar, L. Umek, L. Zagar, Z.J. Zitnik M., Z. B, Orange: Data Mining Toolbox in Python, J. Mach. Learn. Res. 14 (2013), pp. 2349–2353.
[16] R. Williamson, D. Djidrovska, A. Ledic, S. Brzica, V. Antikj, R. Hofer, J. Almirall, Characterization and identification of luminescent components in inks using various analytical techniques for the study of crossed-line intersections, Forensic Chem. 3 (2017) 28–35.
[17] INTERPOL, AIEED, Physical-Chemical Study of Crossed Line Intersection, Lyon, 2016, p. 92.
[18] L. van der Maaten, G. Hinton, Visualizing data using t-SNE, J. Mach. Learn. Res. 9 (2008) 2579–2605.
[19] M. Ester, H.-P. Kriegel, J. Sander, X. Xu, A. Density-Based Algorithm for Discovering Clusters in Large Spatial Databases with Noise, in: Proc. of 2nd International Conference on Knowledge Discovery and Data Mining, AAAI Press, 1996, pp. 226–231.

Supplementary Material

Comparison of optical techniques and MeV SIMS in determining deposition order between optically distinguishable and indistinguishable writing tools

Table of Contents

Page	Title	Sample	Analysis
S-2	Figure S-1	fountain pen over BIC	PCA
S-2	Figure S-2	fountain pen over BIC	k-means
S-3	Figure S-3	BIC over fountain pen	PCA
S-3	Figure S-4	BIC over fountain pen	k-means
S-4	Figure S-5	BIC over Pilot	PCA
S-4	Figure S-6	BIC over Pilot	k-means
S-5	Figure S-7	Pilot over BIC	PCA
S-5	Figure S-8	Pilot over BIC	k-means
S-6	Figure S-9	Pilot over Trodat Printy	PCA
S-6	Figure S-10	Pilot over Trodat Printy	k-means
S-7	Figure S-11	Trodat Printy over Pilot	PCA
S-7	Figure S-12	Trodat Printy over Pilot	k-means
S-8	Figure S-13	Fountain pen over Trodat Printy	PCA
S-8	Figure S-14	Fountain pen over Trodat Printy	k-means
S-9	Figure S-15	Trodat Printy over fountain pen	PCA
S-9	Figure S-16	Trodat Printy over fountain pen	k-means
S-10	Figure S-17	BP1 over BP4	t-SNE
S-10	Figure S-18	BP5 over BP2	t-SNE
S-11	Figure S-19	BP2 over BP5	t-SNE

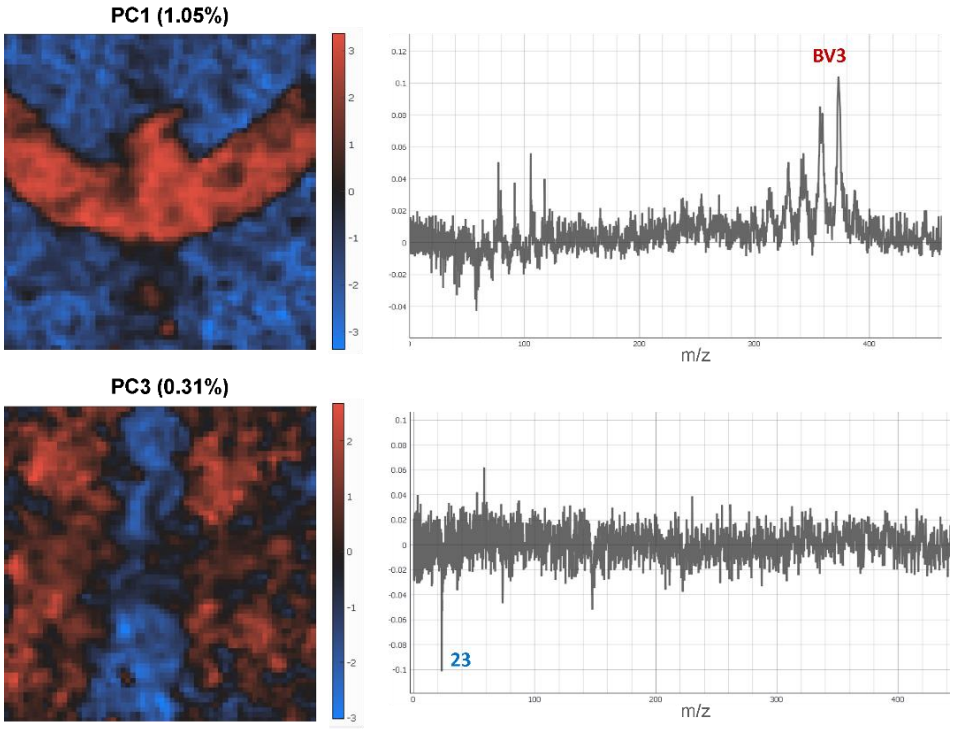

*Figure S-1. PCA results for **fountain pen over BIC** combination. Scores (left) of the ink-descriptive principal components (PC1 and PC3), and their corresponding loading plots (right) with ink-determining species highlighted. Raw data was first normalized to total counts and binned by a factor of 2, then pre-processed by square root scaling + mean centering. A Gaussian smoothing filter with SD=0.8 was applied. All calculated principal components were autoscaled.This sample had a low number of counts collected.*

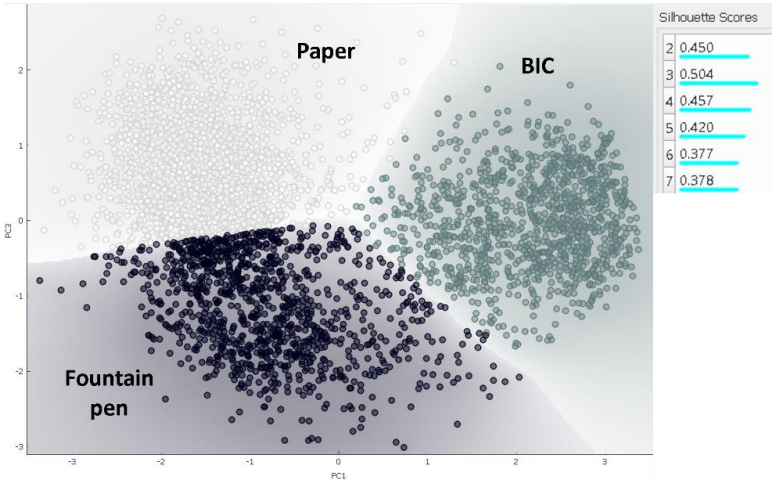

Figure S-2. K-means clustering on pixels represented in autoscaled PC1-PC3 score plot. Optimal number of clusters (three) is determined from the highest silhouette score, corresponding to BIC ink, fountain pen ink and paper.

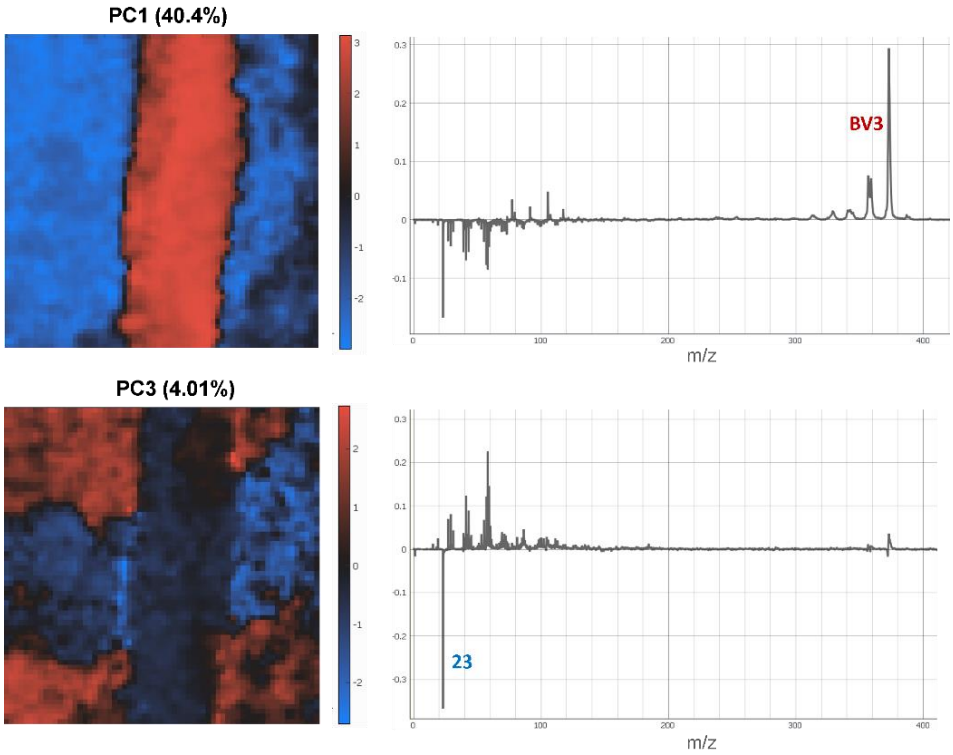

*Figure S-3. PCA results for **BIC over fountain pen** combination. Scores (left) of the ink-descriptive principal components (PC1 and PC3), and their corresponding loading plots (right) with ink-determining species highlighted. Raw data was first normalized to total counts and binned by a factor of 2, then pre-processed by square root scaling + mean centering. A Gaussian smoothing filter with SD=0.8 was applied. All calculated principal components were autoscaled.*

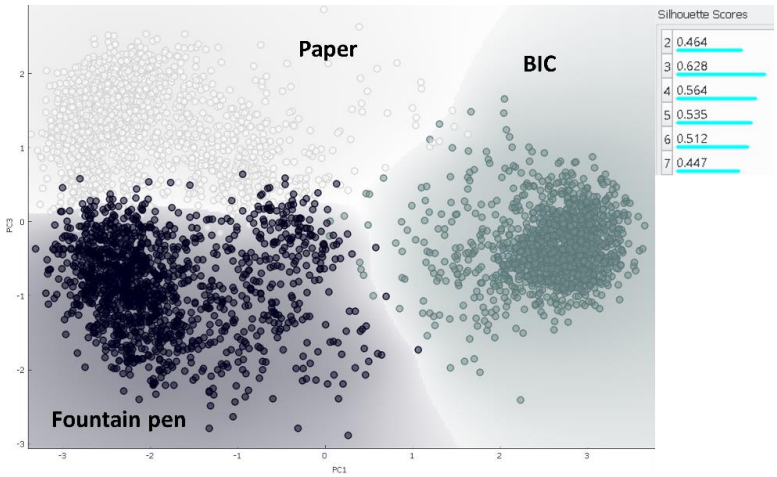

Figure S-4. K-means clustering on pixels represented in PC1-PC3 score plot. Optimal number of clusters (three) is determined from the highest silhouette score, corresponding to BIC ink, fountain pen ink and paper.

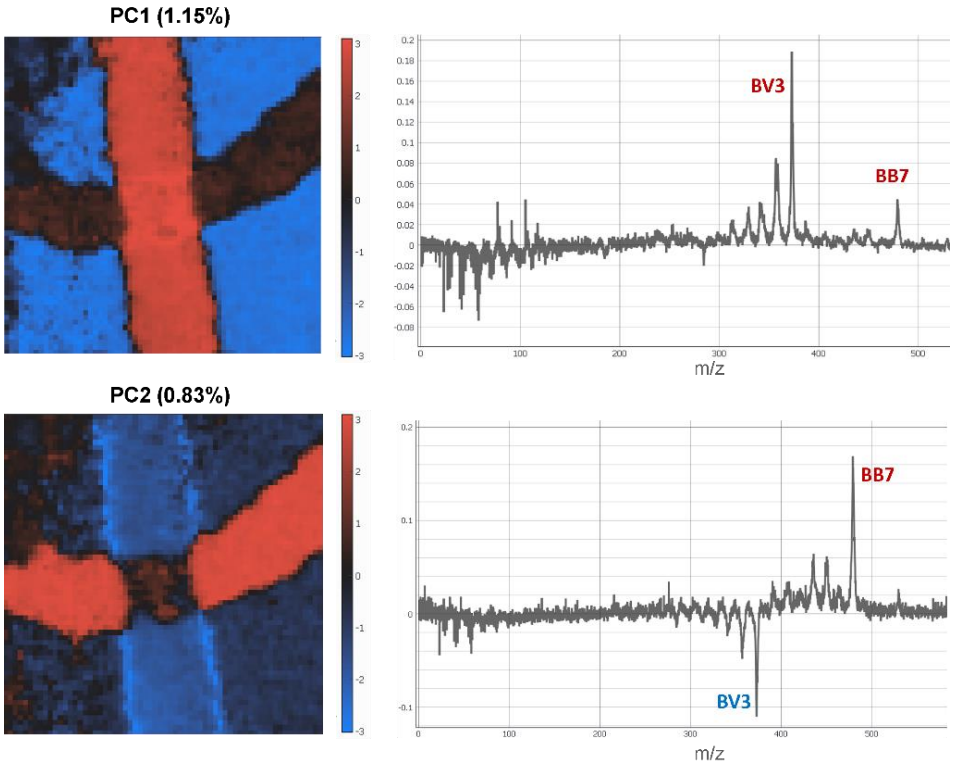

*Figure S-5. PCA results for **BIC over Pilot** combination. Scores (left) of the ink-descriptive principal components (PC1 and PC2), and their corresponding loading plots (right) with ink-determining species highlighted. Raw data was first normalized to total counts and binned by a factor of 2, then pre-processed by Poisson scaling + mean centering. A Gaussian smoothing filter with SD=0.6 was applied. All calculated principal components were autoscaled.*

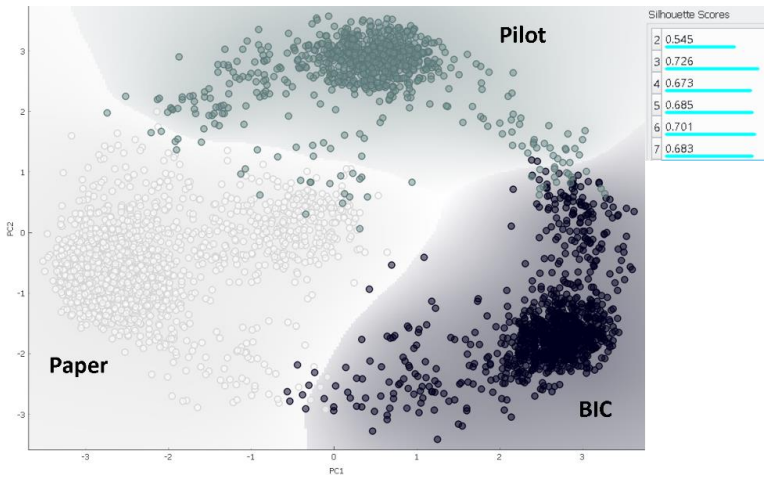

Figure S-6. K-means clustering on pixels represented in PC1-PC2 score plot. Optimal number of clusters (three) is determined from the highest silhouette score, corresponding to BIC ink, Pilot ink and paper. Higher number of clusters separates the paper cluster into multiple regions, probably due to morphology.

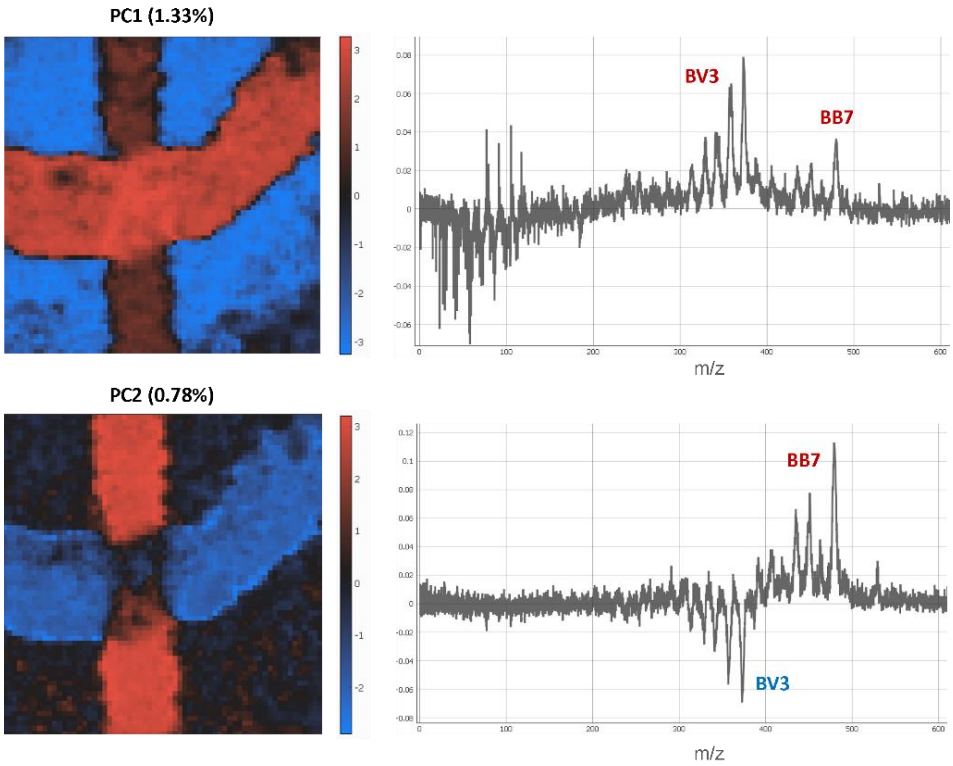

*Figure S-7. PCA results for **Pilot over BIC** combination. Scores (left) of the ink-descriptive principal components (PC1 and PC2), and their corresponding loading plots (right) with ink-determining species highlighted. Raw data was first normalized to total counts and binned by a factor of 2, then pre-processed by Poisson scaling + mean centering. A Gaussian smoothing filter with SD=0.6 was applied. All calculated principal components were autoscaled.*

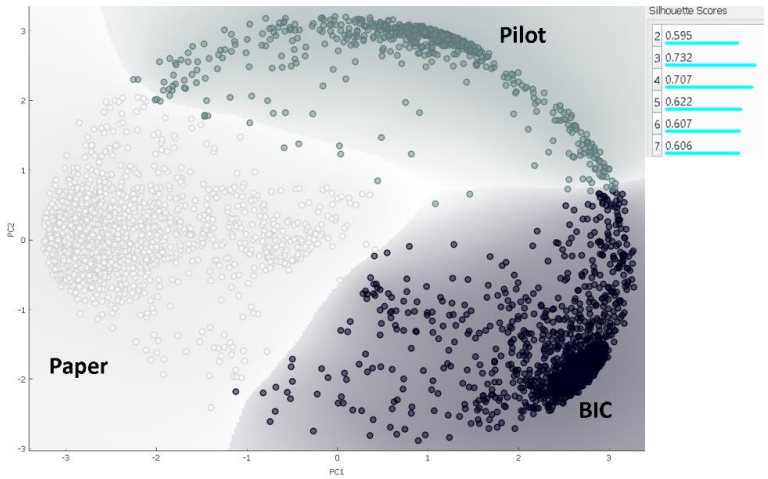

Figure S-8. K-means clustering on pixels represented in PC1-PC2 score plot. Optimal number of clusters (three) is determined from the highest silhouette score, corresponding to BIC ink, Pilot ink and paper. The second highest silhouette score (4 clusters) separates the paper cluster into two regions, probably due to morphology.

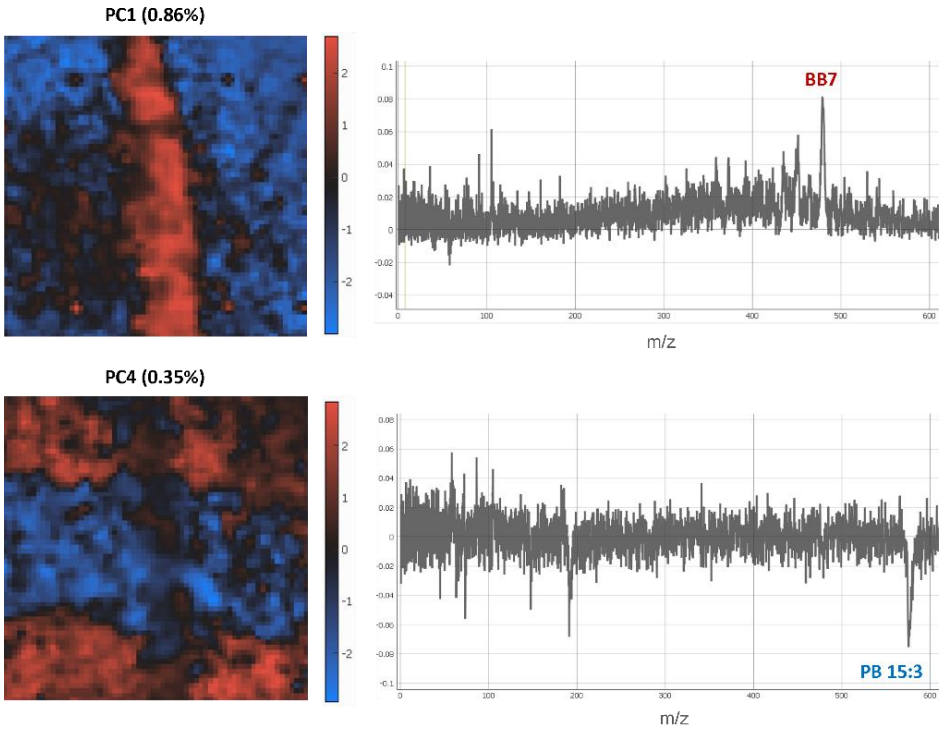

*Figure S-9. PCA results for **Pilot over Trodat Printy** combination. Scores (left) of the ink-descriptive principal components (PC1 and PC4), and their corresponding loading plots (right) with ink-determining species highlighted. Raw data was first normalized to total counts and binned by a factor of 2, then pre-processed by square root scaling + mean centering. A Gaussian smoothing filter with SD=0.8 was applied. All calculated principal components were autoscaled. This sample had a low number of counts collected.*

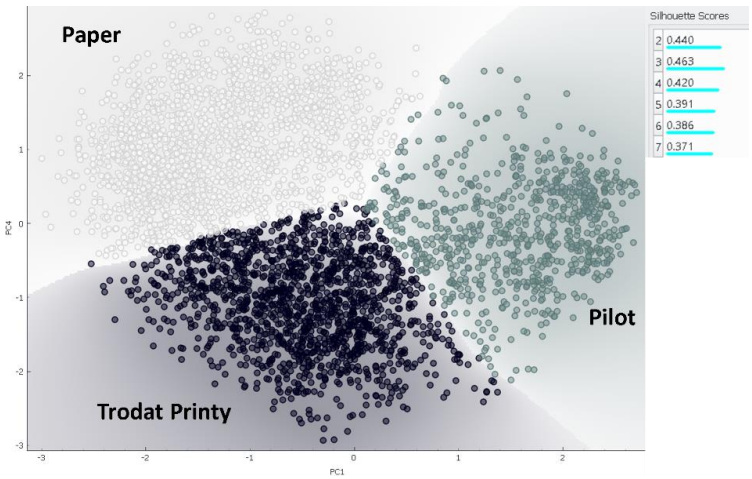

Figure S-10. K-means clustering on pixels represented in PC1-PC4 score plot. Optimal number of clusters (three) is determined from the highest silhouette score, corresponding to Pilot ink, Trodat Printy ink and paper.

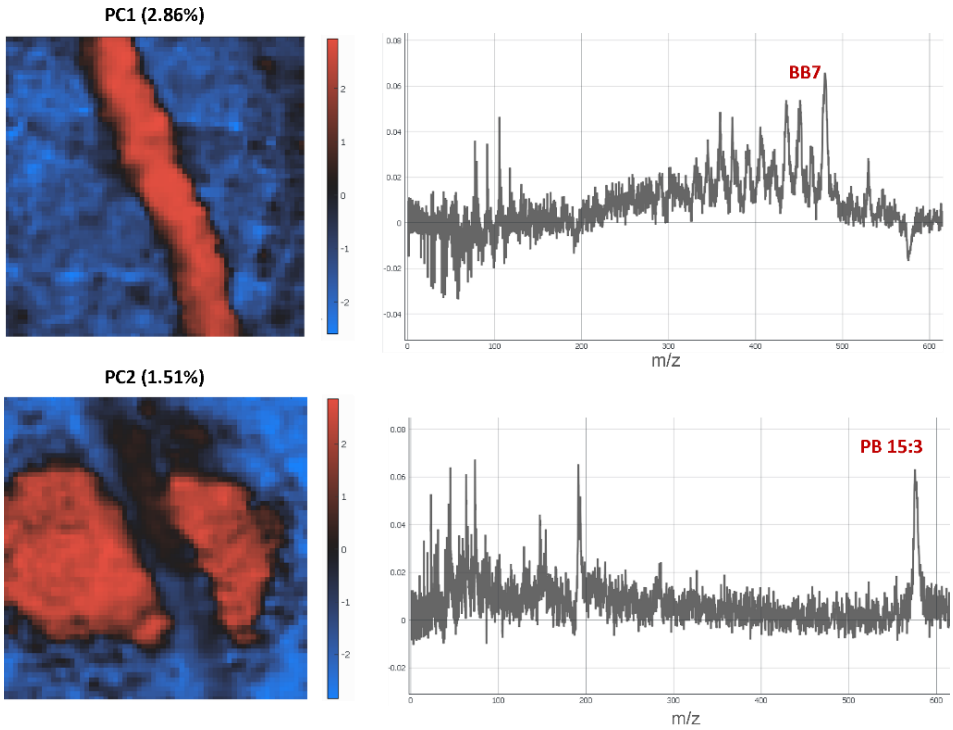

*Figure S-11. PCA results for **Trodat Printy over Pilot** combination. Scores (left) of the ink-descriptive principal components (PC1 and PC2), and their corresponding loading plots (right) with ink-determining species highlighted. Raw data was first normalized to total counts and binned by a factor of 2, then pre-processed by square root scaling + mean centering. A Gaussian smoothing filter with SD=0.8 was applied. All calculated principal components were autoscaled.*

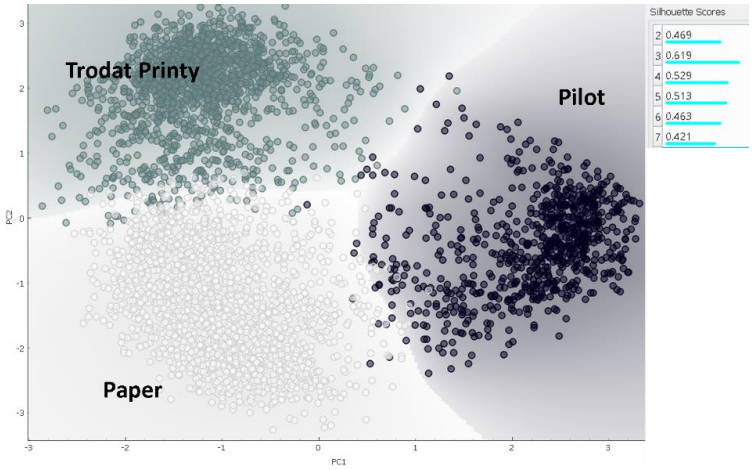

Figure S-12. K-means clustering on pixels represented in PC1-PC2 score plot. Optimal number of clusters (three) is determined from the highest silhouette score, corresponding to Pilot ink, Trodat Printy ink and paper.

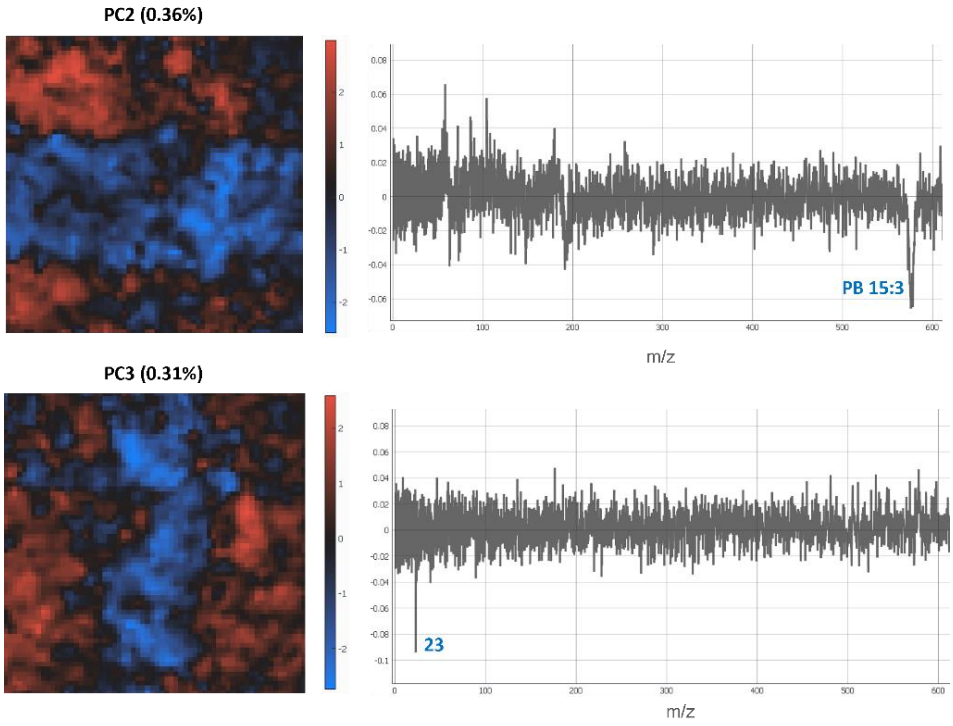

*Figure S-13. PCA results for **fountain pen over Trodat Printy** combination. Scores (left) of the ink-descriptive principal components (PC2 and PC3), and their corresponding loading plots (right) with ink-determining species highlighted. Raw data was first normalized to total counts and binned by a factor of 2, then pre-processed by square root scaling + mean centering. A Gaussian smoothing filter with SD=0.8 was applied. All calculated principal components were autoscaled. This sample had a low number of counts collected.*

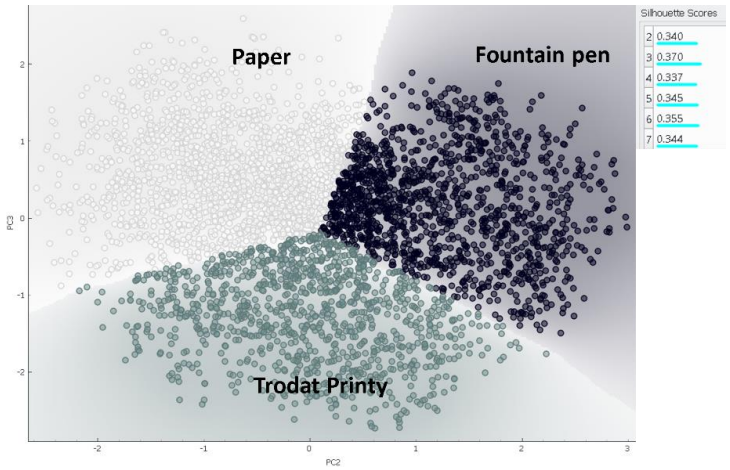

Figure S-14. K-means clustering on pixels represented in PC2-PC3 score plot. Optimal number of clusters (three) is determined from the highest silhouette score, corresponding to fountain pen ink, Trodat Printy ink and paper.

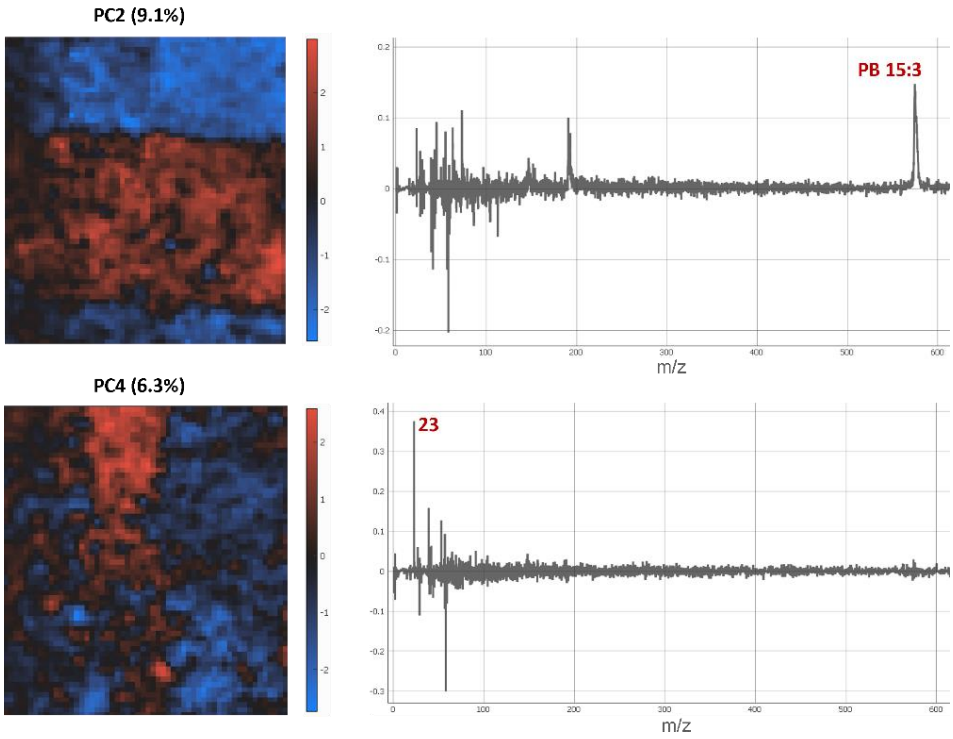

*Figure S-15. PCA results for **Trodat Printy over fountain pen** combination. Scores (left) of the ink-descriptive principal components (PC2 and PC4), and their corresponding loading plots (right) with ink-determining species highlighted. Raw data was first normalized to total counts and binned by a factor of 2, then pre-processed by square root scaling + mean centering. A Gaussian smoothing filter with SD=0.9 was applied. All calculated principal components were autoscaled. This sample had a low number of counts collected.*

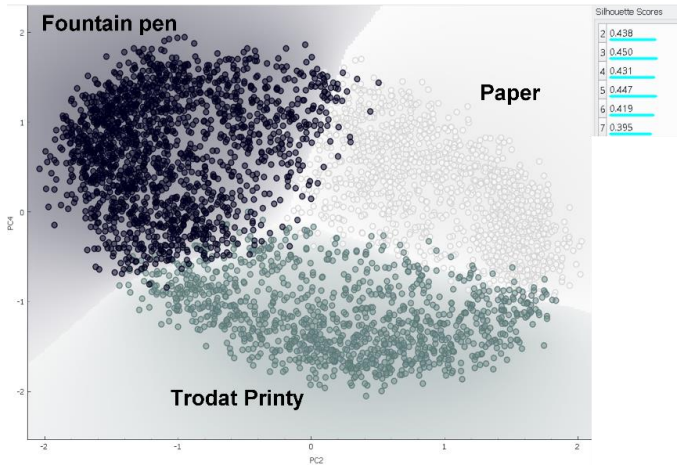

Figure S-16. K-means clustering on pixels represented in PC2-PC4 score plot. Optimal number of clusters (three) is determined from the highest silhouette score, corresponding to fountain pen ink, Trodat Printy ink and paper.

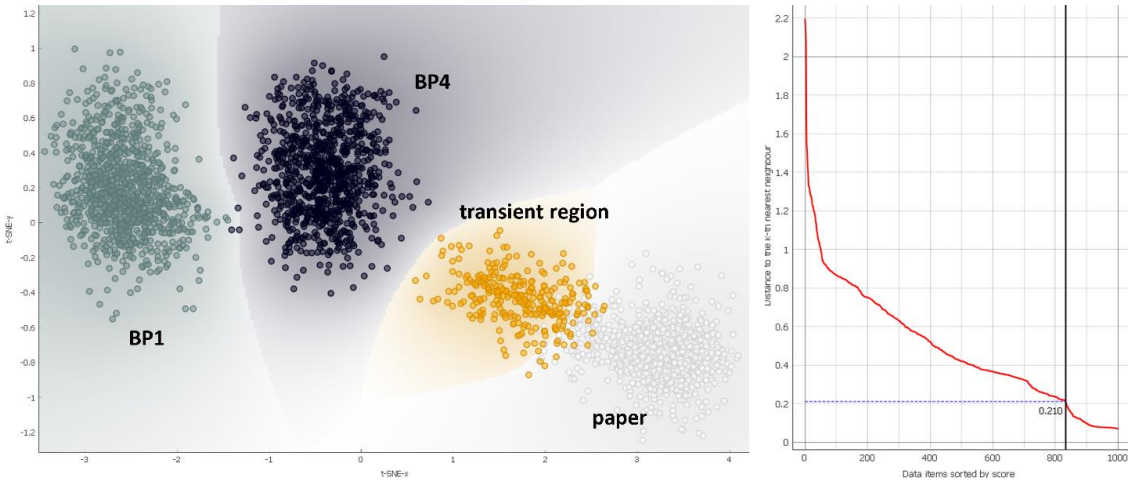

*Figure S-17. T-SNE results for **BP1 over BP4 combination**. Clustered pixels originating from BP1, BP4, paper, and a transient region, represented in t-SNE space (left). Perplexity parameter for t-SNE was conditioned to preserve global structure, combining two different perplexity values (50 and 500) to try preserve both the local and global structure. Clustering was performed with DBSCAN code within Orange software (density based clustering). Optimal number of clusters is defined by selecting the neighborhood distance parameter to the value in the first "valley" (right).*

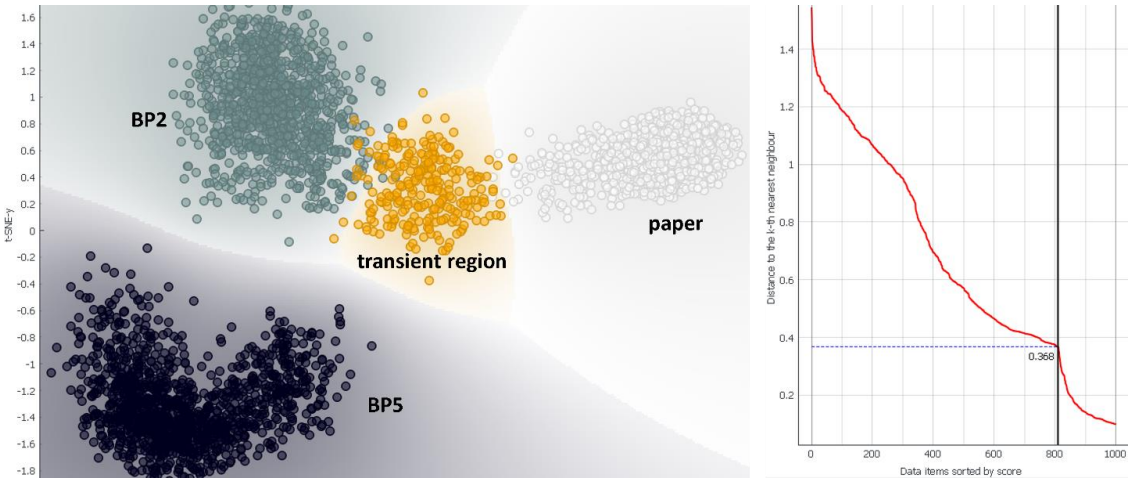

*Figure S-18. T-SNE results for **BP5 over BP2 combination**. Clustered pixels originating from BP5, BP2, paper, and a transient region, represented in t-SNE space (left). Perplexity parameter for t-SNE was conditioned to preserve global structure, combining two different perplexity values (50 and 500) to try preserve both the local and global structure. Clustering was performed with DBSCAN code within Orange software (density based clustering). Optimal number of clusters is defined by selecting the neighborhood distance parameter to the value in the first "valley" (right).*

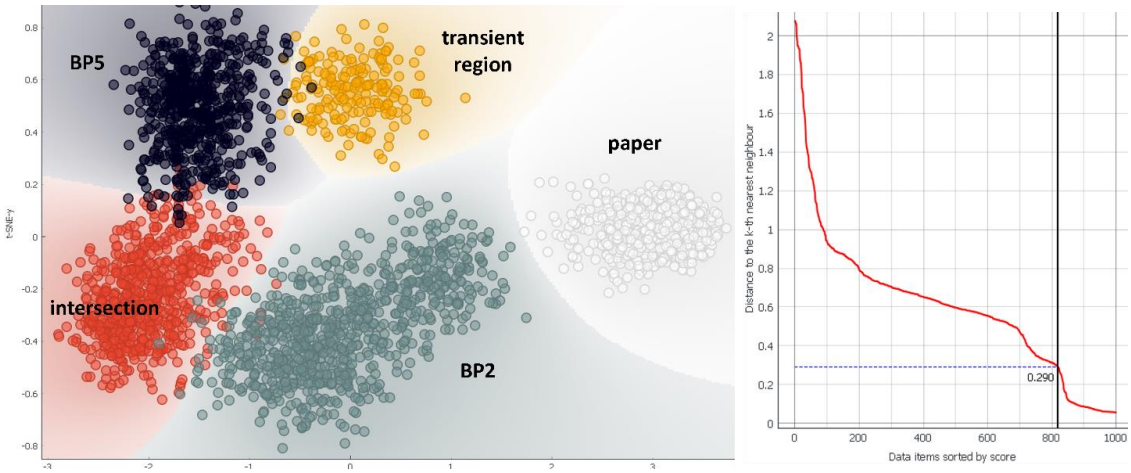

*Figure S-19. T-SNE results for **BP2 over BP5 combination**. Clustered pixels originating from BP2, BP5, paper, transient region, and intersectionregion is represented in t-SNE space (left). Perplexity parameter for t-SNE was conditioned to preserve global structure, combining two different perplexity values (50 and 500) to try preserve both the local and global structure. Clustering was performed with DBSCAN code within Orange software (density based clustering). Optimal number of clusters is defined by selecting the neighborhood distance parameter to the value in the first "valley" (right).*

Chapter 4

Conclusions

The development of MeV ToF SIMS technique is still progressing in the accelerator facilities worldwide, and new fields of application are constantly being found suitable due to the method's excellent sensitivity to biomolecules, lateral resolution in imaging, and surface sensitivity. This thesis has focused on the advancement of the technique in two aspects: fundamental research in the low energy primary ion beam mode, and application in the standard MeV energy mode, where the emphasis is put on the benefit of multivariate analysis methods in MeV SIMS imaging.

The low energy primary ion beam mode in MeV SIMS implies greater contribution of nuclear stopping and lesser contribution of electronic stopping in sputtering of ions, which translates to greater sensitivity to inorganic ions and lesser sensitivity to organic molecular ions. On the basis of this principle, MeV SIMS has the potential to be used for the analysis of inorganic samples, in addition to standardly analyzed organic samples. However, since no sputtering theory exists so far which can fully describe the sputtering process including both electronic and nuclear energy loss, it is hard to predict secondary ion yields of any given organic or inorganic species when operating with primary ion beam energies at which equal occurrence of nuclear and electronic stopping is expected. Furthermore, the secondary ion yield trends are drastically different between species and there seems to be no single parameter to describe them. This complicates the choice of a unique, most optimal primary ion beam for the analysis of a hybrid system, which then largely depends on the characteristics of a given sample. Nevertheless, the work presented here established that MeV SIMS is indeed capable of detecting ions from numerous inorganic targets, albeit with significant differences in sensitivity. Moreover, secondary ions from an organic target were still efficiently detected using low primary ion beam energies, clearly with reduced yields and increased fragmentation. The study culminated in imaging of a hybrid organic/inorganic sample and clearly demonstrated a diminishing contrast between organic and inorganic region when using low primary ion energies instead of standard MeV energies, while preserving the prominence of both organic and inorganic secondary ion yields. The work continued in efforts to further investigate the possibilities of this mode in terms of depth profiling of inorganic materials. The choice of the species comprising the target was governed by a sufficient and similar sensitivity in the low energy mode determined in the previous study. The LE MeV SIMS depth profile of a Cr-ITO dual-layer sample demonstrated solid chemical sensitivity to inorganic secondary ions, as expected, as well as satisfactory depth resolution comparable to keV SIMS using the same type of etching beam. The observed limitations in the profile seemed to be a consequence of the sputtering rather than the analysis conditions, which is encouraging. The most significant revelation was a sign of majorly reduced matrix effect on Cr^+ secondary ion at the partially oxidized locations in Cr layer, compared to keV SIMS. It is well known that

matrix effects present a considerable issue in conventional SIMS quantification, hence this observation could bring out the advantage of using LE MeV SIMS. Several studies have demonstrated the dependence of matrix effects on the chemistry of the primary ion beam. Considering that fact, with LE MeV SIMS as an accelerator-based technique, it is much more convenient to tailor and optimize the beam to specific needs, thus possibly reducing matrix effects. This study demonstrated that depth profiling of inorganic materials with MeV SIMS using lower energy primary ion beams is indeed feasible, using a relatively low-cost sputtering source for etching.

Apart from the fundamental research in the non-standard primary ion energy region, MeV SIMS technique proved promising in the analysis of questioned documents while operating in the standard energy region. Due to the method being surface-sensitive and chemically non-destructive, the forensic analysis of deposition order of intersecting ink lines appears highly suitable. However, due to the complex, multivariate nature of MeV SIMS datasets, the need for multivariate analysis techniques for the detection of underlying patterns and extraction of latent information is justified in MeV SIMS imaging examples from forensics of ink intersections. On this basis, the work presented in this thesis explored MeV SIMS capabilities in this field first through a feasibility study involving inks from various types of writing tools, with image analysis enhanced by the use of PCA. Here, a novel approach was proposed to investigate the unsolved cases by means of another IBA method called PIXE, which provides insight in elemental composition at greater depths. This strategy revealed valuable information on ink deposition events at the point of intersection, and helped in solving some cases. This initial research was followed by a focused study on cases deemed the most problematic for forensic examiners, simulated in a forensic laboratory. In this final study, a more sophisticated, non-linear multivariate algorithm called t-SNE has shown substantial success in determining the deposition order of optically identical ballpoint pen inks, which seemed to yield almost identical mass spectra as well. Generally, MeV SIMS showed better results in determining the deposition order when dealing with oil-based rather than liquid-based writing tool inks. However, the ink traces in all systems of intersecting lines analyzed so far were easily differentiated using MeV SIMS, and such valuable information can be exploited in other cases of official document forgery, such as alteration or addition of letters and numbers, where no overlapping traces are present or relevant.

Contributions of MeV ToF SIMS coupled with multivariate analysis demonstrated in this thesis could hopefully pave the way to the recognition of MeV SIMS as an additional forensic tool in the examination of ink intersections. Certainly, it is necessary to perform further extensive and systematic investigation in terms of repeatability and reproducibility on well-defined sets of samples.

The two topics covered in this thesis may have the potential to be merged together in some aspects. LE MeV SIMS could in theory be extended to various applications, among them the forensics of questioned documents, as well. The field involves countless types of writing tools composed of different proportions of various dyes, pigments and binders, leading to virtually infinite unique compositions of a particular ink found in a questioned sample. Some inks contain inorganic components, which could be analyzed with LE MeV SIMS via spot analysis, imaging or even depth profiling with an appropriate sputter source. In the presented work, several cases of ink intersections remained problematic to MeV SIMS, but could be further analyzed with a primary ion beam of lower energy if inorganic species are present that contribute to ink differentiation. This could be extended to depth profiling, which could reveal new information on processes that occur at the point of the interaction of inks below the surface in problematic cases.

Appendix A

LE MeV SIMS Spectra of Selected Inorganic Targets

Additional measurements were performed with LE MeV SIMS on various inorganic targets in order to expand the internal database of detectable inorganic ions. Samples mounted on a holder for Jeol JAMP 7830F Auger spectrometer were borrowed from the Laboratory for Surface and Thin Film Analysis at Jožef Stefan Institute (JSI), Ljubljana, where they are used as reference materials. The composition of some of the targets was pre-estimated with X-ray photoelectron spectroscopy (XPS) at JSI after sputter-cleaning with Ar (Figure A.1).

LABEL	COMPOSITION
L	Au
M	Hf
J	GaAs
K	Ge
A	Al
D	B-N-O
H	Co
I	Cu
N	InP
0	Fe
W	Pd
Y	Rh
Z	Ag
2	AgS
9	Zn

Figure A.1: Selected inorganic samples on a Jeol JAMP 7830F Auger spectrometer holder. The targets highlighted in the table and circled in the image were analyzed with LE MeV SIMS.

Spectra were collected with a 555 keV Cu^{2+} primary ion beam in a positive ion mode. Beam pulsing was used as a START signal for ToF measurement, and was performed with deflector voltage set to ± 300 V, using high voltage switch with 10 ns rise time and 100 µs between the ion pulses. Target voltage was set to +5 kV in order to push the secondary ions into the time-of-flight tube, while the MCP detector voltage was -2 kV. Measurements were carried out under a vacuum of $10^{-6} - 10^{-7}$ mbar. An area of about 250 x 250 μm^2 was analyzed for each sample. The spectra are shown in Figure A.2.

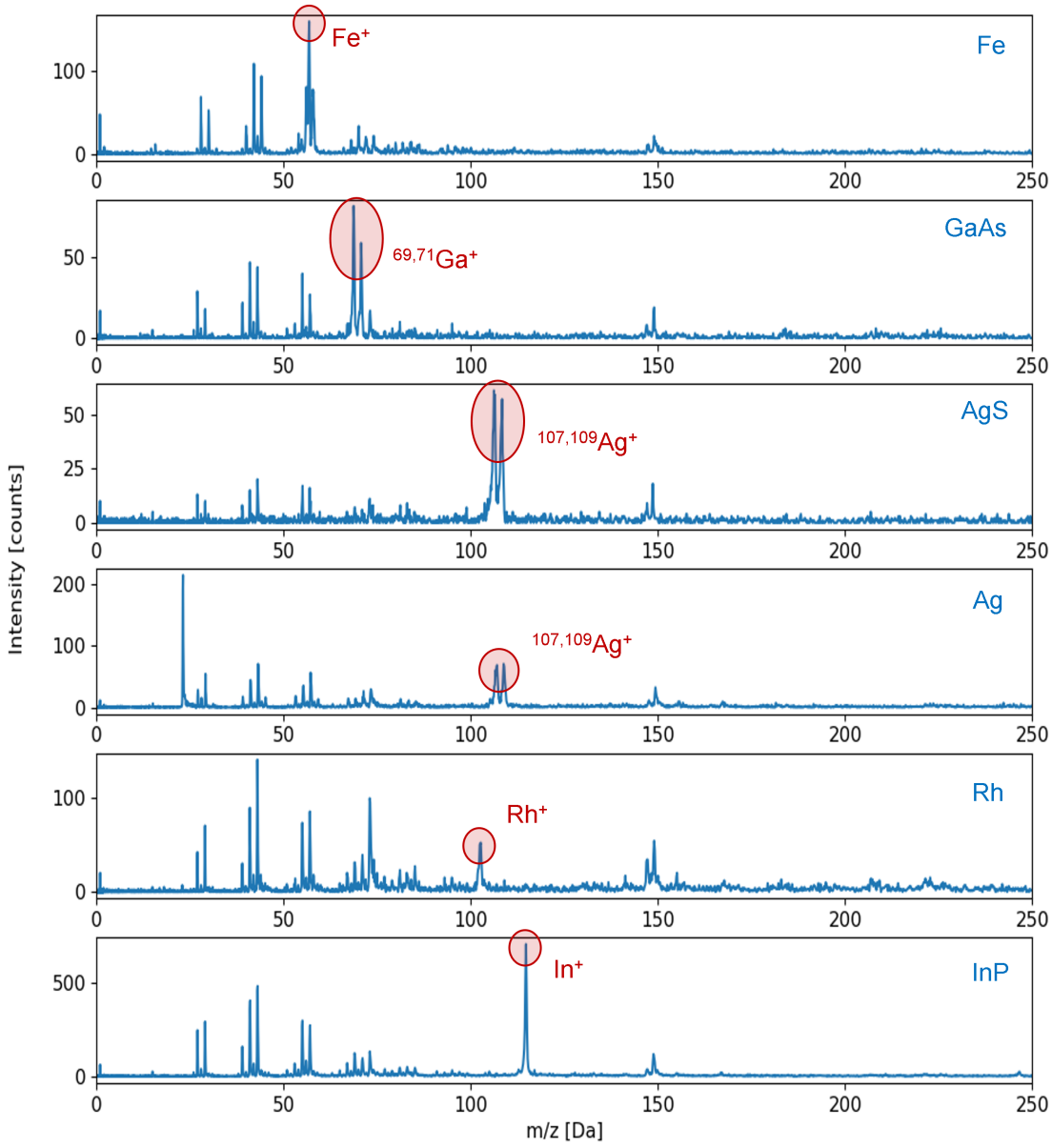

Figure A.2: LE MeV SIMS positive ion spectra of selected inorganic samples, analyzed using a 555 keV Cu^+ primary ion beam.

Other measured targets included Hf, Au, Ge, and Zn and yielded no indication that metallic ions are detectable under set conditions.

References

[1] J. H. Gross, *Mass spectrometry: A textbook*. Springer, Berlin Heidelberg, 2004.

[2] F. Michiels, W. Vanhoolst, W. Jacob, P. V. Espen, and F. Adams, "Applications of image processing for surface characterization and depth profiling with SIMS," *Micron and Microscopica Acta*, vol. 18, no. 3, pp. 249–250, Jan. 1987.

[3] D. S. McPhail, "Applications of Secondary Ion Mass Spectrometry (SIMS) in Materials Science," *Journal of Materials Science*, vol. 41, no. 3, pp. 873–903, Feb. 2006.

[4] L. A. McDonnell and R. M. Heeren, "Imaging mass spectrometry," *Mass Spectrometry Reviews*, vol. 26, no. 4, pp. 606–643, Apr. 2007.

[5] A. M. Belu, D. J. Graham, and D. G. Castner, "Time-of-flight secondary ion mass spectrometry: Techniques and applications for the characterization of biomaterial surfaces," *Biomaterials*, vol. 24, no. 21, pp. 3635–3653, Sep. 2003.

[6] D. G. Castner and B. D. Ratner, "Biomedical surface science: Foundations to frontiers," *Surface Science*, vol. 500, no. 1-3, pp. 28–60, Mar. 2002.

[7] S. Chandra, D. R. Smith, and G. H. Morrison, "Peer Reviewed: A Subcellular Imaging by Dynamic SIMS Ion Microscopy," *Analytical Chemistry*, vol. 72, no. 3, 104 A–114 A, Feb. 2000.

[8] R. Strick, P. L. Strissel, K. Gavrilov, and R. Levi-Setti, "Cation–chromatin binding as shown by ion microscopy is essential for the structural integrity of chromosomes," *Journal of Cell Biology*, vol. 155, no. 6, pp. 899–910, Dec. 2001.

[9] P. J. Todd, T. G. Schaaff, P. Chaurand, and R. M. Caprioli, "Organic ion imaging of biological tissue with secondary ion mass spectrometry and matrix-assisted laser desorption/ionization," *Journal of Mass Spectrometry*, vol. 36, no. 4, pp. 355–369, 2001.

[10] M. L. Pacholski, D. M. Cannon, A. G. Ewing, and N. Winograd, "Static time-of-flight secondary ion mass spectrometry imaging of freeze-fractured, frozen-hydrated biological membranes," *Rapid Communications in Mass Spectrometry*, vol. 12, no. 18, pp. 1232–1235, Sep. 1998.

[11] J. C. Vickerman and I. S. Gilmore, Eds., *Surface Analysis– The Principal Techniques*. John Wiley & Sons, Ltd, Apr. 2009.

[12] Y. Nakata, Y. Honda, S. Ninomiya, T. Seki, T. Aoki, and J. Matsuo, "Matrix-free high-resolution imaging mass spectrometry with high-energy ion projectiles," *Journal of Mass Spectrometry*, vol. 44, no. 1, pp. 128–136, Jan. 2009.

[13] T. Tadić, I. B. Radović, Z. Siketić, *et al.*, "Development of a TOF SIMS setup at the Zagreb heavy ion microbeam facility," *Nuclear Instruments and Methods in Physics Research Section B: Beam Interactions with Materials and Atoms*, vol. 332, pp. 234–237, Aug. 2014.

[14] B. N. Jones, V. Palitsin, and R. Webb, "Surface analysis with high energy time-of-flight secondary ion mass spectrometry measured in parallel with PIXE and RBS," *Nuclear Instruments and Methods in Physics Research Section B: Beam Interactions with Materials and Atoms*, vol. 268, no. 11-12, pp. 1714–1717, Jun. 2010.

[15] L. Jeromel, Z. Siketić, N. O. Potočnik, *et al.*, "Development of mass spectrometry by high energy focused heavy ion beam: MeV SIMS with 8 MeV Cl^{7+} beam," *Nuclear Instruments and Methods in Physics Research Section B: Beam Interactions with Materials and Atoms*, vol. 332, pp. 22–27, Aug. 2014.

[16] M. Schulte-Borchers, M. Döbeli, A. M. Müller, M. George, and H.-A. Synal, "Time-of-flight MeV-SIMS with beam induced secondary electron trigger," *Nuclear Instruments and Methods in Physics Research Section B: Beam Interactions with Materials and Atoms*, vol. 380, pp. 94–98, Aug. 2016.

[17] R. D. Macfarlane and D. F. Torgerson, "Californium-252 Plasma Desorption Mass Spectroscopy," *Science*, vol. 191, no. 4230, pp. 920–925, Mar. 1976.

[18] E. D. Silveira, C. McAfee, D. Cocke, D. Naugle, D. Sun, and E. Schweikert, "Particle desorption mass spectrometry of YBCO superconductors," *International Journal of Mass Spectrometry and Ion Processes*, vol. 91, no. 2, R5–R11, Jul. 1989.

[19] H. Feld, R. Zurmuehlen, A. Leute, and A. Benninghoven, "Carbon cluster emission from polymers under keV and MeV ion bombardment," *The Journal of Physical Chemistry*, vol. 94, no. 11, pp. 4595–4599, May 1990.

[20] M. Toulemonde, E. Paumier, and C. Dufour, "Thermal spike model in the electronic stopping power regime," *Radiation Effects and Defects in Solids*, vol. 126, no. 1-4, pp. 201–206, Mar. 1993.

[21] B. N. Jones, J. Matsuo, Y. Nakata, *et al.*, "Comparison of MeV monomer ion and keV cluster ToF-SIMS," *Surface and Interface Analysis*, vol. 43, no. 1-2, pp. 249–252, May 2010.

[22] B. Sundqvist, P. Roepstorff, J. Fohlman, *et al.*, "Molecular Weight Determinations of Proteins by Californium Plasma Desorption Mass Spectrometry," *Science*, vol. 226, no. 4675, pp. 696–698, Nov. 1984.

[23] D. M. Bunk and R. D. Macfarlane, "Fragmentation Analysis of Bradykinin by 252Cf-Plasma Desorption Mass Spectrometry," *Journal of the American Society for Mass Spectrometry*, vol. 2, no. 5, pp. 379–386, Sep. 1991.

[24] D. M. Bunk and R. D. Macfarlane, "Fragmentation of proteins in the 13- to 29-kDa mass range observed by 252Cf-plasma desorption mass spectrometry.," *Proceedings of the National Academy of Sciences*, vol. 89, no. 13, pp. 6215–6219, Jul. 1992.

[25] P. Hakansson, A. Johansson, I. Kamensky, B. Sundqvist, J. Fohlman, and P. Peterson, "Fast Heavy-Ion Induced Desorption of Biomolecules," *IEEE Transactions on Nuclear Science*, vol. 28, no. 2, pp. 1776–1778, 1981.

[26] Y. Nakata, H. Yamada, Y. Honda, *et al.*, "Imaging mass spectrometry with nuclear microprobes for biological applications," *Nuclear Instruments and Methods in Physics Research Section B: Beam Interactions with Materials and Atoms*, vol. 267, no. 12-13, pp. 2144–2148, Jun. 2009.

[27] Z. Siketić, I. B. Radović, M. Jakšić, M. P. Hadžija, and M. Hadžija, "Submicron mass spectrometry imaging of single cells by combined use of mega electron volt time-of-flight secondary ion mass spectrometry and scanning transmission ion microscopy," *Applied Physics Letters*, vol. 107, no. 9, p. 093 702, Aug. 2015.

[28] T. Seki, Y. Wakamatsu, S. Nakagawa, T. Aoki, A. Ishihara, and J. Matsuo, "Biomaterial imaging with MeV-energy heavy ion beams," *Nuclear Instruments and Methods in Physics Research Section B: Beam Interactions with Materials and Atoms*, vol. 332, pp. 326–329, Aug. 2014.

[29] L. Breuer, F. Meinerzhagen, M. Bender, D. Severin, and A. Wucher, "Time-of-flight secondary neutral & ion mass spectrometry using swift heavy ions," *Nuclear Instruments and Methods in Physics Research Section B: Beam Interactions with Materials and Atoms*, vol. 365, pp. 482–489, Dec. 2015.

[30] M. Bailey, B. Jones, S. Hinder, J. Watts, S. Bleay, and R. Webb, "Depth profiling of fingerprint and ink signals by SIMS and MeV SIMS," *Nuclear Instruments and Methods in Physics Research Section B: Beam Interactions with Materials and Atoms*, vol. 268, no. 11-12, pp. 1929–1932, Jun. 2010.

[31] L. Beck, "Recent trends in IBA for cultural heritage studies," *Nuclear Instruments and Methods in Physics Research Section B: Beam Interactions with Materials and Atoms*, vol. 344, pp. 439–444, Feb. 2015.

[32] K. Chughtai and R. M. A. Heeren, "Mass Spectrometric Imaging for Biomedical Tissue Analysis," *Chemical Reviews*, vol. 110, no. 5, pp. 3237–3277, Apr. 2010.

[33] Z. Siketić, I. Bogdanović Radović, M. Jakšić, M. Popović Hadžija, and M. Hadžija, "Submicron mass spectrometry imaging of single cells by combined use of Mega Electron Volt time-of-flight secondary ion mass spectrometry and scanning transmission ion microscopy," *Applied Physics Letters*, vol. 107, no. 9, p. 093 702, 2015. DOI: 10.1063/1.4930062.

[34] J. Vickerman, D. Briggs, and S. Limited, *TOF-SIMS: Surface Analysis by Mass Spectrometry*. IM publications, 2001, ISBN: 9781901019032.

[35] J. Biersack and L. Haggmark, "A Monte Carlo computer program for the transport of energetic ions in amorphous targets," *Nuclear Instruments and Methods*, vol. 174, no. 1-2, pp. 257–269, Aug. 1980.

[36] M. Robinson and I. Torrens, "Computer simulation of atomic-displacement cascades in solids in the binary-collision approximation," *Physical Review B*, vol. 9, no. 12, pp. 5008–5024, Jun. 1974.

[37] M. T. Robinson, "Computer simulation studies of high-energy collision cascades," *Nuclear Instruments and Methods in Physics Research Section B: Beam Interactions with Materials and Atoms*, vol. 67, no. 1-4, pp. 396–400, Apr. 1992.

[38] A. Bohr, *Atomic interaction in penetration phenomena*. Munksgaard Copenhagen, Denmark, 1948, vol. 18.

[39] J. Lindhard, M. Scharff, and H. E. Schiøtt, *Range concepts and heavy ion ranges*. Munksgaard Copenhagen, 1963, vol. 33.

[40] J. Schou, "Slowing-down processes, energy deposition, sputtering and desorption in ion and electron interactions with solids," 2007.

[41] J. Lindhard and M. Scharff, "Energy dissipation by ions in the kev region," *Physical Review*, vol. 124, no. 1, p. 128, 1961.

[42] P. Sigmund, *Particle Penetration and Radiation Effects*. Springer Berlin Heidelberg, 2006.

[43] ——, *Fundamental Processes in Sputtering of Atoms and Molecules (SPUT92): Symposium on the Occasion of the 250th Anniversary of the Royal Danish Academy of Sciences and Letters, Copenhagen, 30 August - 4 September, 1992: Invited Reviews*. Royal Danish Academy of Sciences and Letters, 1993, vol. 43.

[44] ——, "Theory of sputtering. i. sputtering yield of amorphous and polycrystalline targets," *Physical Review*, vol. 184, no. 2, pp. 383–416, 1969. DOI: 10.1103/physrev.184.383.

[45] ——, "Theory of sputtering. i. sputtering yield of amorphous and polycrystalline targets," *Physical Review*, vol. 187, no. 2, pp. 768–768, 1969. DOI: 10.1103/physrev.187.768.

[46] ——, "Sputtering by ion bombardment: Theoretical concepts," in *Sputtering by Particle Bombardment I*, R. Behrisch, Ed. Springer, 1981, vol. 47, pp. 9–71.

[47] R. Hoogerbrugge and P. G. Kistemaker, "Analytical expressions for the internal and kinetic energy distributions of sputtered clusters and molecules," *Nuclear Instruments and Methods in Physics Research Section B: Beam Interactions with Materials and Atoms*, vol. 21, no. 1-4, pp. 37–45, 1987. DOI: 10.1016/0168-583x(87)90136-4.

[48] R. Haring, H. Roosendaal, and P. Zalm, "On the energy and angular distribution of sputtered polyatomic molecules," *Nuclear Instruments and Methods in Physics Research Section B: Beam Interactions with Materials and Atoms*, vol. 28, no. 2, pp. 205–213, 1987. DOI: 10.1016/0168-583x(87)90106-6.

[49] B. J. Garrison, "Molecular desorption induced by heavy particle bombardment of solids," *International Journal of Mass Spectrometry and Ion Physics*, vol. 53, pp. 243–254, 1983. DOI: 10.1016/0020-7381(83)85115-8.

[50] R. Hoogerbrugge, W. J. van der Zande, and P. G. Kistemaker, "Collision cascade contributions in the sputtering of polyatomic ions from a glycerol matrix," *International Journal of Mass Spectrometry and Ion Processes*, vol. 76, no. 3, pp. 239–246, 1987. DOI: 10.1016/0168-1176(87)83028-8.

[51] T.-Y. Yen, "Thesis," Ph.D. dissertation, Dept. of Agricultural Chemistry, Oregon State University, 1992.

[52] A. Hedin, P. Hakansson, B. Sundqvist, and R. E. Johnson, "Ion-track model for fast-ion-induced desorption of molecules," *Physical Review B*, vol. 31, no. 4, pp. 1780–1787, 1985. DOI: 10.1103/physrevb.31.1780.

[53] R. Katz, "Track structure theory in radiobiology and in radiation detection," *Nuclear Track Detection*, vol. 2, no. 1, pp. 1–28, 1978. DOI: 10.1016/0145-224x(78)90002-9.

[54] A. Hedin, P. Hakansson, M. Salehpour, and B. U. Sundqvist, "Fast-ion-induced erosion of leucine as a function of the electronic stopping power," *Physical Review B*, vol. 35, no. 14, pp. 7377–7381, 1987. DOI: 10.1103/physrevb.35.7377.

[55] W. Ens, B. U. Sundqvist, P. Hakånsson, D. Fenyö, A. Hedin, and G. Jonsson, "Radial velocity measurements of secondary molecular ions in kev and mev bombardment," *Le Journal de Physique Colloques*, vol. 50, no. C2, 1989. DOI: 10.1051/jphyscol:1989202.

[56] S. L. Lee and R. A. Lucchese, "Models for high energy ion induced desorption of molecules from surfaces," *Le Journal de Physique Colloques*, vol. 50, no. C2, 1989. DOI: 10.1051/jphyscol:1989237.

[57] J. Sunner, A. Morales, and P. Kebarle, "Mechanism of formation of fab spectra," *International Journal of Mass Spectrometry and Ion Processes*, vol. 86, pp. 169–186, 1988. DOI: 10.1016/0168-1176(88)80062-4.

[58] H. M. Urbassek and K. T. Waldeer, "Spikes in condensed rare gases induced by kev-atom bombardment," *Physical Review Letters*, vol. 67, no. 1, pp. 105–108, 1991. DOI: 10.1103/physrevlett.67.105.

[59] J. Shiea and J. Sunner, "Molecular dynamics simulation of bulk desorption," *NATO ASI Series*, pp. 147–156, 1991. DOI: 10.1007/978-1-4684-7926-3_20.

[60] R. Kelly, "Thermal sputtering as a gas-dynamic process," *Nuclear Instruments and Methods in Physics Research Section B: Beam Interactions with Materials and Atoms*, vol. 46, no. 1-4, pp. 441–447, 1990. DOI: 10.1016/0168-583x(90)90744-f.

[61] R. E. Johnson, B. U. Sundqvist, A. Hedin, and D. Fenyö, "Sputtering by fast ions based on a sum of impulses," *Physical Review B*, vol. 40, no. 1, pp. 49–53, 1989. DOI: 10.1103/physrevb.40.49.

[62] "RBI facility layout." (2022), [Online]. Available: https://www.irb.hr/eng/Divisions/Division-of-Experimental-Physics/Laboratory-for-ion-beam-interactions/Articles/Accelerators (visited on 03/03/2022).

[63] R. J. Cotter and D. H. Russell, "Time-of-flight mass spectrometry: Instrumentation and applications in biological research," *Journal of the American Society for Mass Spectrometry*, vol. 10, no. 9, pp. 1104–1105, 1998.

[64] M. R. Keenan and P. G. Kotula, "Accounting for Poisson noise in the multivariate analysis of TOF-SIMS spectrum images," *Surface and Interface Analysis*, vol. 36, no. 3, pp. 203–212, 2004.

[65] J. C. Vickerman and D. Briggs, *TOF-SIMS: Materials Analysis by Mass Spectrometry*. IM publications, 2013.

[66] S. M. Holand. "PRINCIPAL COMPONENT ANALYSIS (PCA)." (2022), [Online]. Available: https://strata.uga.edu/software/pdf/pcaTutorial.pdf (visited on 03/03/2022).

[67] L. Van der Maaten and G. Hinton, "Visualizing data using t-SNE," *Journal of machine learning research*, vol. 9, no. 11, 2008.

[68] L. Deng, "The MNIST database of handwritten digit images for machine learning research," *IEEE Signal Processing Magazine*, vol. 29, no. 6, pp. 141–142, 2012.

[69] X. V. Eynde and P. Bertrand, "TOF-SIMS quantification of polystyrene spectra based on principal component analysis (PCA)," *Surface and Interface Analysis: An International Journal devoted to the development and application of techniques for the analysis of surfaces, interfaces and thin films*, vol. 25, no. 11, pp. 878–888, 1997.

[70] M. Wagner and D. G. Castner, "Characterization of adsorbed protein films by time-of-flight secondary ion mass spectrometry with principal component analysis," *Langmuir*, vol. 17, no. 15, pp. 4649–4660, 2001.

[71] M. Wagner, B. Tyler, and D. G. Castner, "Interpretation of static time-of-flight secondary ion mass spectra of adsorbed protein films by multivariate pattern recognition," *Analytical Chemistry*, vol. 74, no. 8, pp. 1824–1835, 2002.

[72] B. Tyler, "Interpretation of TOF-SIMS images: Multivariate and univariate approaches to image de-noising, image segmentation and compound identification," *Applied surface science*, vol. 203, pp. 825–831, 2003.

[73] N. B. Gallagher, J. M. Shaver, E. B. Martin, J. Morris, B. M. Wise, and W. Windig, "Curve resolution for multivariate images with applications to TOF-SIMS and Raman," *Chemometrics and intelligent laboratory systems*, vol. 73, no. 1, pp. 105–117, 2004.

[74] A. De Juan and R. Tauler, "Multivariate curve resolution (MCR) from 2000: Progress in concepts and applications," *Critical reviews in analytical chemistry*, vol. 36, no. 3-4, pp. 163–176, 2006.

[75] M. Wagner, D. Graham, and D. Castner, "Simplifying the interpretation of TOF-SIMS spectra and images using careful application of multivariate analysis," *Applied Surface Science*, vol. 252, no. 19, pp. 6575–6581, 2006.

[76] D. J. Graham, M. S. Wagner, and D. G. Castner, "Information from complexity: Challenges of TOF-SIMS data interpretation," *Applied surface science*, vol. 252, no. 19, pp. 6860–6868, 2006.

[77] J. L. Lee, I. S. Gilmore, M. P. Seah, and I. W. Fletcher, "Topography and field effects in secondary ion mass spectrometry Part I: Conducting samples," *Journal of The American Society for Mass Spectrometry*, vol. 22, no. 10, 2011.

[78] J. Lee, I. Gilmore, M. Seah, A. Levick, and A. Shard, "Topography and field effects in secondary ion mass spectrometry Part II: Insulating samples," *Surface and interface analysis*, vol. 44, no. 2, pp. 238–245, 2012.

[79] J. Lee, I. Gilmore, and M. Seah, "Quantification and methodology issues in multivariate analysis of TOF-SIMS data for mixed organic systems," *Surface and Interface Analysis: An International Journal devoted to the development and application of techniques for the analysis of surfaces, interfaces and thin films*, vol. 40, no. 1, pp. 1–14, 2008.

[80] J. Lee, I. Gilmore, I. Fletcher, and M. Seah, "Multivariate image analysis strategies for TOF-SIMS images with topography," *Surface and Interface Analysis: An International Journal devoted to the development and application of techniques for the analysis of surfaces, interfaces and thin films*, vol. 41, no. 8, pp. 653–665, 2009.

[81] J. Lee, I. Gilmore, and M. Seah, "Proposed terminology for multivariate analysis in surface chemical analysis–vocabulary–part 1: General terms and terms for the spectroscopies," *Chem. Anal.*, pp. 1–10, 2008.

[82] J. Lee, "Time-of-flight secondary ion mass spectrometry-fundamental issues for quantitative measurements and multivariate data analysis," 2011.

[83] I. S. Gilmore and M. S. Wagner, "Multivariate Analysis in Surface Analysis-Part I," *Surface and Interface Analysis: An International Journal devoted to the development and application of techniques for the analysis of surfaces, interfaces and thin films*, vol. 41, no. 2, 2009.

[84] ——, "Multivariate Analysis in Surface Analysis-Part II," *Surface and Interface Analysis: An International Journal devoted to the development and application of techniques for the analysis of surfaces, interfaces and thin films*, vol. 41, no. 8, 2009.

[85] I. Gilmore, M. Wagner, and P. Trevorrow, "A bright future for Multivariate Analysis Applications in Surface Science," *Surface and Interface Analysis*, vol. 41, no. 8, pp. 634–635, 2009.

[86] P. J. Cumpson, I. W. Fletcher, N. Sano, and A. J. Barlow, "Rapid multivariate analysis of 3D TOF-SIMS data: Graphical processor units (GPUs) and low-discrepancy subsampling for large-scale principal component analysis," *Surface and Interface Analysis*, vol. 48, no. 12, pp. 1328–1336, 2016.

[87] P. J. Cumpson, N. Sano, I. W. Fletcher, J. F. Portoles, M. Bravo-Sanchez, and A. J. Barlow, "Multivariate analysis of extremely large TOF-SIMS imaging datasets by a rapid PCA method," *Surface and Interface Analysis*, vol. 47, no. 10, pp. 986–993, 2015.

[88] N. Tuccitto, "Automated data mining of secondary ion mass spectrometry spectra," *Journal of Chemometrics*, vol. 32, no. 3, e2968, 2018.

[89] S. A. Thomas, A. M. Race, R. T. Steven, I. S. Gilmore, and J. Bunch, "Dimensionality reduction of mass spectrometry imaging data using autoencoders," in *2016 IEEE symposium series on computational intelligence (SSCI)*, IEEE, 2016, pp. 1–7.

Bibliography

Publications Related to the Thesis

Journal Articles

M. Barac, M. Brajković, Z. Siketić, *et al.*, "Depth profiling of Cr-ITO dual-layer sample with secondary ion mass spectrometry using MeV ions in the low energy region," *Scientific Reports*, vol. 12, no. 1, 2022.

M. Barac, A. Filko, Z. Siketić, M. Brajković, A. Ledić, and I. B. Radović, "Comparison of optical techniques and MeV SIMS in determining deposition order between optically distinguishable and indistinguishable inks from different writing tools," *Forensic Science International*, vol. 331, p. 111 136, 2022.

M. Barac, M. Brajkovic, I. Bogdanović Radović, J. Kovac, and Z. Siketic, "MeV TOF SIMS Analysis of Hybrid Organic/inorganic Compounds in the Low Energy Region," *Journal of the American Society for Mass Spectrometry*, vol. 32, no. 3, pp. 825–831, 2021.

K. L. Moore, M. Barac, M. Brajković, M. J. Bailey, Z. Siketić, and I. Bogdanović Radović, "Determination of deposition order of toners, inkjet inks, and blue ballpoint pen combining MeV-secondary ion mass spectrometry and particle induced X-ray emission," *Analytical chemistry*, vol. 91, no. 20, pp. 12 997–13 005, 2019.

Other Publications

Journal Articles

T. Fischer, M. Marchetti-Deschmann, A. Cristina Assis, *et al.*, "Profiling and imaging of forensic evidence – a pan-European Forensic Round Robin Study Part 1: Document forgery," *Science & Justice*, vol. 62, no. 4, pp. 433–447, 2022.

I. B. Mihalić, S. Fazinić, M. Barac, *et al.*, "Multivariate analysis of PIXE + XRF and PIXE spectral images," *Journal of Analytical Atomic Spectrometry*, vol. 36, no. 3, pp. 654–667, 2021.

M. Brajković, I. Bogdanović Radović, M. Barac, D. D. Cosic, and Z. Siketić, "Imaging of Organic samples with Megaelectron Volt Time-of-Flight Secondary Ion Mass Spectrometry Capillary Microprobe," *Journal of the American Society for Mass Spectrometry*, vol. 32, no. 10, pp. 2567–2572, 2021.

M. P. Hadžija, Z. Siketić, M. Hadžija, M. Barac, and I. B. Radović, "Study of the diacylglycerol composition in the liver and serum of mice with prediabetes and diabetes using MeV TOF-SIMS," *Diabetes Research and Clinical Practice*, vol. 159, p. 107 986, 2020.

M. Brajković, M. Barac, I. Bogdanović Radović, and Z. Siketić, "Dependence of Megaelectron Volt time-of-flight secondary ion mass spectrometry secondary molecular ion yield from phthalocyanine blue on primary ion stopping power," *Journal of the American Society for Mass Spectrometry*, vol. 31, no. 7, pp. 1518–1524, 2020.

M. Brajković, M. Barac, D. Cosic, I. B. Radović, and Z. Siketić, "Development of MeV TOF-SIMS capillary microprobe at the Ruđer Bošković Institute in zagreb," *Nuclear Instruments and Methods in Physics Research Section B: Beam Interactions with Materials and Atoms*, vol. 461, pp. 237–242, 2019.

Biography

The author of this thesis obtained his Master's Degree in Atomic and Molecular Physics at the Department of Physics, University of Rijeka, Croatia, in 2017, with a thesis titled *Influence of secondary effects in XRF analysis* under the supervision of Prof. Dr. Sc. Ivo Orlić. In 2018, he started working in the Laboratory for Ion Beam Interactions at Ruđer Bošković Institute, Zagreb, Croatia, as a research assistant under the mentorship of Dr. Sc. Zdravko Siketić. Parallelly, he started his doctoral studies at the Nanosciences and Nanotechnologies programme at the Jožef Stefan International Postgraduate School in Ljubljana, Slovenia, co-mentored by Prof. Dr. Janez Kovač. The scope of work included operating an in-house MeV ToF SIMS experimental setup, studying different primary ion beam energy modes and their effects on the secondary ion yield from various types of materials, and investigation and application of multivariate analysis techniques for data analysis of MeV SIMS datasets. The author gained experience in MeV SIMS application in different fields ranging from biomedical research, archaeology, plant biology, to cultural heritage and forensics. Along the way, the author made significant progress in the analysis and interpretation of MeV SIMS measurements in the forensic field of questioned documents, resulting, inter alia, in receiving The Annual Award of Ruđer Bošković Institute for the best scientific papers in 2021. Apart from the MeV SIMS technique, the author obtained experience in other Ion Beam Analysis (IBA) techniques, such as STIM, PIXE, and RBS. During his research, the author collaborated on several projects, presented his work at many internationally recognized conferences, and trained on international schools and workshops.